Numerical study of higher order topological insulators by machine learning and Berry phases

Hiromu Araki

February 2020

Numerical study of higher order topological insulators by machine learning and Berry phases

Hiromu Araki
Doctoral Program in Physics

Submitted to the Graduate School of Pure and Applied Sciences in Partial Fulfillment of the Requirements for the Degree of Doctor of Philosophy in Science

at the
University of Tsukuba

Contents

1 Introduction **3**
- 1.1 Background . . . 3
- 1.2 Purpose . . . 4
- 1.3 Outline . . . 4

2 Topological insulator phases and topological invariants **6**
- 2.1 The quantum spin Hall phase . . . 6
  - 2.1.1 The time-reversal symmetry, Kramers' theorem and time-reversal invariant momentum . . . 7
  - 2.1.2 The $\mathbb{Z}_2$ index for the quantum spin Hall phase . . . 8
  - 2.1.3 The tight-binding model for the quantum spin Hall phase – the Kane-Mele model . . . 8
- 2.2 Topological insulator phases . . . 12
  - 2.2.1 The $\mathbb{Z}_2$ indices for strong and weak topological insulator phases . . . 12
  - 2.2.2 The tight-binding model for the topological insulator phase – the Fu-Kane-Mele model . . . 13
- 2.3 The entanglement Chern number for topological phases . . . 15
  - 2.3.1 Definition of the entanglement Chern numbers . . . 16
  - 2.3.2 The entanglement Chern number for the quantum spin Hall phase . . . 17
  - 2.3.3 The entanglement Chern number for the topological insulator phase . . . 18

3 Higher-order topological insulators **21**
- 3.1 Higher-order topological insulator on hyper-cubic lattices . . . 21
  - 3.1.1 Tight-binding models for the higher-order topological insulators on hyper-cubic lattices . . . 21
  - 3.1.2 The topological invariants for the BBH models . . . 23
- 3.2 Higher-order topological insulators on hyper-tetrahedral lattices . . . 26
  - 3.2.1 Tight-binding model for Higher-order topological insulators on hyper-tetrahedral lattices . . . 27
  - 3.2.2 The topological invariants for the hyper-tetrahedral HOTI models . . . 29
- 3.3 Experimental realizations . . . 30

4 Berry phase and its quantization **32**
- 4.1 Berry phase with local bond twist . . . 32
  - 4.1.1 The Berry phase for tight-binding models . . . 32
  - 4.1.2 The Berry phase for spin models . . . 33
- 4.2 Symmetries and quantization of the Berry phase . . . 34

5 Quantized Berry phases for higher-order topological insulators 35
5.1 Quantized Berry phases . . . 35
5.1.1 Quantized Berry phases for the BBH model . . . 35
5.1.2 Bulk-corner correspondence . . . 37
5.2 Quantized Berry phases for Higher-order topological insulator models . . . 38
5.2.1 The BBH model with next-nearest neighbour hopping . . . 38
5.2.2 The BBH model with intersite interactions . . . 40
5.2.3 Spin-model-analogue of the BBH model . . . 41
5.2.4 The BBH model in three-dimensions . . . 42
5.3 Conclusion . . . 44
5.4 Appendix . . . 45

6 Machine learning study for the disordered higher-order topological insulators 48
6.1 Disordered kagome higher-order topological insulators . . . 48
6.1.1 Phase diagrams for rhombus and triangular geometries in the clean limit 49
6.1.2 Symmetries and topological invariants . . . 50
6.1.3 Effect of disorders . . . 51
6.2 Identification of the topological phase by machine learning . . . 51
6.2.1 Configuration of the neural network . . . 51
6.2.2 Input and output data . . . 52
6.2.3 Supervised learning . . . 53
6.3 Disordered higher-order topological insulator phases . . . 54
6.3.1 Result for the rhombus geometry . . . 54
6.3.2 Result for the triangular geometry . . . 56
6.3.3 Inverse participation ratio . . . 56
6.4 Conclusion . . . 57

7 Conclusions and perspectives 59

8 Acknowledgment 60

Publications 61

Bibliography 63

Chapter 1

Introduction

1.1 Background

Since the discovery of the quantum Hall effect by K. von Klitzing *et al.* in 1980 [1], the topological materials have attracted great deals of attentions in condensed matter physics. One of the remarkable features of the topological materials is that the topological property is determined by the bulk wavefunctions [2]. Another remarkable feature is the bulk-edge correspondence [3–6], which claims that gapless edge states appear when the insulator has non-trivial bulk topological property.

In 2005, the quantum spin Hall effect for the insulator under the time-reversal symmetry was proposed by C. Kane and E. Mele [7,8]. It is a topological material that has a finite spin current on edges protected by non-trivial topological invariant. The concept of the quantum spin Hall effect was brought in three dimensions, which is called the topological insulator [9]. After the epoch-making study, the topological insulators had been extensively studied. One of the prominent discovery might be the periodic table of the topological insulators and superconductors [10–12], which is also called the Altland-Zirnbauer classification [13]. It gives the comprehensive classification of non-interacting topological insulators and superconductors under time-reversal symmetry, chiral symmetry and particle-hole symmetry in arbitrary spacial dimensions. The topological classifications are extended to include the crystalline symmetries, such as inversion, mirror and glide symmetries [14, 15, 15–19].

While the topological insulator phases appear in non-interacting systems, the electron-electron interactions enrich the physics of topological insulators. One of the effect of interactions is known to be the reduction of the classification [20–23]. For example, the $\mathbb{Z}$ classification of one-dimensional BDI symmetry class is broken to $\mathbb{Z}_8$ with interactions. Further, the interactions induce the new topological physics – such as the topological Mott insulator [24,25] and the fractional topological insulator [26–29]. Also, it is revealed that the short-range entangled states of many-body systems protected by symmetries can host the nontrivial topological state, which are now understood as the symmetry-protected topological (SPT) phases [30–34].

The Berry phase is known to be an useful tool to characterize the SPT phases [35–44]. The Berry phase get a quantized value because of the symmetry of the system, such as the chiral symmetry, the time-reversal symmetry, the inversion symmetry and the SU(N) symmetry of the spins.

In the couple of years, the higher-order topological insulators (HOTI) are intensely studied [45–56]. The HOTIs in d-dimensions has topologically protected boundary states in $d-n$ dimensional boundaries ($n \geq 2$), *e.g.*, hinge states in three dimensions and corner states in two and three dimensions. Since the proposal of the HOTIs, the higher-order topological materials are experimentally realized one after another, such as bismuth crystals [57],

mechanical systems [58], electrical circuits [59, 60], photonic crystals [61, 62] and acoustic systems [63].

On the other hand, the machine learning, especially the artificial neural network, is widely used in the various fields in physics, including astrophysics [64], high-energy physics [65, 66], Monte Carlo simulations [67] and quantum many-body systems [68–72]. As for the research of topological states, the first-order topological insulators and the topological superconductors have been successfully classified in the presence of disorders, and the resulting phase diagrams reproduce those obtained by the other methods [73–75].

1.2 Purpose

The primary purpose of this thesis is the theoretical investigation of the properties of the higher-order topological insulator phases by numerical analysis of the boundary states and the topological invariants. We investigate the higher-order topological insulator phases by both the Berry phases and the machine learning. By the Berry phase, we investigate the higher-order topological insulator phases for the system with and without interactions and the spin models. By the machine learning, we investigate the phase transition of the higher-order topological insulator models with disorders.

1.3 Outline

In Chapter 2, we briefly introduce the topological phases and their topological invariants. Firstly, we introduce the quantum Hall effect and its topological invariants, the Chern number. Secondly, we introduce the quantum spin Hall effect and the $\mathbb{Z}_2$ index. Thirdly, we introduce the topological insulator phase and the $\mathbb{Z}_2$ indices. Lastly, we review the related studies about the entanglement Chern numbers, which characterizes these topological phases.

Chapter 3 reviews the higher-order topological insulators. Firstly, we show the theory of the higher-order topological insulators in both hyper-cubic lattices and hyper-tetrahedral lattices. Then, we briefly review the experimental realizations of the higher-order topological materials.

Chapter 4 describes the Berry phase and its quantization. Firstly we show the definition of the Berry phase by introducing a local bond twists. Then we show the symmetries and the quantization of the Berry phase.

Chapter 5 proposes the quantized Berry phase with the bond-twists as a topological invariant, which characterizes the higher-order topological insulator phases. The quantized Berry phase is topologically stable even with the electron-electron interactions unless the energy gap is closed. To demonstrate it for a concrete model, we have shown the quantization of the Berry phase in $\mathbb{Z}_4$ and the characterization of the higher-order topological insulator phases in several extended Benalcazar-Bernevig-Hughes (BBH) models that contain the intersite Coulomb interactions and the next-nearest neighbor hopping. In addition, we show the quantized Berry phase for the quantum spin analog of the BBH model. Further, we show that the BBH model in three-dimensions also has the Berry phase quantized in $\mathbb{Z}_4$. We also confirm the bulk-corner correspondence between the quantized Berry phase and the corner states in the higher-order topological insulator phases.

In Chapter 6, we investigate the higher-order topological insulators by using machine learning technique. We applied the image recognition method of machine learning, which detects the boundary states of topological materials. Focusing on the higher-order topological insulator model on a breathing kagome lattice, we studied the robustness of the higher-order topological insulator phases against disorders. We have successfully generated a phase diagram by machine learning which is consistent with the other analytical method. We have

also numerically found that the higher-order topological insulator phases are robust against disorder as far as the disorder strength does not exceed the energy gap.

Chapter 2

Topological insulator phases and topological invariants

In recent decades, the topological phenomena have highly attracted many researchers in condensed matter physics. One of the typical phenomena is the quantum Hall effect. The quantum Hall effect is a phenomena that the Hall conductance σ_H of the system in the strong magnetic field is quantized as $\sigma_{\mathrm{H}} = \frac{e^2}{h}\nu$. Here, e is the elementary electric charge and h is the Planck constant. The ν is the filling factor, which is the ratio of the electrons to the Landau level under the Fermi level. The quantum Hall effect is discovered by K. von Klitzing, G. Dorda and M. Pepper in 1980 [1]. They measured the Hall conductance of a two dimensional electron gas on a silicon metal-oxide-semiconductor field-effect transistor. The filling factor ν for the quantum Hall systems is given as the Chern number

$$\nu \equiv \frac{1}{2\pi i}\int_{\mathrm{BZ}} B_z(\boldsymbol{k})\mathrm{d}^2k \tag{2.1}$$

Here, $\psi(\boldsymbol{k})$ is the Bloch wave-function, $\boldsymbol{A}(\boldsymbol{k}) = \langle\psi(\boldsymbol{k})|\boldsymbol{\nabla}|\psi(\boldsymbol{k})\rangle$ is the Berry connection, and $\boldsymbol{B}(\boldsymbol{k}) = \boldsymbol{\nabla}\times\boldsymbol{A}(\boldsymbol{k})$ is the Berry curvature. The formula $\sigma_{\mathrm{H}} = \frac{e^2}{h}\nu$ is called as the TKNN formula, which is given by D. J. Thouless, M. Kohmoto, M. P. Nightingale and M. den Nijs [2]. Because the Chern number is a topological number for the Bloch wave function, it does not change under adiabatic transformation. The quantum Hall system has a bulk-edge correspondence that the Chern number corresponds to the number of chiral edge states localized on the edge of the system [5].

In the following sections, we introduce the novel topological phases, the quantum spin Hall phase and the topological insulator phases. We also review the related studies about the entanglement Chern numbers, which characterizes these topological phases.

2.1 The quantum spin Hall phase

In 2005, the quantum spin Hall effect is proposed by C. L.Kane and E. J. Mele [7]. They found that the two-dimensional system under time-reversal symmetry has a topological phase, in which the spin current on the edges is finite and the state is protected by the non-trivial $\mathbb{Z}_2$ index. A typical model for the quantum spin Hall effect is the Kane-Mele model, which is a tight-binding model on a honeycomb lattice [7]. The model Hamiltonian contains the spin-orbit coupling that is essential for the quantum spin Hall effect. The spin-orbit coupling can be considered as the effective magnetic field for up and down spins in the opposite directions. When the up and down spins are decoupled, the quantum spin Hall system consists of two copies of the quantum Hall systems about each of spins. In this section, we review the

quantum spin Hall effect and the $\mathbb{Z}_2$ index. Firstly, we introduce the $\mathbb{Z}_2$ index and the quantum spin Hall effect. Secondly, we show the Kane-Mele model as a typical model for the quantum spin Hall effect.

2.1.1 The time-reversal symmetry, Kramers' theorem and time-reversal invariant momentum

The time-reversal operator Θ is defined as changing the direction of the time as $\Theta : t \mapsto -t$. The time-reversal operator transforms the position operator $\boldsymbol{r}$ to $\boldsymbol{r}$, the momentum operator $\boldsymbol{p}$ to $-\boldsymbol{p}$, and the spin operator $\boldsymbol{s}$ to $-\boldsymbol{s}$. Here we represent the spin operator $\boldsymbol{s} = \boldsymbol{\sigma}/2$ using the Pauli matrices $\boldsymbol{\sigma}$. In this representation, the time-reversal operator is written as $\Theta = -i\sigma_y\mathcal{K}$, where $\mathcal{K}$ is the complex conjugation operator.

Next, we consider the system with the time-reversal symmetry, whose Hamiltonian $\mathcal{H}$ satisfies $\Theta\mathcal{H}\Theta^{-1} = \mathcal{H}$, i.e. $[\mathcal{H}, \Theta] = 0$. Hence, if one of the eigenstate of the system is $|u_j\rangle$, then $\Theta|u_j\rangle$ is also the eigenstate of the system. We note that the eigenstates $|u_j\rangle$ and $\Theta|u_j\rangle$ are orthogonal The degenerated pair $|u_j\rangle$ and $\Theta|u_j\rangle$ are called the Kramers pair and the degeneracy is called the Kramers degeneracy. The *Kramers theorem* states that if the Hamiltonian commutes with the time-reversal operator Θ with $\Theta^2 = -1$, the eigenstates of the Hamiltonian have the Kramers pairs and the eigenenergies are at least doubly degenerate.

Next, we consider the electrons on the lattice with periodic potentials. The Bloch theorem states that the eigenstates of the Hamiltonian $\mathcal{H}$ are represented as $\{|\psi_{n\boldsymbol{k}}\rangle\}$, which satisfy $\mathcal{H}|\psi_{n\boldsymbol{k}}\rangle = E_{n\boldsymbol{k}}|\psi_{n\boldsymbol{k}}\rangle$. Here, $\boldsymbol{k}$ is called the Bloch wave number. The wave functions $|\psi_{n\boldsymbol{k}}\rangle$ are written by the periodic state $|u_{n\boldsymbol{k}}\rangle$ as $|\psi_{n\boldsymbol{k}}\rangle = e^{i\boldsymbol{k}\cdot\boldsymbol{r}}|u_{n\boldsymbol{k}}\rangle$. Now the Bloch Hamiltonian $H(\boldsymbol{k})$ is defined as $H(\boldsymbol{k}) = e^{-i\boldsymbol{k}\cdot\boldsymbol{r}}\mathcal{H}e^{i\boldsymbol{k}\cdot\boldsymbol{r}}$. The Bloch states $|u_{n\boldsymbol{k}}\rangle$ are obtained by solving the Schrödinger equation for the Hamiltonian $H(\boldsymbol{k})$,

$$\begin{aligned} H(\boldsymbol{k})|u_{n\boldsymbol{k}}\rangle &= e^{-i\boldsymbol{k}\cdot\boldsymbol{r}}\mathcal{H}|\psi_{n\boldsymbol{k}}\rangle \\ &= E_{n\boldsymbol{k}}e^{-i\boldsymbol{k}\cdot\boldsymbol{r}}|\psi_{n\boldsymbol{k}}\rangle \\ &= E_{n\boldsymbol{k}}|u_{n\boldsymbol{k}}\rangle\,. \end{aligned} \tag{2.2}$$

Considering the system with the time-reversal symmetry, the Bloch Hamiltonian $H(\boldsymbol{k})$ satisfies $\Theta H(\boldsymbol{k})\Theta^{-1} = H(-\boldsymbol{k})$. [1] This equation guaranties that the energy bands of the system with the time-reversal symmetry make pairs and the states with the Bloch wave number $\boldsymbol{k}$ and the Bloch wave number $-\boldsymbol{k}$ have the same energies. The pairs of the bands, $u_{n,\boldsymbol{k}}$ and $u_{m,\boldsymbol{k}}$, are the Kramers pair.

The Bloch space $\{\boldsymbol{k}\}$ is periodic with the reciprocal lattice vectors $\boldsymbol{G}$. For special wave numbers that satisfy $\boldsymbol{k} = -\boldsymbol{k} + \boldsymbol{G}$, the Bloch Hamiltonian $H(\boldsymbol{k})$ commute with the time-reversal operator Θ. These wave numbers are called *the time-reversal invariant momentum* (TRIM). The TRIM of the honeycomb lattice is shown in Fig. 2.1 (b). For d dimensional systems, the TRIM can be expressed as $\sum_{i=1}^{d} n_i\boldsymbol{G}_i/2$, where $\boldsymbol{G}_i$ is i-th reciprocal vector and n_i takes 0 or 1. For d-dimensional systems, the number of the TRIM is 2^d.

[1] To calculate $e^{i\boldsymbol{k}\cdot\boldsymbol{r}}\Theta\mathcal{H}\Theta^{-1}e^{-i\boldsymbol{k}\cdot\boldsymbol{r}}$, one can obtain

$$\begin{aligned} e^{i\boldsymbol{k}\cdot\boldsymbol{r}}\Theta\mathcal{H}\Theta^{-1}e^{-i\boldsymbol{k}\cdot\boldsymbol{r}} &= \Theta e^{-i\boldsymbol{k}\cdot\boldsymbol{r}}\mathcal{H}e^{i\boldsymbol{k}\cdot\boldsymbol{r}}\Theta^{-1} \\ &= \Theta H(\boldsymbol{k})\Theta^{-1}. \end{aligned}$$

On the other hand, by using $\Theta\mathcal{H}\Theta^{-1} = \mathcal{H}$, one can obtain

$$e^{i\boldsymbol{k}\cdot\boldsymbol{r}}\Theta\mathcal{H}\Theta^{-1}e^{-i\boldsymbol{k}\cdot\boldsymbol{r}} = e^{i\boldsymbol{k}\cdot\boldsymbol{r}}\mathcal{H}e^{-i\boldsymbol{k}\cdot\boldsymbol{r}} = H(-\boldsymbol{k}).$$

Hence $\Theta H(\boldsymbol{k})\Theta^{-1} = H(-\boldsymbol{k})$.

2.1.2 The $\mathbb{Z}_2$ index for the quantum spin Hall phase

Next, we introduce the $\mathbb{Z}_2$ index, which is the topological number for the quantum spin Hall systems. First, we define *the sewing matrix* for the system with the time-reversal symmetry

$$w_{\alpha\beta}(\boldsymbol{k}) = \langle u_{\alpha-\boldsymbol{k}}|\Theta|u_{\beta\boldsymbol{k}}\rangle\,. \tag{2.3}$$

Here, $\alpha, \beta = 1, 2, \cdots, N$ is the index of the Kramers pairs. The sewing matrix w is the U($2N$) matrix. To show the unitarity, let us calculate the matrix element of w,

$$\begin{aligned}\sum_\alpha w^\dagger_{\gamma\alpha}(\boldsymbol{k})w_{\alpha\beta}(\boldsymbol{k}) &= \sum_\alpha w^*_{\alpha\gamma}(\boldsymbol{k})w_{\alpha\beta}(\boldsymbol{k}) \\ &= \sum_\alpha \langle\Theta u_{\gamma\boldsymbol{k}}|u_{\alpha-\boldsymbol{k}}\rangle\,\langle u_{\alpha-\boldsymbol{k}}|\Theta u_{\beta\boldsymbol{k}}\rangle \\ &= \langle\Theta u_{\gamma\boldsymbol{k}}|\Theta u_{\beta\boldsymbol{k}}\rangle \\ &= \langle u_{\beta\boldsymbol{k}}|u_{\gamma\boldsymbol{k}}\rangle \\ &= \delta_{\beta\gamma}.\end{aligned} \tag{2.4}$$

Hence the matrix w is unitary. The sewing matrix w also has the property

$$w_{\beta\alpha}(-\boldsymbol{k}) = -w_{\alpha\beta}(\boldsymbol{k})^2. \tag{2.5}$$

The property shows that the sewing matrix $w(\boldsymbol{k})$ is skew-symmetric if the $\boldsymbol{k}$ is at the TRIM. Hence the Pfaffian can be defined at the TRIMs.

Now we can define the $\mathbb{Z}_2$ index ν for the time-reversal symmetric systems:

$$(-1)^\nu = \prod_i \frac{\mathrm{Pf}[w(\Lambda_i)]}{\sqrt{\det[w(\Lambda_i)]}} \tag{2.6}$$

where Λ_i is the i-th TRIM and multiplication is taken over all the TRIMs. Pf$[w]$ is the Pfaffian of w. To consider the property of the Pfaffian, $\det[w] = \mathrm{Pf}[w]^2$, we can find that the $\mathbb{Z}_2$ index ν takes 0 or 1. Hence the $\mathbb{Z}_2$ index is a topological number and the ν is not changed unless the band gap is closed. The $\mathbb{Z}_2$ index is one of the topological order, which characterizes the quantum spin Hall phase. For $\nu = 0$, the system is topologically trivial, while for $\nu = 1$, the system is in the quantum spin Hall phase. In the phase, the spin Hall conductance is finite and the spin current is localized on the edge of the system. In the next section, we demonstrate it through the concrete model, the Kane-Mele model for the quantum spin Hall effect.

2.1.3 The tight-binding model for the quantum spin Hall phase – the Kane-Mele model

In this section, we review the Kane-Mele model that is a typical model of the quantum spin Hall phase. The Kane-Mele model is a tight-binding model for the s-states in a honeycomb lattice. In 2005, C. L. Kane and E. J. Mele proposed the model for the quantum spin Hall state [7, 8].

[2] We can show the equation as following:

$$\begin{aligned}w_{\beta\alpha}(-\boldsymbol{k}) &= \langle u_{\beta\boldsymbol{k}}|\Theta|u_{\alpha-\boldsymbol{k}}\rangle \\ &= -\langle u_{\alpha-\boldsymbol{k}}|\Theta|u_{\beta\boldsymbol{k}}\rangle \\ &= -w_{\alpha\beta}(\boldsymbol{k}).\end{aligned}$$

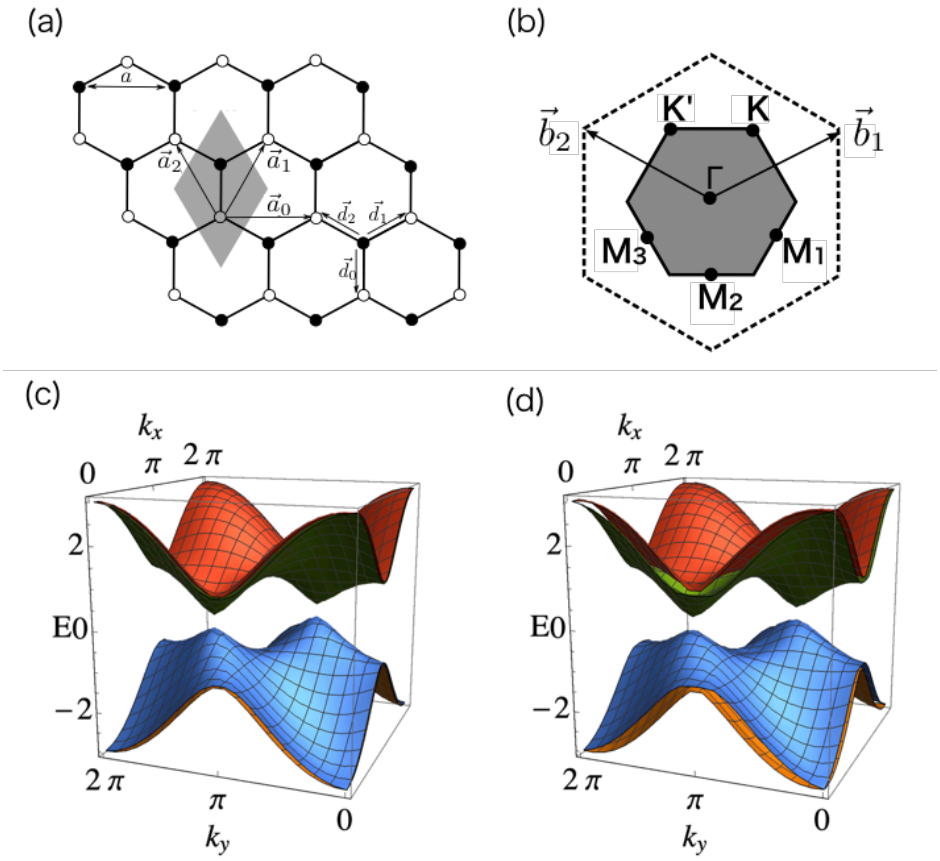

Figure 2.1: (a) The lattice structure of the honeycomb lattice. A unit cell is shaded. The black and white sites form the sublattice degree of freedom. We denote them as A (B) for the black (white) sites. (b) The first Brillouin zone of the honeycomb lattice, which is shaded in the figure. There are two high symmetric points K and K'. In addition, the time reversal invariant momentum, Γ, M_1, M_2, M_3 are shown. (c)-(d) The bulk bands of the Kane-Mele model. The parameters are set to $t = 1, \lambda_{SO} = 0.05$ and (c) $\lambda_\nu = \lambda_{SO}, \lambda_R = \lambda_{SO}$, (d) $\lambda_\nu = 6\lambda_{SO}, \lambda_R = 3\lambda_{SO}$. As seen in later, the model is in (c) the quantum spin Hall phase and (d) trivial phase.

Graphene is a two dimensional honeycomb lattice composed of carbon atoms. A carbon atom has six electrons, which forms a ground-state with electron configuration of $1s^2 2s^2 2p^2$. In a graphene sheet, three of the outer four electrons form three sp^2 orbitals and the rest remains in 2p orbital. The sp^2 orbital electrons yield the σ-bonds, on the other hand, the 2p-electron forms the π-electron, which moves as a free electron. The energy of the sp^2-electrons is much less than that of π-electrons and the elements in the carbon group have four valence electrons. Hence the tight-binding approximation for the π-electrons are justified.

The honeycomb lattice has sublattices so a unit cell consists of two individual sites A and B (see Fig. 2.1 (a)). The figure shows the lattice vectors $\boldsymbol{a}_1$ and $\boldsymbol{a}_2$. The shaded region is a unit cell. The vectors $\boldsymbol{d}_i$ (i=1, 2, 3) represent the nearest-neighbour vector between the sites. The Brillouin zone and the reciprocal lattice vectors $\boldsymbol{b}_1$ and $\boldsymbol{b}_2$ are shown in Fig. 2.1 (b). Here, the high symmetry points, K and K', are shown. There are four TRIMs, Γ, M_1, M_2 and M_3.

The Kane-Mele model is a tight-binding model for π-electrons in a honeycomb lattice, which contains the terms for the nearest neighbour hopping, the next-nearest neighbour

spin-orbit coupling, the nearest neighbour Rashba effect and the staggered potentials:

$$\begin{aligned}\mathcal{H}_{\rm KM} &= t\sum_{\langle ij\rangle}\hat{c}_i^\dagger\hat{c}_j + i\lambda_{\rm SO}\sum_{\langle\langle ij\rangle\rangle}\nu_{ij}\hat{c}_i^\dagger\hat{s}^z\hat{c}_j \\ &\quad + i\lambda_{\rm R}\sum_{\langle ij\rangle}\hat{c}_i^\dagger\{\boldsymbol{s}\times\boldsymbol{d}_{ij}\}^z\hat{c}_j + \lambda_\nu\sum_i\xi_i\hat{c}_i^\dagger\hat{c}_i. \end{aligned} \tag{2.7}$$

where $\hat{c}_i = (\hat{c}_{iA\uparrow}\ \hat{c}_{iA\downarrow}\ \hat{c}_{iB\uparrow}\ \hat{c}_{iB\downarrow}\ )^{\rm T}$ are the annihilation operators of the π-electrons in i-th unit cell and $\boldsymbol{s}$ is the spin operator The first term is the hopping term between the nearest-neighbour sites. The second term is the spin-orbit coupling term between next-nearest-neighbour sites. The factor $\nu_{ij} = \pm 1$ is the sign of $\hat{\boldsymbol{d}}_1 \times \hat{\boldsymbol{d}}_2$. Here $\hat{\boldsymbol{d}}_{1,2}$ are the nearest-neighbour bond vectors that make the trajectory between the i-th site and the j-th site. The factor ν_{ij} corresponds to the z component of the angular momentum $L_z = (\boldsymbol{r}\times\boldsymbol{p})_z$. The third term is the Rashba effect term between the nearest-neighbour sites. Here $\boldsymbol{d}_{ij}$ is the nearest-neighbour vector from the i-th site to the j-th site. This term is from the effect by the substrate and the electric field perpendicular to the lattice. This term breaks the mirror symmetry with respect to the lattice plane and conservation of s_z. The fourth term is the staggered potential term, which represent the difference of the site potential between the sublattices $\{A, B\}$. The ξ_i equals to $+1$ (-1) for electrons at A (B) site. This term violates the inversion symmetry.

Next, we consider the bulk Hamiltonian of the Kane-Mele model. After the Fourier transformation $\hat{c}_i = \frac{1}{\sqrt{N}}\sum_{\boldsymbol{k}\in BZ} e^{-i\boldsymbol{k}\cdot\boldsymbol{R}_i}\hat{c}_{\boldsymbol{k}}$, the Hamiltonian of the Kane-Mele model is written as $\mathcal{H} = \sum_{\boldsymbol{k}} H(\boldsymbol{k})$ where

$$H(\boldsymbol{k}) = \sum_{a=1}^{5} d_a\Gamma^a + \sum_{a<b=1}^{5} d_{ab}\Gamma^{ab}. \tag{2.8}$$

Here, $\{\Gamma^a, \Gamma^{ab}\}$ are the generators of the 4×4 hermitian matrices, which are $\Gamma^{(1,2,3,4,5)} = (\sigma_x\otimes I,\ \sigma_z\otimes I,\ \sigma_y\otimes s_x,\ \sigma_y\otimes s_y,\ \sigma_y\otimes s_z)$ and $\Gamma^{ab} = [\Gamma^a, \Gamma^b]/2i$. The coefficients d are shown in the table below [7]. In the table, x and y span in the first Brillouin zone.

d_1	$t(1+2\cos x\cos y)$	d_{12}	$-2t\cos x\sin y$
d_2	λ_ν	d_{15}	$\lambda_{\rm SO}(2\sin 2x - 4\sin x\cos y)$
d_3	$\lambda_{\rm R}(1-\cos x\cos y)$	d_{23}	$-\lambda_{\rm R}\cos x\sin y$
d_4	$-\sqrt{3}\lambda_{\rm R}\sin x\sin y$	d_{24}	$\sqrt{3}\lambda_{\rm R}\sin x\cos y$
otherwise : 0			

If the Rashba term vanishes ($\lambda_{\rm R} = 0$), the total s_z is conserved. In this case, the Hamiltonian can be block diagonalized with respect to the s_z basis

$$\mathcal{H} = \begin{pmatrix} \mathcal{H}_\uparrow & 0 \\ 0 & \mathcal{H}_\downarrow \end{pmatrix}. \tag{2.9}$$

and one can calculate the Chern number $\nu_\uparrow(\nu_\downarrow)$ for each block Hamiltonians $\mathcal{H}_\uparrow$ $(\mathcal{H}_\downarrow)$. The number ν_s is called *the spin Chern number*. Due to the time-reversal symmetry, the total Chern number $\nu = \nu_\uparrow + \nu_\downarrow$ is zero. However, for the quantum spin Hall systems, the difference of the Chern numbers $\nu_s = \nu_\uparrow - \nu_\downarrow$ is nonzero. The spin Chern number is related to the spin Hall conductivity as $\sigma^s_{xy} = (e/4\pi)(\nu_\uparrow - \nu_\downarrow)$, hence the spin Hall conductivity in the quantum spin Hall phase is nonzero. In the phase, the edge states appear for each block Hamiltonians and the currents for up and down spins have opposite directions. For the system without s_z conservation, the $\mathbb{Z}_2$ index determines the quantum spin Hall phase. The phase diagram determined by the $\mathbb{Z}_2$ index is shown in Fig. 2.2 (a) for two parameters $\lambda_{\rm R}$

and λ_ν, normalized by $\lambda_{\rm SO}$. If there are only the hopping and the spin-orbit coupling, the system is in the quantum spin Hall phase. To increase $\lambda_{\rm R}$ and λ_ν, the band gap is closed and the topological phase transition occurs from the quantum spin Hall phase to the trivial insulator phase.

In next, we analyze the edge spectrum for the Kane-Mele model. To analyze the edge states, we consider the system on the cylinder geometry [Fig. 2.2 (b)]. To achieve this, the system takes the periodic boundary condition for x direction as the open boundary condition for y direction. Thus, we take the Fourier transformation $\hat{c}_{x,y} = \frac{1}{\sqrt{N}} \sum_{k_x \in 0,2\pi} e^{-ik_x \cdot \boldsymbol{R}_x} \hat{c}_{k_x,y}$ to the Hamiltonian along the x direction. The spectrum for the Kane-Mele model under those conditions are shown in Fig. 2.2 (c)-(d) as a function of k_x. We fixed the parameters $t = 1$, $\lambda_{\rm SO} = 0.05$. The other parameters are set to (c) $\lambda_{\rm R}/\lambda_{\rm SO} = 1$, $\lambda_\nu/\lambda_{\rm SO} = 1$ and (d) $\lambda_{\rm R}/\lambda_{\rm SO} = 3$, $\lambda_\nu/\lambda_{\rm SO} = 6$. The system of Fig. 2.2 (c) is in the quantum spin Hall phase and the system of Fig. 2.2 (d) is in the trivial phase. As seen in Fig. 2.2 (c), the system has the dispersive states in the band-gap, which is localized on the edge. This existence of the edge states shows the bulk-edge correspondence between the non-trivial $\mathbb{Z}_2$ index and the edge states. On the other hand, in Fig. 2.2 (d), there are no edge state in the band gap. This is because the system is in the trivial insulator phase.

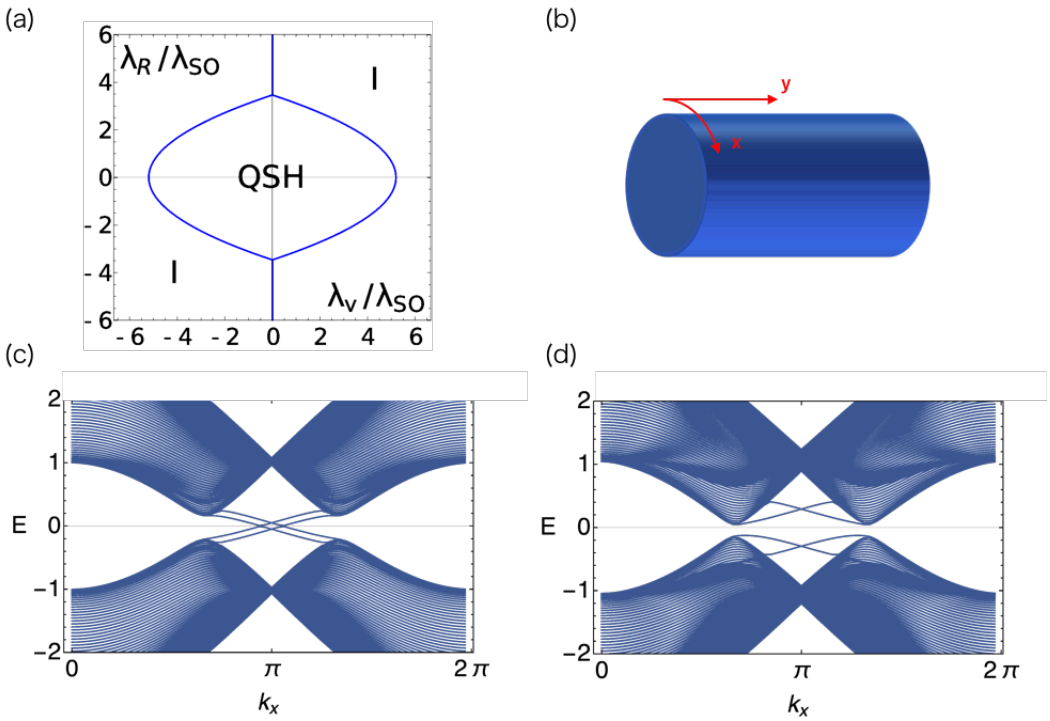

Figure 2.2: (a) The phase diagram of the Kane-Mele model. On the blue line, the band gap is closed. The inner region of the blue line is the quantum spin Hall phase. The outer region is trivial insulator phase. (b) The schematic picture of the cylinder geometry. There are open boundaries along the y direction. (c)-(d) The energy spectrum of the Kane-Mele model with the cylinder geometry. Parameters are set to $t = 1$, $\lambda_{\rm SO} = 0.05$, (c) $\lambda_{\rm R}/\lambda_{\rm SO} = 1$, $\lambda_\nu/\lambda_{\rm SO} = 1$ and (d) $\lambda_{\rm R}/\lambda_{\rm SO} = 3$, $\lambda_\nu/\lambda_{\rm SO} = 6$. The model is in (c) the quantum spin Hall phase and (d) the trivial phase.

2.2 Topological insulator phases

In this section, we introduce the strong topological insulator and the weak topological insulator, which is a typical topological phase in three dimensions. As seen in the previous section, the quantum spin Hall effect appears in two dimensions where the spin-orbit coupling is essential. The quantum spin Hall phase is characterized by the $\mathbb{Z}_2$ index, which is defined for the system under the time-reversal symmetry. To generalize the quantum spin Hall phase to three dimensions, the Fu-Kane-Mele model is proposed [9]. The model is a tight-binding model of s states on a diamond lattice with the spin-orbit coupling. In three dimensions, four $\mathbb{Z}_2$ indices classify the topological phases into the strong topological insulator phases and the weak topological insulator phases. The strong topological insulators are robust against disorders, while the weak topological insulators can be continuously connected to the trivial insulators.

2.2.1 The $\mathbb{Z}_2$ indices for strong and weak topological insulator phases

In this section, we consider topological insulator phase, which is the extension of the quantum spin Hall phase in three dimensions. In the topological insulator phase, the topological spin current emerges not in the edge but the two-dimensional surfaces. Here we introduce the $\mathbb{Z}_2$ index for the topological insulator phase. Naturally, the definition of the $\mathbb{Z}_2$ index can be extended for each two-dimensional surfaces. To define the $\mathbb{Z}_2$ index in this way, let us consider the TRIM in three-dimensional Brillouin zone. We denote the eight TRIMs in three-dimensions as $\Lambda_{n_1,n_2,n_3} = (n_1\pi, n_2\pi, n_3\pi)$ in the basis of the reciprocal vectors ($n_j \in \{0,1\}$). On the TRIMs, the $\mathbb{Z}_2$ index is defined as

$$\delta_{n_1,n_2,n_3} = \frac{\mathrm{Pf}[w(\Lambda_{n_1,n_2,n_3})]}{\sqrt{\det[w(\Lambda_{n_1,n_2,n_3})]}} \tag{2.10}$$

We note the δ_{n_1,n_2,n_3} is a topological number because it is quantized to -1 or 1. Here, we consider the $\mathbb{Z}_2$ index defined for each of the two-dimensional surfaces, such as

$$(-1)^{\nu_j} = \prod_{n_{i\neq=j}\in 0,1; n_j=1} \delta_{n_1,n_2,n_3}, \tag{2.11}$$

where one component of the wave vector is fixed to π. This is a natural extension of the $\mathbb{Z}_2$ index in the two-dimensional plane, which is called *the weak $\mathbb{Z}_2$ indices*. On the other hand, one can define three-dimensional version of the $\mathbb{Z}_2$ index as

$$(-1)^{\nu_0} = \prod_{n_{i\neq=j}\in 0,1} \delta_{n_1,n_2,n_3}, \tag{2.12}$$

which is called *the strong $\mathbb{Z}_2$ index* and it characterizes the topological insulator phase.

Analogous to the quantum spin Hall insulators, if the system has non-trivial $\mathbb{Z}_2$ index, the system with open boundary condition has the in-gap surface state on the plane. The topological insulator is the insulators with the non-trivial strong $\mathbb{Z}_2$ index. The schematic picture for the surface state is shown in Fig. 2.3. Figure 2.3 (a) shows the bulk spectrum and the surface states for the topological insulator. If the strong $\mathbb{Z}_2$ index is non-trivial, odd number of the in-gap surface state that connect the conduction band and the valence band emerge. On the other hand, if the strong $\mathbb{Z}_2$ index is trivial, there are even number of the surface states in gap and these surface states are not topological, because these surface states can be removed from the band gap by adiabatic transformation. In next, we show the surface states of the concrete model, the Fu-Kane-Mele model, of the topological insulator and also demonstrate the strong $\mathbb{Z}_2$ index characterize the topological insulator phase.

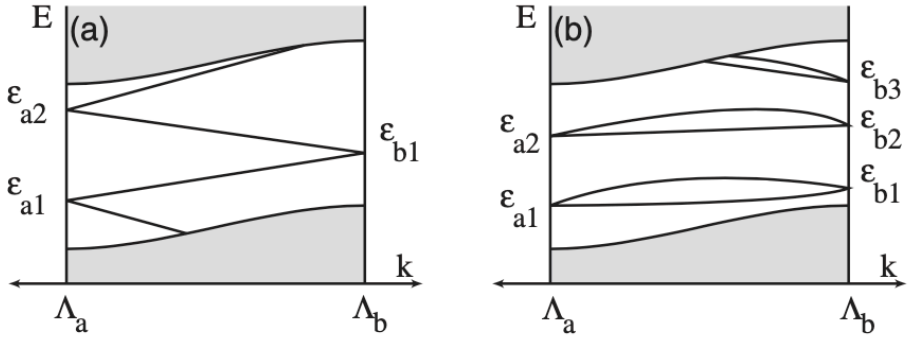

Figure 2.3: From Ref. [9]. Schematic picture of the surface state and bulk spectrum as a function of momentum between two TRIMs, Λ_a and Λ_b. (a) The surface states for the strong topological insulators. (b) The surface states for the insulator with trivial strong $\mathbb{Z}_2$ index. In (a), the dispersive edge states connects the conduction band and the valence band but not in (b).

2.2.2 The tight-binding model for the topological insulator phase – the Fu-Kane-Mele model

L. Fu, C. L. Kane and E. J. Mele proposed a tight-binding model on a diamond lattice with the spin-orbit coupling as the generalization of the quantum spin Hall effect in three dimensions [9]. This model is called the Fu-Kane-Mele model. The model Hamiltonian is defined as

$$\mathcal{H} = \sum_{\langle ij \rangle} t_{ij} c_i^\dagger c_j + i\lambda_{\rm SO} \sum_{\langle\langle ij \rangle\rangle} c_i^\dagger \boldsymbol{s} \cdot \left(\boldsymbol{d}_{ij}^1 \times \boldsymbol{d}_{ij}^2 \right) c_j. \tag{2.13}$$

Here, $c_i^{\rm T} = (c_{i,\uparrow}, c_{i,\downarrow})$ if the annihilation operators of the electron at the i-th site and the $\boldsymbol{s}$ is a spin operator. The first term is the nearest-neighbor hopping term and the second term is the next-nearest-neighbor spin-orbit coupling term. There are four bonds for each of sites in the diamond lattice and the different hopping parameters labeled t_1 to t_4 are introduced as shown in Fig. 2.4 (a). The vectors $\boldsymbol{d}_{ij}^{1,2}$ are the two nearest-neighbor bonds traversed between sites i and j as shown in Fig. 2.4 (a). Both time-reversal symmetry and inversion symmetry are preserved in the Fu-Kane-Mele model.

In next, we consider the bulk Hamiltonian of the Fu-Kane-Mele model. To take the Fourier transformation $\hat{c}_i = \frac{1}{\sqrt{N}} \sum_{\boldsymbol{k} \in BZ} e^{-i\boldsymbol{k}\cdot\boldsymbol{R}_i} \hat{c}_{\boldsymbol{k}}$, we obtain the bulk Hamiltonian of the present model as

$$H(\boldsymbol{k}) = \begin{pmatrix} P(\boldsymbol{k}) & S(\boldsymbol{k})I \\ S(\boldsymbol{k})^* I & -P(\boldsymbol{k}) \end{pmatrix}, \tag{2.14}$$

where the basis is $c_{\boldsymbol{k}}^{\rm T} = (c_{\boldsymbol{k}A\uparrow}, c_{\boldsymbol{k}A\downarrow}, c_{\boldsymbol{k}B\uparrow}, c_{\boldsymbol{k}B\downarrow})$, I denotes the 2×2 identity matrix, and both $S(\boldsymbol{k})I$ and $P(\boldsymbol{k})$ are the 2×2 matrices. The $S(\boldsymbol{k})$ is the contribution of the hopping term, which is defined as

$$S(\boldsymbol{k}) = \sum_{\mu} t_\mu e^{i\boldsymbol{k}\cdot\boldsymbol{d}_\mu}. \tag{2.15}$$

On the other hand, the matrix $P(\boldsymbol{k})$ is the contribution of the spin orbit coupling term, which is defined as

$$P(\boldsymbol{k}) = i\lambda_{\rm SO} \sum_{\mu,\nu} e^{i\boldsymbol{k}\cdot(-\boldsymbol{d}_\mu + \boldsymbol{d}_\nu)} \boldsymbol{S} \cdot (-\boldsymbol{d}_\mu \times \boldsymbol{d}_\nu). \tag{2.16}$$

Here, $\boldsymbol{d}_\mu$ ($\mu = 1, 2, 3, 4$) is the vector between the μ-th nearest-neighbour sites associated with the hopping parameters as shown in 2.4 (a).

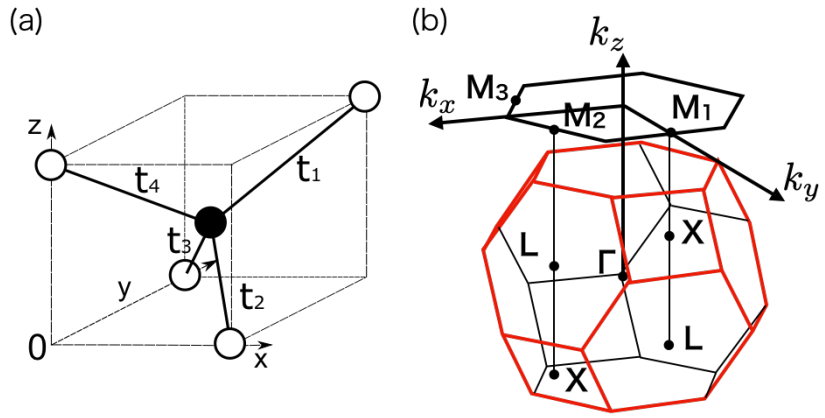

Figure 2.4: (a) A part of the diamond lattice is shown. In the diamond lattice, each of sites has four bonds. The hopping parameters t_j $(j = 1, 2, 3, 4)$ corresponding with the bonds are shown. (b) The first Brillouin zone in three-dimensions and the first Brillouin zone projected to two-dimensional plane to the z direction are shown.

To use the notation, one can obtain the eigenvalues of the Hamiltonian as

$$E_{\pm}(\boldsymbol{k}) = \pm\sqrt{|S(\boldsymbol{k})|^2 + |P_{11}(\boldsymbol{k})|^2 + |P_{12}(\boldsymbol{k})|^2}. \tag{2.17}$$

Because of the inversion symmetry and the time-reversal symmetry, the eigenvalues are doubly degenerated. To simplify the matrix $P(\boldsymbol{k})$, we introduce the vector $\boldsymbol{B}(\boldsymbol{k}) = \sum_\mu e^{i\boldsymbol{k}\cdot\boldsymbol{d}_\mu}\boldsymbol{d}_\mu$. To use the vector, $P(\boldsymbol{k})$ is deformed as

$$P(\boldsymbol{k}) = -i\lambda_{\rm SO}\boldsymbol{S}\cdot(\boldsymbol{B}(-\boldsymbol{k})\times\boldsymbol{B}(\boldsymbol{k}))\,. \tag{2.18}$$

Having the expression, we can show the $P(\boldsymbol{k})$ is zero at the TRIMs because $\boldsymbol{B}(-\boldsymbol{k}) = \boldsymbol{B}(\boldsymbol{k})$ at the TRIM.

Figure 2.5 (a) shows the bulk bands of the model with $t \equiv t_1 = t_2 = t_3 = t_4 = 1$ and $\lambda_{\rm SO} = 0.125$ as a solid line. The horizontal line shows the wave vectors connecting symmetry points, where $\Gamma = (0,0,0), L = (1/2,1/2,1/2), K = (3/4,3/4,0), W = (1,1/2,0)$ and $X = (1,0,0)$ in units of $2\pi/a$ for lattice constant a. For the system with isotropic hopping parameters, one can see the band gap is closed at X as following. The band gap can be calculated by Eq. 2.17, where $P(\boldsymbol{k}) = 0$ because X is a TRIM. Combining it to the Eq. 2.15 which shows $S(\boldsymbol{k}) = 0$ for the isotropic case, the band gap in Eq. 2.17 is closed at the X. Hence, the Fu-Kane-Mele model with the isotropic hopping parameters is the Dirac semimetal, in which Dirac cones appear at the TRIMs. To change one of the hopping parameters, the band gap is open, because $S(\boldsymbol{k})$ can be finite. The dashed line in this figure shows the bulk bands with $\delta t_1 = 0.4$, in which the band gap is open. Hence, we can consider the topological phase for the insulators with anisotropic hopping parameters. The $\mathbb{Z}_2$ indices for the model about the difference of two hopping parameters δt_1 and δt_2 is shown in Fig. 2.5 (b). We note that the bond vectors associated with t_1 and t_2 are denoted by using the Miller indices as (111) and $(1\bar{1}\bar{1})$, respectively. In this figure, the strong $\mathbb{Z}_2$ index and the Miller indices associated with t_1 and t_2 is shown. The shaded region shows the (strong) topological insulator phase, whereas the white region shows the weak topological insulator phase. On the solid and dashed line, the band gap is closed and the solid line is the phase boundary of the strong and weak topological insulators. The Miller indices have the relation to the weak $\mathbb{Z}_2$ indices (ν_1, ν_2, ν_3). Actually, the weak $\mathbb{Z}_2$ indices are $\nu_0; (\nu_1, \nu_2, \nu_3) = 1; (1,0,0)$ in the top triangle region and $\nu_0; (\nu_1, \nu_2, \nu_3) = 0; (1,0,0)$ in the bottom triangular region. On the

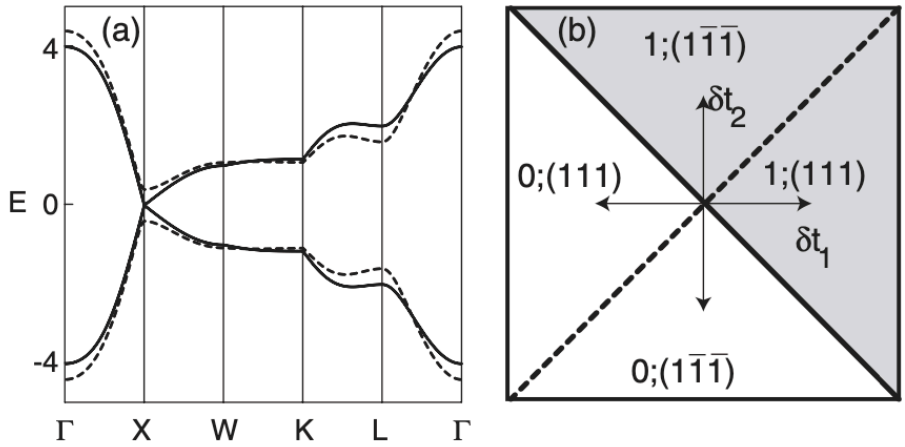

Figure 2.5: From Ref. [9]. (a) The bulk bands of the model with $t = 1$ and $\lambda_{\rm SO} = 0.125$ are shown as a solid line for the wave vectors connecting symmetry points. The symbols for the symmetry points are defined in the main text. The dashed line is the bulk bands with $\delta t_1 = 0.4$, in which the band gap is open. (b) The phase diagram of the Fu-Kane-Mele model as a function of δt_1 and δt_2. In the shaded region, the system is in the (strong) topological insulator phase, while in the white region the system is in the weak topological insulator phase.

other hand, the $\mathbb{Z}_2$ indices are $\nu_0; (\nu_1, \nu_2, \nu_3) = 1; (1, 1, 1)$ in the right triangular region and $\nu_0; (\nu_1, \nu_2, \nu_3) = 0; (1, 1, 1)$ in the left triangular region.

Finally, we investigate the surface states of the model. For the sake to study the surface state, we consider the slab geometry where the model is under the open boundary condition for the z axis but periodic boundary conditions for the x and y axes. Under these boundary conditions, the wave vector in the xy-plane is defined in the Brillouin zone projected about the z axis, as shown in Fig. 2.4 (b). Here, M_1, M_2 and M_3 are the symmetry points in the two-dimensional Brillouin zone. Figure 2.6 shows the bulk spectrum and the surface states are shown for (a) $\delta t_1 = 0.5$ and (b) $\delta t_1 = -0.2$. The $\mathbb{Z}_2$ index is 1 for the system in (a) under periodic boundary condition, hence the system is in the topological insulator phase. Corresponding with the phase, the surface states appear in the energy gap. On the other hand, the $\mathbb{Z}_2$ index is 0 for the system in (b). Thus, there are no surface state in the energy gap.

2.3 The entanglement Chern number for topological phases

The quantum entanglement in many-body systems is useful to describe a quantum phase of the system [76–80]. In particular, the quantum entanglement of insulators describes the topological phase of the system [81–84]. In this section, we review another topological invariant, the entanglement Chern number for both the quantum spin Hall phase and the topological insulator phase [85–89]. The entanglement Chern number is the Chern number for the ground state of the entanglement Hamiltonian, which is constructed by tracing out certain subspaces of a given system [83, 84, 86]. In the following, we show the definition of the entanglement Hamiltonian and the entanglement Chern number. Then, we review its characterization for the quantum spin Hall and the topological insulator phases.

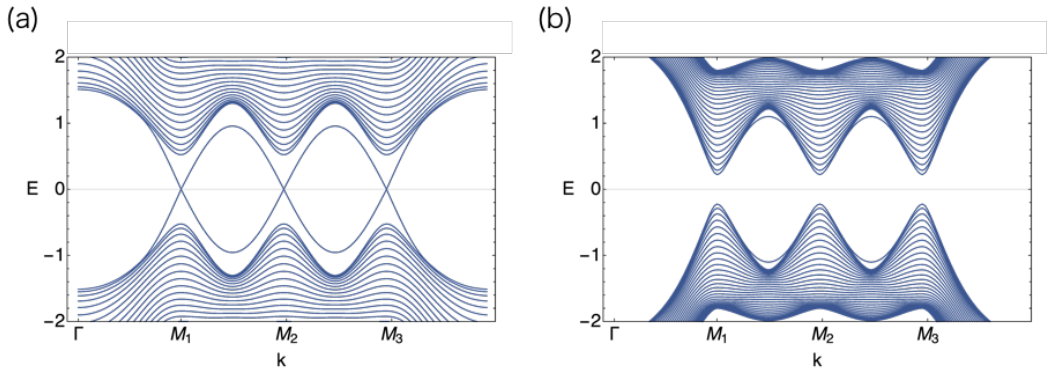

Figure 2.6: The bulk spectrum and the edge states are shown for (a) $\delta t_1 = 0.5$ and (b) $\delta t_1 = -0.2$ for the two-dimensional Brillouin zone projected about the z axis. In (a), the system is in the topological insulator phase and the corresponding surface states appear in the energy gap. On the other hand, in (b), the system has trivial $\mathbb{Z}_2$ index and no surface state appears in the energy gap.

2.3.1 Definition of the entanglement Chern numbers

Here, we introduce the entanglement Chern number. Firstly, let us define the entanglement Hamiltonian. We consider the tight-binding Hamiltonian for non-interacting fermions as $\mathcal{H} = \sum_{kl} t_{kl} \hat{c}_k^\dagger \hat{c}_l$ where $\hat{c}_k^\dagger$ is a creation operator of k-th fermion. For this Hamiltonian, we define $|\psi_0\rangle$ as the ground-state of the Hamiltonian. Next, we consider the density matrix ρ. To think about the pure state of $|\psi_0\rangle$, the ρ is defined as $|\psi_0\rangle \langle\psi_0|$. Here, we divide the system into A and B in order to consider the entanglement for the subsystems. By tracing out the density matrix about subsystem B, the reduced density matrix for A is defined as

$$\begin{aligned} \rho_A &= \mathrm{Tr}_B\, \rho \\ &= \mathrm{Tr}_B\, |\psi_0\rangle \langle\psi_0| \,. \end{aligned} \tag{2.19}$$

Similarly, the reduced density matrix for B is defined as $\rho_B = \mathrm{Tr}_A\, \rho$. Here, we introduce the entanglement Hamiltonian for subsystem A as

$$\rho_A = e^{-\mathcal{H}_A}. \tag{2.20}$$

Here, the $\mathcal{H}_A$ is the entanglement Hamiltonian. In the similar way, the entanglement Hamiltonian for subspace B is defined. We note that the entanglement Hamiltonian contains information about the entanglement between the subsystems.

Next, we introduce the entanglement Chern number in two dimensions. Let $\mathcal{B}$ be the two dimensions Brillouin zone spanned by the wave vector $\boldsymbol{k} = (k_1, k_2)$. Then, the entanglement Chern number is defined as the Chern number for the entanglement Hamiltonian $\mathcal{H}_\mathrm{A}$:

$$c_\mathrm{A} = \frac{1}{2\pi i} \int_{\mathcal{B}} F_{12}(\boldsymbol{k}) d^2k, \tag{2.21}$$

where $F_{12}(\boldsymbol{k}) = \epsilon_{ij} \partial_{k_i} \psi_\mathrm{A}^\dagger(\boldsymbol{k}) \partial_{k_j} \psi_\mathrm{A}(\boldsymbol{k})$ is the Berry curvature of the ground state (negative energy) multiplet ψ_A of the entanglement Hamiltonian $\mathcal{H}_\mathrm{A}$. For free fermion systems, it is convenient to use the correlation matrix instead of the entanglement Hamiltonians. The correlation matrix for the subsystem A is defined as $(C_\mathrm{A})_{ij} = \langle c_i^\dagger c_j \rangle = \mathrm{Tr}[\rho_\mathrm{A} c_i^\dagger c_j]$, where $c_i^\dagger$ is the creation operator of an electron in the subsystem A. Then, it turns out [90] that C_A is related with $\mathcal{H}_\mathrm{A}$ such that

$$\mathcal{H}_\mathrm{A}^T = \ln[(1 - C_\mathrm{A})/C_\mathrm{A}]. \tag{2.22}$$

By calculating the Chern number of the correlation matrix, we can obtain the Chern number of the entanglement Hamiltonian. [85]

To contemplate the quantum spin Hall phase and the topological insulator phases, it is useful to choose the subsystem as up- and down-spins in the system. In following sections, we describe how the entanglement Chern number works to characterize the quantum spin Hall phase and the topological insulator phases.

2.3.2 The entanglement Chern number for the quantum spin Hall phase

Here we contemplate the quantum spin Hall phase. First of all, let us consider there is spin orbit coupling but the z-component of total spin (s_z) is conserved. For the Kane-Mele model, this case corresponds that the Rashba term is vanished. In this case, the Bloch Hamiltonian $H(\boldsymbol{k})$ can be block diagonalized for s_z as

$$H(\boldsymbol{k}) = \begin{pmatrix} H_\uparrow(\boldsymbol{k}) & 0 \\ 0 & H_\downarrow(\boldsymbol{k}) \end{pmatrix}, \tag{2.23}$$

where $H_\uparrow(\boldsymbol{k})$ and $H_\downarrow(\boldsymbol{k})$ are the Bloch Hamiltonians defined in the up- and down-spin space, respectively. We can calculate the Chern number for the Hamiltonian in each spin space. For the quantum spin Hall phase, the Chern numbers are non-trivial. Incidentally, the sum of the Chern numbers is vanished. In this case, the Chern numbers are the same to the entanglement Chern numbers for up- and down-spin, because the up-spins and the down-spins are decoupled. When the s_z conservation is broken, the entanglement Chern number still unchanged as far as the band gap of the entanglement Hamiltonian is open, because the entanglement Chern number is the topological number.

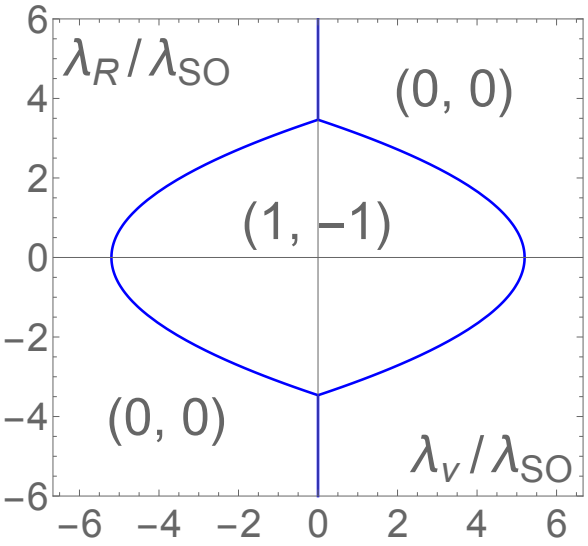

Figure 2.7: The phase diagram for the Kane-Mele model as function of λ_ν and λ_R for $\lambda_{SO} = 0.06$ and $t = 1$, which is determined by the entanglement Chern numbers $(c_\uparrow, c_\downarrow)$. $(c_\uparrow, c_\downarrow) = (0,0)$ and $(1,-1)$ are corresponding to the trivial insulator phase and the quantum spin Hall phase, respectively.

In next, we consider the entanglement Chern number for the Kane-Mele model. The Kane-Mele model had been introduced in Sec. 2.1.3. Figure 2.7 shows the phase diagram for the Kane-Mele model determined by the entanglement Chern numbers $(c_\uparrow, c_\downarrow)$. For small λ_ν and λ_R, the quantum spin Hall phase emerges, which is characterized by $(c_\uparrow, c_\downarrow) = (1, -1)$. Wheres, the trivial insulator phase is characterized by $(c_\uparrow, c_\downarrow) = (0, 0)$. The entanglement

Chern number changes on the blue lines in Fig. 2.7 where the band gap is closed at K and K' point in the Brillouin zone. We see the entanglement Chern number successfully reproduce the phase diagram of the Kane-Mele model by the $\mathbb{Z}_2$ index shown in Fig. 2.2. We note that the relation to the Chern number for block diagonalized Hamiltonian is hold only when $\lambda_R = 0$, although the topological classification by the entanglement Chern number is still valid in the global parameter space.

2.3.3 The entanglement Chern number for the topological insulator phase

Next, we contemplate the topological insulator phases. In three dimensions, we have arbitrary choice of axis in spin space to consider the entanglement Chern numbers. Here, let us choose the z-axis of the spin space for the entanglement Chern number. For three-dimensional systems, one can define the Chern number for the two-dimensional periodic plane in the three-dimensional Brillouin zone, by fixing one of the component of the reciprocal vector. Hereafter, we consider the (k_2, k_3) plane with fixed k_1. On this plane, the entanglement Chern number is defined in the same way to define it in two-dimensions. The entanglement Chern number is called the section entanglement Chern number.

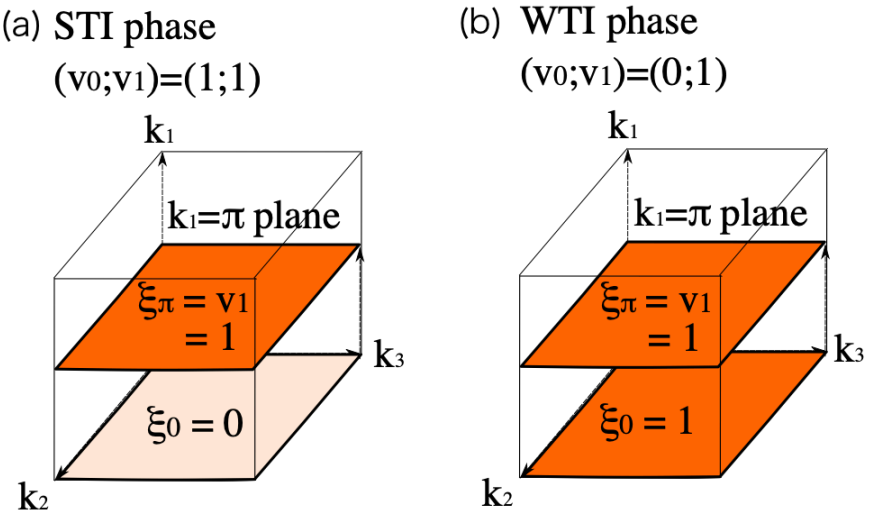

Figure 2.8: The schematic picture for the correspondence between the section entanglement Chern numbers and the $\mathbb{Z}_2$ indices, which is determined in the time-reversal invariant planes. Figure (a) shows the Brillouin zone for the strong topological insulators that have the non-trivial $\mathbb{Z}_2$ indices $\nu_0 = \nu_1 = 1$. For this case, the $\mathbb{Z}_2$ indices on the time-reversal invariant planes are different, corresponding the difference of the section entanglement Chern numbers. Figure (b) shows the Brillouin zone for the weak topological insulator phase that have $\nu_0 = 0$ and $\nu_1 = 1$. In this case, the $\mathbb{Z}_2$ indices on the time-reversal invariant planes are the same.

Remembering the $\mathbb{Z}_2$ indices for the topological insulator phases, the weak $\mathbb{Z}_2$ indices $\{\nu_j\}$ are defined on the time-reversal invariant planes, which is a plane in the Brillouin zone with fixed $k_j = \pi$. Whereas, the strong $\mathbb{Z}_2$ index corresponds the difference between the weak $\mathbb{Z}_2$ indices in the time-reversal invariant planes. Based on that, we firstly consider the strong topological insulator phase. In this phase, definitely the strong $\mathbb{Z}_2$ index is non-trivial and the weak $\mathbb{Z}_2$ indices for $k_1 = 0$ and $k_1 = \pi$ are different [see Fig. 2.8 (a)]. Figure 2.8 (a) shows an example, where the orange (ivory) color corresponds the non-trivial (trivial) weak $\mathbb{Z}_2$ index. To remember the correspondence between the entanglement Chern number and the $\mathbb{Z}_2$ index in the two-dimensional systems, which is demonstrated in the quantum spin Hall phase, there should be same kind of correspondence in three dimensions. That is, the

non-trivial (trivial) weak $\mathbb{Z}_2$ indices defined in the time-reversal invariant plane corresponds the non-trivial (trivial) section entanglement Chern number in the same plane. This implies the section entanglement Chern numbers interpolate the weak $\mathbb{Z}_2$ indices. For the strong topological insulator phase of Fig. 2.8 (a), the section entanglement Chern numbers are 1 for $k_1 = \pi$ and 0 for $k_1 = 0$, corresponding the weak $\mathbb{Z}_2$ indices. On the other hand, for the weak topological insulator with $\nu_0 = 0$ and $\nu_1 = 1$ [see Fig. 2.8 (b)], the weak $\mathbb{Z}_2$ indices are 1 for both $k_1 = \pi$ and $k_1 = 0$ planes. Corresponding them, the section entanglement Chern numbers with $k_1 = \pi$ and $k_1 = 0$ are also 1.

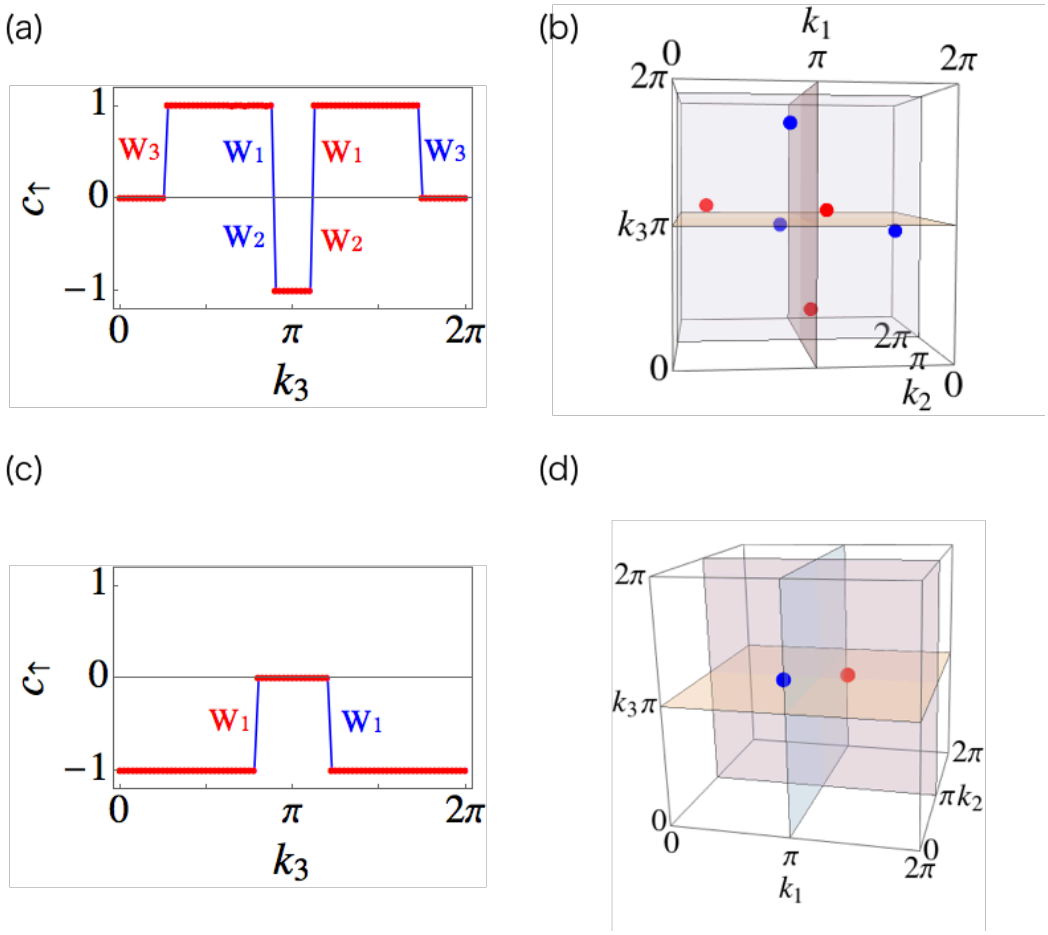

Figure 2.9: The section entanglement Chern numbers and the Weyl points of the entanglement Hamiltonian $H_\uparrow(\boldsymbol{k})$ for (a)-(b) $(t_1, t_2, t_3, t_4) = (1.15t, t, t, t)$ and (c)-(d) $(t_1, t_2, t_3, t_4) = (t, 1.15t, t, t)$. Figures (a) and (c) show the section entanglement Chern numbers. Figures (b) and (d) show the Weyl points of the entanglement Hamiltonians. The red (blue) color shows the chirality + (−) of the Weyl point.

These correspondence indicates that the section entanglement Chern number changes between $k_1 = 0$ and $k_1 = \pi$ planes for the strong topological insulator phase, whereas it does not change or changes even times for the weak topological insulator phase. The change of the topological invariant suggests the existence of a gapless point. As consequence, for the strong topological insulators, there are odd number of the Weyl point(s), which is the gapless point in the entanglement Hamiltonian. The Weyl point is considered as a topological charge, which is characterized by the monopole or anti-monopole of the Berry curvature. The Weyl points appear as pair of the monopole and anti-monopole because total monopole charge is zero. The chirality of the Weyl points are defines as + for the monopole and − for the

anti-monopole, respectively. Hence, total chirality of the Weyl points in the whole Brillouin zone is zero. Whereas, for the weak topological insulators, there are odd number of the Weyl point(s) in the entanglement Hamiltonian.

Then, we contemplate the section entanglement Chern numbers for the Fu-Kane-Mele model. The Fu-Kane-Mele model had been introduced in Sec. 2.2.2. Hereafter, we consider the entanglement Hamiltonian for up-spins, $H_{\uparrow}(\boldsymbol{k})$. Figure 2.9 shows the section entanglement Chern numbers with fixed k_3 and the Weyl points for two different topological insulator phases. In (a) and (b), the hopping parameters of the model is set to $(t_1, t_2, t_3, t_4) = (1.15t, t, t, t)$. The corresponding phase is $\nu_0; (\nu_1, \nu_2, \nu_3) = 1; (1, 1, 1)$. Figure (a) shows the section entanglement Chern number with fixed k_1. We can see there are totally six changes of the section entanglement Chern numbers. Figure (b) shows the Weyl points in the Brillouin zone. Corresponding with the changes of the section entanglement Chern numbers, there are six Weyl points, which is the gapless point in the entanglement Hamiltonian. Here we note that there are two Weyl points in the same plane, hence the section entanglement Chern number spontaneously changes by two. The Weyl points has the chirality + (−), which is colored in red (blue) in Fig. 2.9. On the other hand, in (c) and (d), the hopping parameters of the model is set to $(t_1, t_2, t_3, t_4) = (t, 1.15t, t, t)$. The corresponding phase is $\nu_0; (\nu_1, \nu_2, \nu_3) = 1; (1, 0, 0)$. Figure (c) shows the section entanglement Chern number and Fig. (d) shows the Weyl points for this system. We can see there are two changes of the section entanglement Chern numbers. Corresponding with it, there are two Weyl points. Here we have seen the two phases, the difference of the phases appear in the section entanglement Chern numbers. In (a), the entanglement Chern number with $k_1 = 0$ is trivial, wheres it is non-trivial with $k_1 = \pi$. This agrees the $\mathbb{Z}_2$ indices $(\nu_0, \nu_3) = (1, 1)$. We can see in Fig. (c) that the entanglement Chern number with $k_1 = 0$ ($k_1 = \pi$) is non-trivial (trivial). This also agrees the $\mathbb{Z}_2$ indices $(\nu_0, \nu_3) = (1, 0)$. These results clearly shows the correspondence between the section entanglement Chern numbers and the $\mathbb{Z}_2$ indices. Although we only show the section entanglement Chern numbers with fixed k_3, same correspondence for the section entanglement Chern numbers holds for other axes.

Chapter 3

Higher-order topological insulators

The "higher-order" topological boundary states, which is localized at the boundary of the boundary, is found in 2017 [46]. The bulk-boundary correspondence is also found for the higher-order topological insulators (HOTIs) on the hyper-cubic lattices [53–55]. One of the typical models is the HOTI model on a hyper-cubic lattice, so called *Benalcazar-Bernevig-Hughes (BBH) model* [47–49], which has alternating hopping strength and the π-flux in a plaquette. In this model, the π-flux opens the band gap and the topological corner states exists in the band gap. Another typical model is the HOTI model in a hyper-tetrahedral lattice, which include the kagome and the Pyrochlore lattice [50, 52]. The model also has the alternating hopping strength and the energy gap is opening without the flux. There are the topological corner states in the energy gap. We note that the models are equivalent to the molecular orbital models on the hyper-tetrahedral lattice [91] by the energy shift. The exactly solvable hinge and corner states for several HOTI models, including the breathing kagome HOTI model, are found [51, 56].

In this chapter, we introduce the higher-order topological insulator (HOTI) models on the hyper-cubic lattices [Sec. 3.1] and the hyper-tetrahedral lattices [Sec. 3.2], which have the 0-dimensional corner states. We also introduce the topological invariants for these models. In Sec. 3.3, we briefly review the previous experimental realizations of the HOTIs.

3.1 Higher-order topological insulator on hyper-cubic lattices

In this section, we introduce the typical models of the HOTIs, the BBH models, which is defined on the hyper-cubic lattices [47–49]. The models have the HOTI phase where the topological corner states appears. First, we introduce the models in two- and three-dimensions. Then, we review the topological invariant for the models.

3.1.1 Tight-binding models for the higher-order topological insulators on hyper-cubic lattices

In first, we introduce the BBH model, which is defined as a square lattice model. The model is a tight-binding model of single-orbital electrons with the nearest-neighbour hopping on a square lattice with the π-flux in a plaquette. The Hamiltonian is written as

$$\mathcal{H} = -\sum_{<i,j>} t_{ij} c_i^\dagger c_j. \tag{3.1}$$

Here, c_i and $c_i^\dagger$ are the annihilation and creation operators for an electron on i-th site, respectively. The model has alternating hopping parameters t_1 and t_2 between the nearest-

neighbour sites, as shown in Fig. 3.1 (a). In this figure, the amplitude of the hopping is t_1 (t_2) on the red (blue) lines. To induce the π-flux, one of the nearest-neighbour hopping in every plaquettes has the minus sign. The π-flux open the band gap on the zero-energy. Hereafter, we consider that the electrons are half-filled.

The Bloch Hamiltonian of the BBH model is calculated as

$$\begin{aligned} H(\mathbf{k}) = &(t_1 + t_2 \cos(k_x))\,\Gamma_4 + t_2 \sin(k_x)\,\Gamma_3 \\ &+ (t_1 + t_2 \cos(k_y))\,\Gamma_2 + t_2 \sin(k_y)\,\Gamma_1. \end{aligned} \tag{3.2}$$

Here, $\Gamma_0 = \tau_3\sigma_0, \Gamma_4 = \tau_1\sigma_0, \Gamma_j = -\tau_2\sigma_j$ for $j = 1, 2, 3$ and τ, σ are Pauli matrices indicating four electrons in an unit cell. The bulk spectrum of the model with $t_1 = 0.7, 1.0$ and 1.3 are shown in Fig. 3.1 (b), (c) and (d), respectively. The t_2 is fixed to 1.0 for each figures. There are four bands but each of two band are degenerated. The model has finite gap between the second and the third band as long as $|t_1/t_2| \neq 1$.

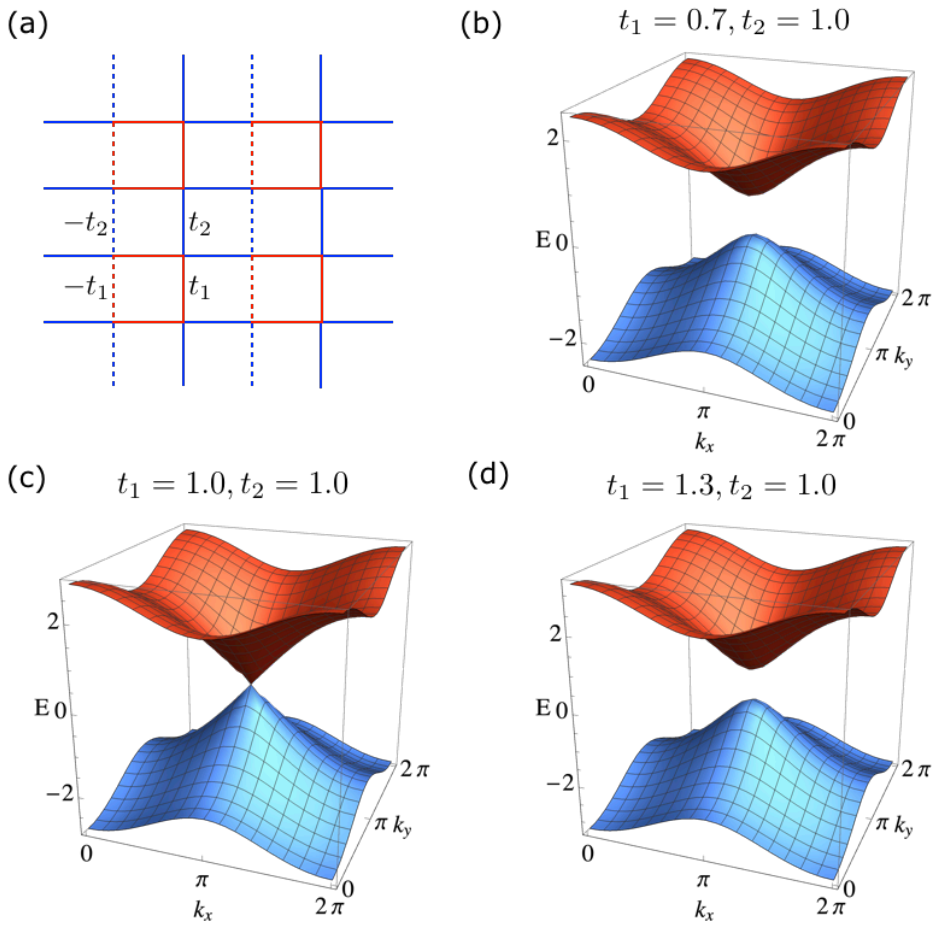

Figure 3.1: (a) The hopping parameters are shown. On the red (blue) lines, the amplitude of the hopping is t_1 (t_2). The hopping parameter on the dashed lines has minus sign. (b)-(d) The bulk spectrum of the BBH model with $t_1 = 0.7, 1.0$ and 1.3 are shown. The t_2 is fixed to 1.0.

Here we consider the model with open boundary condition that has 16×16 sites. Figure 3.2 (a) shows the eigen energies of the finite system against t_1/t_2. The figure shows that the energies of the corner states, which are colored in red, is in the energy gap. There are four corner states in the gap, which are localized in four corners. The total density plot of the

corner states is shown in Fig. 3.2 (b). The red circles represent the amplitude of the corner states on these sites.

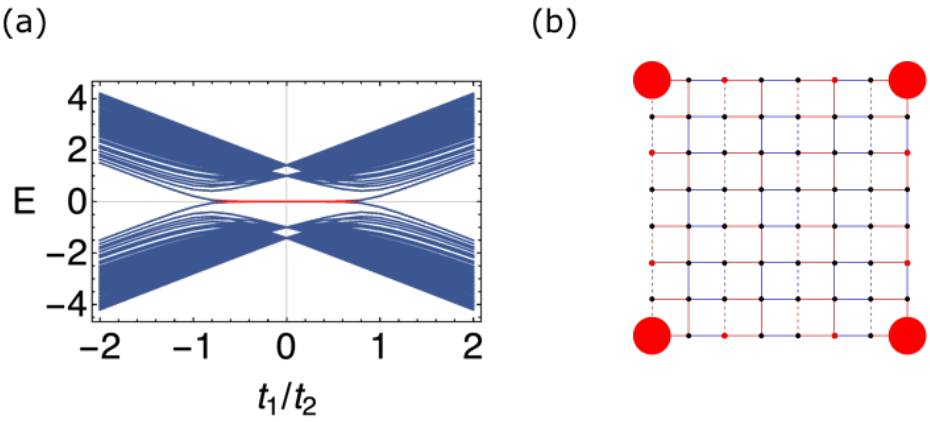

Figure 3.2: (a) The energies of the BBH model are shown against t_1/t_2. The system size is 16×16. There are the corner states in the energy gap, which is colored in red. (b) Total density plot of the corner states with $t_1/t_2 = 0.4$ are shown. The radius on a site corresponds the amplitude of the corner state on the site.

In next, we introduce the BBH model in three-dimensions. The model is a tight-binding model of single-orbital electrons with the nearest-neighbour hopping on a cubic lattice with the π-flux in each surface of the unit cells. Similar to the two-dimensional BBH model, the model Hamiltonian is defined as $\mathcal{H} = -\sum_{<i,j>} t_{ij} c_i^\dagger c_j$, which has alternating hoppings t_1 and t_2 between the nearest-neighbour sites. In the three-dimensional model, three hoppings for bonds in a unit cell has minus sign to induce the π-flux [Fig. 3.3 (a)].

Here, we consider the energies of the model with finite sites. Figure 3.3 (b) shows the eigen energies for the finite system that has $8 \times 8 \times 8$ sites with periodic boundary condition is shown. The figure shows the gap of the bulk energy is opening as long as $|t_1/t_2| \neq 1$. On the other hand, the Fig. 3.3 (d) shows the the eigen energies for the finite system with open boundary condition. In contrast with the 3.3 (b), the in-gap states which is colored in red appear. One of the sample is shown in Fig.3.3 (c). The figure shows the total density of the eight corner states with $t_1/t_2 = 0.4$.

3.1.2 The topological invariants for the BBH models

The topological invariant for the BBH model is proposed by W. A. Benalcazar, *et al.* As shown [48], the quadrupole moment of the BBH model serves as a topological number, which is quantized to 0 or 1/2. The paper proved that the quadrupole moment q_{xy} of quantized by the mirror symmetries about x and y directions and the quadrupole moment can be calculated by the *nested Wilson loop* of the system. In this section, we introduce the topological number proposed in [48].

In first, we introduce the Wilson loop for the bulk Hamiltonian. Let us define $|u_{\boldsymbol{k}}^m\rangle$ as the eigen state of the bulk Hamiltonian $H(\boldsymbol{k})$. Here, we consider the electrons are half-filled and the bulk bands have finite gap. The Wilson loop in the x direction $W_{x,\mathbf{k}}$ is defined as

$$W_{x,\mathbf{k}} = F_{x,\mathbf{k}+N,\Delta k_x} \dots F_{x,\mathbf{k}+\Delta\mathbf{k}_x} F_{x,\mathbf{k}} \tag{3.3}$$

$$[F_{x,\mathbf{k}}]^{mn} = \langle u_{\mathbf{k}+\Delta kx}^m | u_{\mathbf{k}}^n \rangle \tag{3.4}$$

where $\Delta\mathbf{k_x} = (2\pi/N_x, 0)$, N_x is the number to divide the k_x in the Brillouin zone. Here, $m, n = 1, 2$ are spanned for half-filled Bloch states $|u_{\mathbf{k}}^j\rangle$ $(j = 1, 2)$. The Wilson loop in the y

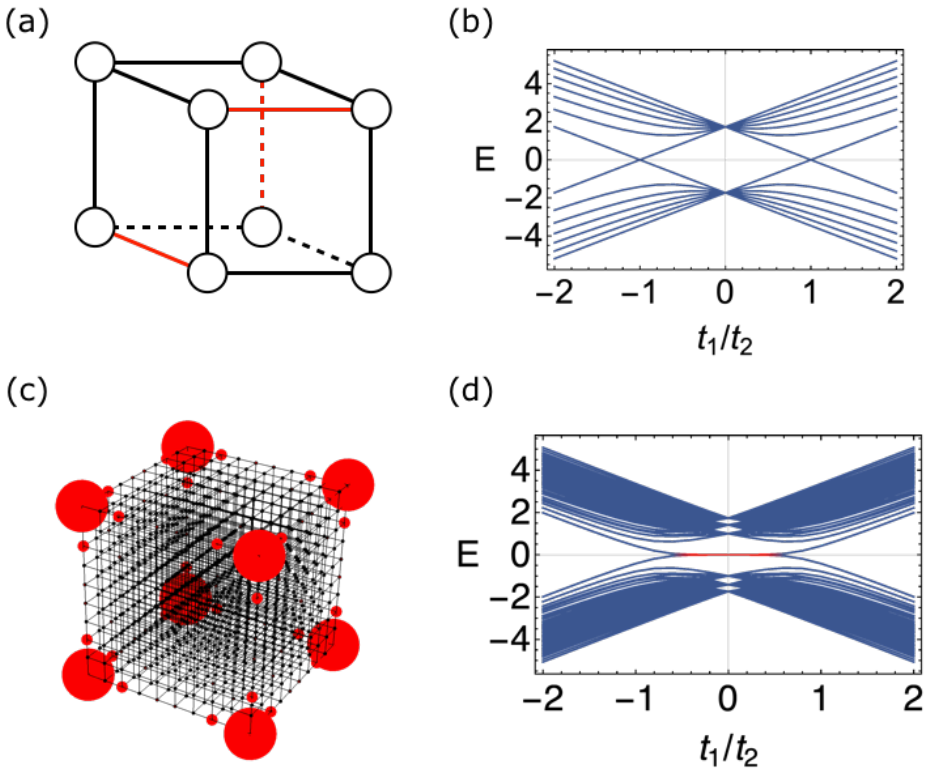

Figure 3.3: (a) A unit cell of the BBH model in three-dimensions is shown. The hopping parameters on the red line has minus sign. The amplitude of the hopping parameters in the unit cell is t_1. The amplitude of the hopping parameters connecting to the other unit cells is t_2. (b) The eigen energies of the 3D BBH model with the periodic boundary condition is shown. The systems size is $8 \times 8 \times 8$. (c) Total density of the corner states are shown. (d) The energies of the 3D BBH model are shown against t_1/t_2. There are the corner state in the energy gap, which is colored in red.

direction $W_{y,\mathbf{k}}$ is defined in similar way about the definition of the $W_{x,\mathbf{k}}$. Then, the Wannier Hamiltonian $H_{W_x(\mathbf{k})}$ is defined by

$$W_{x,\mathbf{k}} = e^{iH_{W_x(\mathbf{k})}}. \tag{3.5}$$

As shown in Ref. [92], the Wannier Hamiltonian is adiabatically connected to the edge Hamiltonian perpendicular to the x direction. Then, we can diagonalize the Wilson loop as

$$W_{x,\mathbf{k}} = \sum_{j=\pm} \left|v^j_{x,\mathbf{k}}\right\rangle e^{2\pi i v^j_x(k_y)} \left\langle v^j_{x,\mathbf{k}}\right|, \tag{3.6}$$

where $2\pi v^j_x(k_y)$ $(j = 1, 2)$ is the eigen value of the Wannier Hamiltonian and $\left|v^j_{x,\mathbf{k}}\right\rangle$ is the eigen vector of the Wilson loop. We note that the phases $v^j_x(k_y)$ are proportional to the Wannier centers [93–99]. The $v^j_y(k_x)$ and $\left|v^j_{y,\mathbf{k}}\right\rangle$ is also defined in the same fashion. Because of the mirror symmetry about x direction, the equation $v^-_x(k_y) = -v^+_x(k_y) \mod 1$ holds. Here, we redefined the $2\pi v^-_x(k_y)$ $(2\pi v^+_x(k_y))$ as the lower (higher) eigen value of the Wannier Hamiltonian. Hereafter, we restrict the phase $v^-_x(k_y)$ in $[0, 1/2]$. The schematic picture of the phases $v^\pm_x(k_y)$ is shown in Fig. **??**. In the present model, fortunately, the Wannier Hamiltonian is gapped for arbitrary $k_y \in (-\pi, \pi]$.

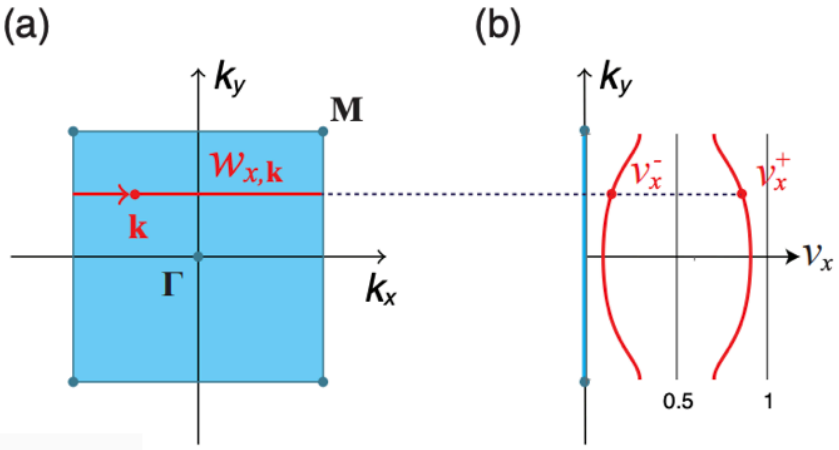

Figure 3.4: From Ref. [48]. (a) The Brillouin zone for the square lattice is shown. The Wilson loop $W_{x,\mathbf{k}}$ is calculated along the red line. (b) shows the eigen values of the Wannier Hamiltonian for $k_y \in (-\pi, \pi]$. The gap opens for any k_y.

Thus, we can calculate the *nested Wilson loop* in the following way. In the beginning, we define the Wannier band subspaces as

$$\left|w^{\pm}_{x,\mathbf{k}}\right\rangle = \sum_{n=1,2} |u^n_{\mathbf{k}}\rangle \left[v^{\pm}_{x,\mathbf{k}}\right]^n. \tag{3.7}$$

To define the nested Wilson loop for the Wannier band, we define

$$F^{\pm}_{y,\mathbf{k}} = \left\langle w^{\pm}_{x,\mathbf{k}+\Delta\mathbf{k}_y} | w^{\pm}_{x,\mathbf{k}} \right\rangle \tag{3.8}$$

for $\Delta \mathrm{k}_y = (0, 2\pi/N_y)$. Then, the nested Wilson loop for the Wannier band $v^{\pm}_x$ is defined as

$$\tilde{W}^{\pm}_{y,k_x} = F^{\pm}_{y,\mathbf{k}+N_y\Delta\mathbf{k}_y} \cdots F^{\pm}_{y,\mathbf{k}+\Delta\mathbf{k}_y} F^{\pm}_{y,\mathbf{k}}. \tag{3.9}$$

Then, the polarization of the Wannier band is

$$p_y^{v_x^{\pm}} = -\frac{i}{2\pi}\frac{1}{N_x}\sum_{k_x} \log\left[\tilde{W}^{\pm}_{y,k_x}\right] = \begin{cases} 1/2, & |t_1/t_2| < 1 \\ 0, & |t_1/t_2| > 1. \end{cases} \tag{3.10}$$

The polarization of the Wannier Hamiltonian $H_{W_x(\mathbf{k})}$ captures the topology of the edge Hamiltonian.

In next, we consider the polarization and the spacial symmetries. Firstly, we consider the mirror symmetries $M_x : x \to -x$, $M_y : y \to -y$ and the inversion symmetry $I : (x, y) \to (-x, -y)$. These symmetries enforce the polarization as

$$p_y^{v_x^+} \overset{M_x}{=} p_y^{v_x^-}, p_y^{v_x^{\pm}} \overset{M_y}{=} -p_y^{v_x^{\pm}}, p_y^{v_x^+} \overset{\mathcal{I}}{=} -p_y^{v_x^-} \bmod 1. \tag{3.11}$$

Therefore, the polarizations is quantized as

$$p_y^{v_x^{\pm}}, p_x^{v_y^{\pm}} = 0 \text{ or } 1/2 \tag{3.12}$$

with these symmetries. Thus, the Wannier bands with these three symmetries has the $\mathbb{Z}_2 \times \mathbb{Z}_2$ classification. In this classification, the non-trivial phase corresponds $\left(p_y^{v_x^{\pm}}, p_x^{v_y^{\pm}}\right) =$

$(1/2, 1/2)$. The classification is reduced to $\mathbb{Z}_2$ if the C_4 symmetry is satisfied. In this case, the quadrupole moment q_{xy} can be the topological invariant as

$$q_{xy} = p_y^{v_x^+} = p_y^{v_x^-} = p_x^{v_y^+} = p_x^{v_y^-} = 0 \text{ or } 1/2. \tag{3.13}$$

Actually, considering the BBH model that has the C_4 symmetry, the non-trivial polarization $p_y^{v_x^\pm} = 1/2$ as calculated in Eq. 3.10 corresponds the existence of the edge state shown in Fig. 3.2 (b).

Concluding the review, the polarization calculated for the Bloch Hamiltonian is quantized by the mirror and inversion symmetries. In this section, we have seen the polarizations for the two-dimensional BBH model, which is 1/2 for $|t_1/t_2| < 1$ and 0 for $|t_1/t_2| > 1$. This agrees with the existence of the corner states in the higher-order topological insulator phase seen in Fig. 3.2. In the similar way, the polarization for the three-dimensional BBH model is quantized as long as the mirror and inversion symmetries are preserved. It has also correspondence with the higher-order topological insulator phase [Fig. 3.3(d)], where 1/2 for $|t_1/t_2| < 1$ and 0 for $|t_1/t_2| > 1$.

The Berry phase is also serve as the topological invariant for the higher-order topological insulator phase with the C_4 symmetry. The quantization of the Berry phase is shown in Chapter 4. The Berry phase of the BBH model and the bulk-corner correspondence is shown in Chapter 5.

3.2 Higher-order topological insulators on hyper-tetrahedral lattices

In this section, we introduce the HOTI model on the hyper-tetrahedral lattices introduced by M. Ezawa in 2018 [50]. The models have the HOTI phase where the topological corner states appears. First, we introduce the models in two- and three-dimensions. Then, we review the topological invariant for the models.

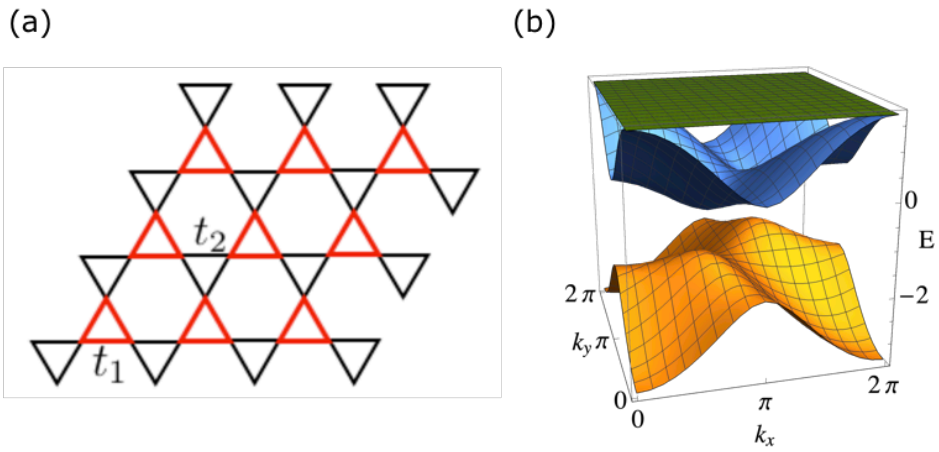

Figure 3.5: (a) The hopping parameters are shown. On the red (black) lines, the amplitude of the hopping parameter is t_1 (t_2). (b) shows the energies of the kagome HOTI model against t_1/t_2.

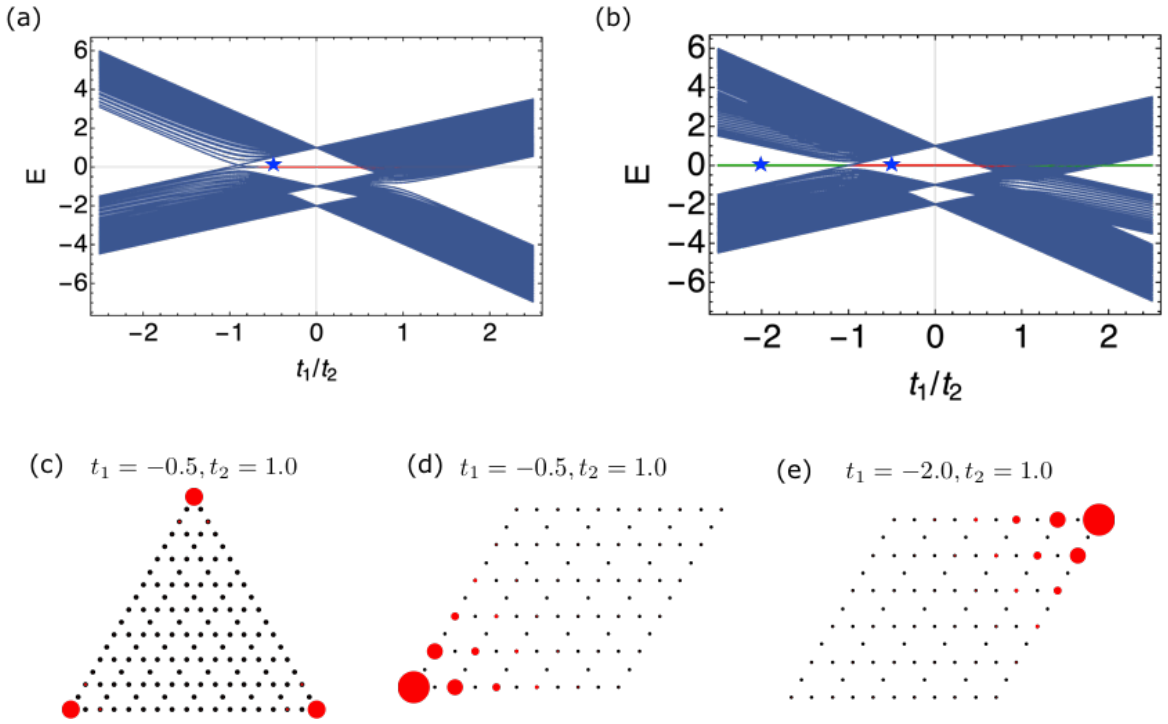

Figure 3.6: (a) The energies of the finite system of the breathing kagome model for a triangular geometry is shown. The red colored in-gap states show the corner states localized at three corners as shown in figure (c). The in-gap states are triply degenerated in the HOTI phase $-1 < t_1/t_2 < 0.5$. (c) The total-density of the in-gap corner states with $t_1 = -0.5$ and $t_2 = 1.0$ is shown. The radius on sites correspond the amplitude of the corner state on these sites. (b) The energies of the finite system of the breathing kagome model for a rhombic geometry is shown. The red (green) colored in-gap states show the corner states localized at the left-bottom (right-top) corner as shown in figure (d) ((e)). (d-e) The density of the in-gap corner state with $t_1 = -0.5$ ($t_1 = -2.0$) and $t_2 = 1.0$ is shown in figure (d) ((e)).

3.2.1 Tight-binding model for Higher-order topological insulators on hyper-tetrahedral lattices

Firstly, we consider a tight-binding Hamiltonian for spinless fermions on a breathing kagome lattice

$$\mathcal{H}_0 = -\sum_{i,j} t_{ij} c_i^\dagger c_j. \tag{3.14}$$

Here, $c_i^\dagger$ and c_i are the creation and annihilation operators of an electron on a site i, respectively, and $t_{ij} = t_1(t_2)$ if the bond between i and j belongs to the nearest-neighbor bond and it lives on the upward (downward) triangles (see Fig. 3.5(a)). In the following, we set $t_2 = 1$.

Here we consider the Bloch Hamiltonian of the breathing kagome model. The Bloch Hamiltonian for the three bands are calculated as

$$H(\boldsymbol{k}) = -\begin{bmatrix} 0 & h_1 & h_2 \\ h_1^* & 0 & h_3 \\ h_2^* & h_3^* & 0 \end{bmatrix}. \tag{3.15}$$

Here, the elements of the Hamiltonian are $h_1 = t_1 + t_2 e^{-i\left(k_x/2+\sqrt{3}k_y/2\right)}$, $h_2 = t_1 + t_2 e^{-ik_x}$ and $h_3 = t_1 + t_2 e^{i\left(-k_x/2+\sqrt{3}k_y/2\right)}$. The bulk spectrum obtained by diagonalizing the Hamiltonian

is shown in Fig. 3.5 (b) for the $t_1 = 0.7$ and $t_2 = 1.0$. There are a flat band and two dispersive bands. The latter bands are gapped for $|t_1/t_2| \neq 1.0$.

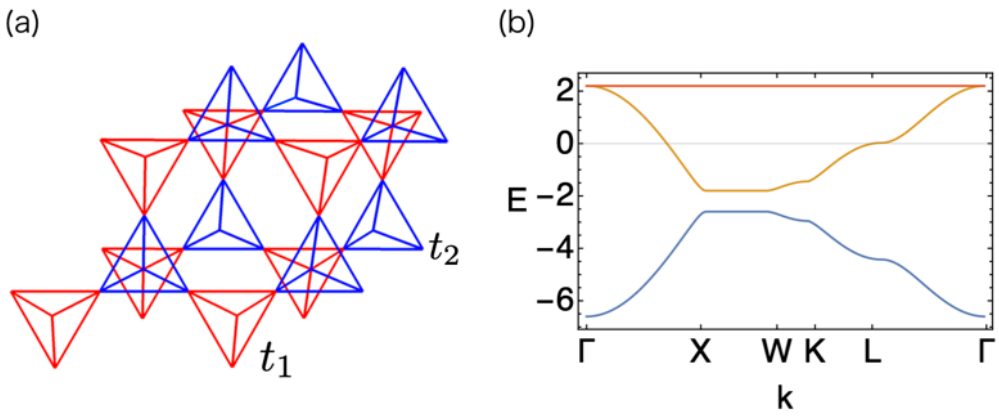

Figure 3.7: (a) The hopping parameters for the breathing Pyrochlore lattice model are shown. On the red (blue) lines, the amplitude of the hopping parameter is t_1 (t_2). (b) The bulk spectrum of the present model are shown as a function of t_1/t_2.

We then consider the energies for the finite system with open boundary conditions. Figure 3.6 (a) shows the eigen energies of the finite system for a triangular geometry as a function of t_1/t_2. The states in the energy gap is the localized states at corners. Figure 3.6 (c) shows the density plot of the corner states for $t_1 = -0.5$ and $t_2 = 1$, where the t_1-plaquette exists at the corners. The size of the points corresponds with the amplitude of the corner state on the site. As seen in the figure, the in-gap states are localized at the corners.

Next, we consider the rhombic geometry. Figure 3.6 (b) shows the eigen energies of the finite system for a rhombic geometry as a function of t_1/t_2. The states in the energy gap is the localized state at a corner. Figure 3.6 (d) and (e) show the density plot of the corner states for $t_1 = -0.5$ and $t_1 = -2.0$ with fixed $t_2 = 1$, respectively, where the t_1-plaquette exists at the left-bottom corner. The system size is 11×11 sites. As seen in the figure, the in-gap states are localized at the corners. In this geometry, the in-gap state with $|t_1/t_2| < 1$ (colored in red in Fig. 3.6 (c)) is localized in the left-bottom corner. On the other hand, the in-gap state with $|t_1/t_2| > 1$ (colored in green in Fig. 3.6 (c)) is localized in the right-top corner.

In next, we introduce a higher-order topological insulator model on a breathing Pyrochlore lattice, which is the extension of the breathing kagome model to three-dimensions. The model is a tight-binding model of single-orbital electrons with the nearest-neighbour hopping on a breathing Pyrochlore lattice, which is shown in Fig. 3.7 (a). Similar to the two-dimensional BBH model, the Hamiltonian is described as $\mathcal{H} = -\sum_{<i,j>} t_{ij} c_i^\dagger c_j$, where the nearest-neighbor hopping parameters take t_1 or t_2 [Fig. 3.7 (a)]. Figure 3.7 (b) shows the bulk spectrum of the model. The model has two flat bands and two dispersive bands. The gap of the latter two bands opens for $|t_1/t_2| \neq 1$.

Here, we consider the energies of the model with finite system sites. Figure 3.8 (a) shows the eigen energies for the finite system that has $6 \times 6 \times 6$ unit cells under the open boundary conditions. There are in-gap states, which is localized at corners. A sample of the corner state is shown in Fig. 3.8 (b). This is the corner state for $t_1 = 0.4$ and $t_2 = 1.0$. The in-gap state colored in green (red) shows the corner states localized at the right-top (left-bottom) corner shown in Fig. 3.8 (b).

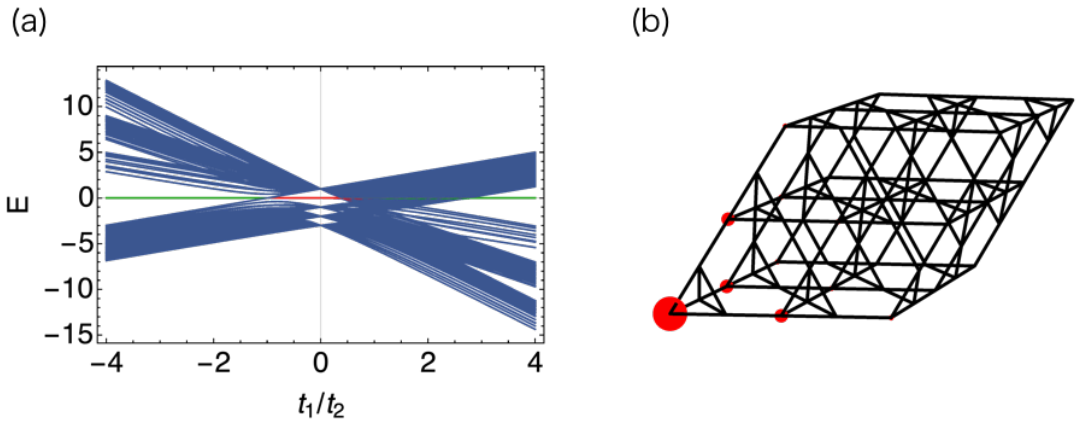

Figure 3.8: (a) The energies of the finite system of the breathing Pyrochlore model is shown. The red (green) colored in-gap states show the corner states localized at the left-bottom (right-top) corners in figure (b). (b) The in-gap corner state with $t_1 = 0.4$ and $t_2 = 1.0$ is shown. The radius on sites correspond the amplitude of the corner state on these sites.

3.2.2 The topological invariants for the hyper-tetrahedral HOTI models

The topological invariants for these systems are proposed by M. Ezawa [50]. He proposed a topological quantity corresponding with the Wannier center of the electrons. The topological quantity for two-dimensional kagome HOTI model is written as

$$P_3 = \frac{3}{2}\left(p_x^2 + p_y^2\right) = p_x^2 + p_+^2 + p_-^2, \tag{3.16}$$

for the polarizations $p_i = \frac{1}{S}\int_{\mathrm{BZ}} A_i d^2\mathbf{k}$ and $p_\pm = -p_x/2 \pm \sqrt{3}p_y/2$. The $A_i = -i\langle\psi|\partial_{k_i}|\psi\rangle$ is the Berry phase, and $S = 8\pi^2/\sqrt{3}$ is the area of the Brillouin zone. Firstly we consider the limitation of the value of polarizations. If we consider the gauge transformation as $|\psi\rangle \to e^{i\chi(\boldsymbol{k})}|\psi\rangle$. The transformation enforce $\frac{1}{2\pi}\oint A_x(\boldsymbol{k})dk_x \to \frac{1}{2\pi}\oint A_x(\boldsymbol{k})dk_x + \frac{1}{2\pi}\left(\chi(2\pi, k_y) - \chi(0, k_y)\right)$. We can take $\left(\chi(2\pi, k_y) - \chi(0, k_y)\right) = 2\pi n$ where n is an integer. Hence, $\frac{1}{2\pi}\oint A_x(\boldsymbol{k})dk_x$ is well-defined mod 1. As same, $\frac{1}{2\pi}\oint A_y(\boldsymbol{k})dk_y$ is also well-defined mode 1. As consequence, the polarizations p_j are well-defined mod 1. Hereafter, we take $p_j \in [0, 1)$.

The quantity is quantized under the three-fold rotational (C_3) symmetry, the mirror symmetries M_x with respect to the x axis and $M_\pm$ with respect to the two lined obtained by rotating the x axis by $\pm 2\pi/3$. The quantization of the quantity is shown as follows. Firstly, under the mirror symmetry M_x, p_x obeys $p_x = -p_x$. Hence the p_x is quantized as 0 or 1/2. In the similar way, we can show that $p_\pm$ are quantized as 0 or 1/2 by using $M_\pm$. In the trivial phase, the quantity is 0, which means the Wannier center is at the origin in the unit cell as shown in Fig. 3.9 (b). On the other hand, in the HOTI phase, the quantity is 1/2, which means the Wannier center is at the center of the unit cell as shown in Fig. 3.9 (a).

Similar to the kagome HOTI model, the topological quantity for the Pyrochlore HOTI model is defined as

$$\begin{aligned} P_6 &= p_{x+y}^2 + p_{y+z}^2 + p_{z+x}^2 + p_{x-y}^2 + p_{y-z}^2 + p_{z-x}^2 \\ &= 4\left(p_x^2 + p_y^2 + p_z^2\right). \end{aligned} \tag{3.17}$$

As same as the derivation of the quantization of the P_3 in two-dimensions, quantization of the P_6 is shown under the mirror symmetries for each plane. As a consequence, the quantity

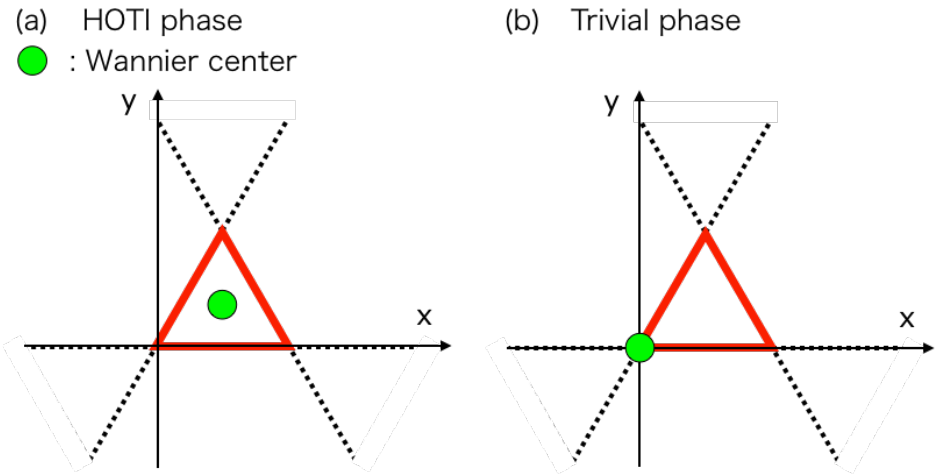

Figure 3.9: The figure shows the Wannier center of the electrons on the kagome lattice for (a) the HOTI phase and (b) the trivial phase.

is quantized to $P_6 = 0$ or 3. In this model, the non-trivial $P_3 = 3$ corresponds the HOTI phase of the model with $-1 < t_1/t_2 < 1/2$.

As shown in [91], the quantized Berry phase is also the topological invariant for the systems. The Berry phase is quantized by the symmetric group S_Q, where $Q = d + 1$ and d is dimension of the system. The S_Q symmetries are equivalent to the mirror symmetry for one-dimensional systems, the C_3 symmetry for two-dimensional systems and a combination of the mirror and C_3 symmetries for three-dimensional systems. Then the Berry phase is quantized to be $2\pi\frac{n}{Q}$. The quantization of the Berry phase is described in the next chapter.

3.3 Experimental realizations

Recently, the higher-order topological materials are experimentally found one after another. Firstly, the second-order topological insulator is realized in a bismuth crystal [57]. In this material, the topological hinge states protected by the C_3 symmetry appear. They calculated the eigenstates of the system by both the tight-binding model and the first-principle calculations. Also they observed the hinge states of the system by the STM experiment.

The higher-order topology is also observed in classical systems. A phononic quadrupole topological insulator is observed in a two-dimensional mechanical system [58]. The system consists of silicon plates and they measured the resonance frequencies for the finite system. They observed the corner modes corresponding with the second-order quadrupole topological insulator phase. Electrical circuits are also the playground of the higher-order topology [59, 60]. In this case, the impedance between two nearest-neighbour sites at the corner is intense in the higher-order topological phase. The second-order topological insulator is found in a photonic crystal [61, 62]. The system is in a square lattice with a breathing structure. They consider the transverse-magnetic (TM) field of light and predict the classification of the topological phases of the system [61]. After that, the corner mode for the topological phases are observed [62]. These kind of topological boundary state are observed in various one-dimensional photonic crystals [100, 101]. However these are one-dimensional systems, they have similar topological origin to the higher-order topological insulators. Actually, both of them are characterized by the Zak phase, which is quantized under the inversion symmetry. The higher-order topology is also found in the acoustic system [63]. They fabricated a breathing kagome structure of the cylindrical resonators. They measured the frequency and

found the corner modes corresponding with the higher-order topology.

We have briefly reviewed the experiments for higher-order topological insulators, which are mostly in two-dimensions. Because the impurities break the spatial symmetry, it is a basic problem whether the higher-order topological insulators are robust against disorders. In Chapter 6, we investigate the disorder effect for the higher-order topological insulators by using artificial neural networks.

Chapter 4

Berry phase and its quantization

This chapter introduce the Berry phase as a topological invariant with symmetries. Firstly we show the definition of the Berry phase and its quantization for both tight-binding models and spin models. In next, we briefly describe the symmetry and the quantization of the Berry phase.

4.1 Berry phase with local bond twist

This section introduce the definition of the Berry phase by introducing the local bond twist, originally defined by Y. Hatsugai and I. Maruyama [91].

4.1.1 The Berry phase for tight-binding models

Hereafter, we deal with the tight-binding model of single orbital spinless electrons with the unit cell of N sites and the Hamiltonians $\mathcal{H}$ are invariant under the symmetric group $\mathbb{Z}_N$, which changes the index of the sites $j \to j+1$ $(N+1=1)$. Hereafter, we consider the finite system under periodic boundary conditions. The local bond twistings are introduced as follows. To begin with, we write $\mathcal{H}$ as

$$\mathcal{H} = h_{P_0} + \sum_{P \neq P_0} h_P. \tag{4.1}$$

where h_P is the Hamiltonian that consists of hoppings and electron-electron interactions closed in a unit cell P. The P_0 is one of the unit cells. We then modify h_{P_0} in such a way that

$$\mathcal{H}(\boldsymbol{\theta}) := h_{P_0}(\boldsymbol{\theta}) + \sum_{P \neq P_0} h_P. \tag{4.2}$$

where the creation and annihilation operators only in h_{P_0} is modified as $\tilde{c}_j := e^{i\varphi_j} c_j$ and $\tilde{c}_j^\dagger := e^{-i\varphi_j} c_j^\dagger$ with $\varphi_j = \sum_{q=1}^{j} \theta_q$ for $j = 1, 2, \cdots, N$ and $\varphi_N = 0$. The parameter space $\boldsymbol{\Theta}$ is defined by $N-2$ independent parameters $(\theta_1, \theta_2, \cdots, \theta_{N-1})$ and $\theta_N = -\sum_{j=1}^{N-1} \theta_j$. We note that the Hamiltonians defined in all the other unit cells are unchanged.

Now let us define the paths L_j $(j = 1, 2, \cdots, N)$ in the twist-parameter space, $\boldsymbol{E}_{j-1} \to \boldsymbol{G} \to \boldsymbol{E}_j$ where $\boldsymbol{E}_1 = (2\pi, 0, \cdots, 0)$, $\boldsymbol{E}_2 = (0, 2\pi, \cdots, 0)$, $\cdots$, $\boldsymbol{E}_{N-1} = (0, 0, \cdots, 2\pi)$, $\boldsymbol{E}_0 = \boldsymbol{E}_N = (0, 0, 0)$, and $\boldsymbol{G} = 1/N \sum_{j=1}^{N} \boldsymbol{E}_j$.

We define the Berry phase in the parameter space as an integral in the closed path for the Berry connection,

$$\boldsymbol{A}(\boldsymbol{\theta}) = \langle \Psi(\boldsymbol{\theta}) | \frac{\partial}{\partial \boldsymbol{\theta}} | \Psi(\boldsymbol{\theta}) \rangle \,, \tag{4.3}$$

along the path L_j,

$$\gamma_j = -i \oint_{L_j} d\boldsymbol{\Theta} \cdot \boldsymbol{A}(\boldsymbol{\Theta}) \tag{4.4}$$

where $|\Psi(\boldsymbol{\Theta})\rangle$ denotes the many body ground state of $\mathcal{H}(\boldsymbol{\Theta})$.

The Berry phases of the models are quantized in $\mathbb{Z}_N$ as the following reasons: Firstly, because the Berry phases for each of the paths are canceled, we have

$$\sum_{j=1}^{N} \gamma_j \equiv N\gamma \equiv 0 \mod 2\pi. \tag{4.5}$$

Secondly, the $\mathbb{Z}_N$ symmetry enforces

$$\gamma_1 \equiv \gamma_2 \equiv \cdots \equiv \gamma_N \equiv \gamma \mod 2\pi. \tag{4.6}$$

To combine the above two equations, we obtain $\gamma_j \equiv 2\pi \frac{n}{N} \mod 2\pi$, $n \in \mathbb{Z}$ for $j = 1, 2, \cdots, N$.

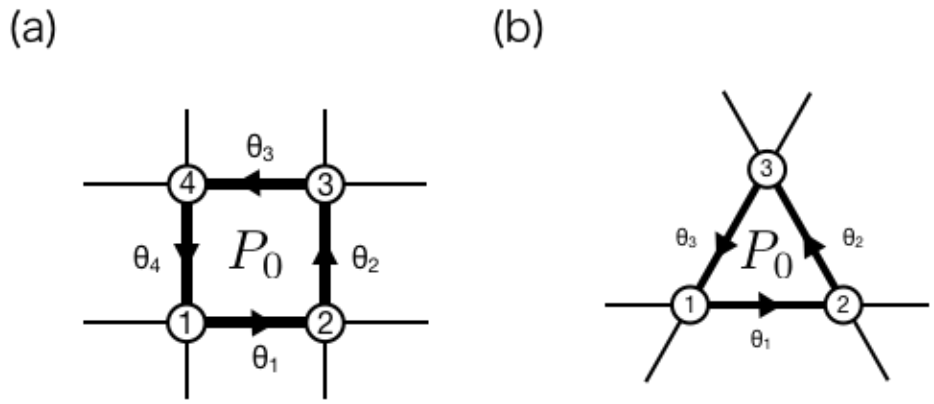

Figure 4.1: The twist parameters induced for the nearest-neighbour hopping on (a) a square lattice and (b) a kagome lattice are shown.

Here we show the example for the $N = 4$ case for a square lattice model and the $N = 3$ case for a kagome lattice model. Figure 4.1 shows the twist parameters for the nearest-neighbour hopping on (a) a square lattice and (b) a kagome lattice. In these models, the Berry phases are quantized in $\mathbb{Z}_4$ and $\mathbb{Z}_3$, respectively.

4.1.2 The Berry phase for spin models

This section introduce the Berry phase of spin models. Again, we consider a spin model with the unit cell of N sites and the Hamiltonians $\mathcal{H}$ are invariant with the symmetric group $\mathbb{Z}_N$, which changes the index of the sites $j \to j + 1$ $(N + 1 = 1)$. To introduce the twist for the interactions in a unit cell, we modify the Hamiltonian

$$\mathcal{H}(\boldsymbol{\Theta}) := h_{P_0}(\boldsymbol{\Theta}) + \sum_{P \neq P_0} h_P. \tag{4.7}$$

where $S_j^- \to e^{i\varphi_j} S_j^-$ and $S_j^+ \to e^{-i\varphi_j} S_j^+$, instead of $c_j \to e^{i\varphi_j} c_j$ and $c_j^\dagger \to e^{-i\varphi_j} c_j^\dagger$ for the tight-binding model. The definition of φ_j is same to that for the tight-binding model.

As same as the derivation in the previous section, we conclude the Berry phase for the spin model is quantized as

$$\sum_{j=1}^{N} \gamma_j \equiv N\gamma \equiv 0 \mod 2\pi. \tag{4.8}$$

4.2 Symmetries and quantization of the Berry phase

This kind of the Berry phase with the local bond twist is firstly introduced for the spin liquid models [35]. The Berry phase is quantized under some anti-unitary operation, including the time-reversal symmetry [36, 38]. The Berry phase is quantized for the spin chains with inversion symmetry [37, 40, 44]. The quantization is extended to the system with the SU(N) symmetry [41] and the rotational symmetry [43]. Here, we mention that the calculation method for the quantized Berry phase is developed by using path-integral Monte Carlo simulations [39, 42].

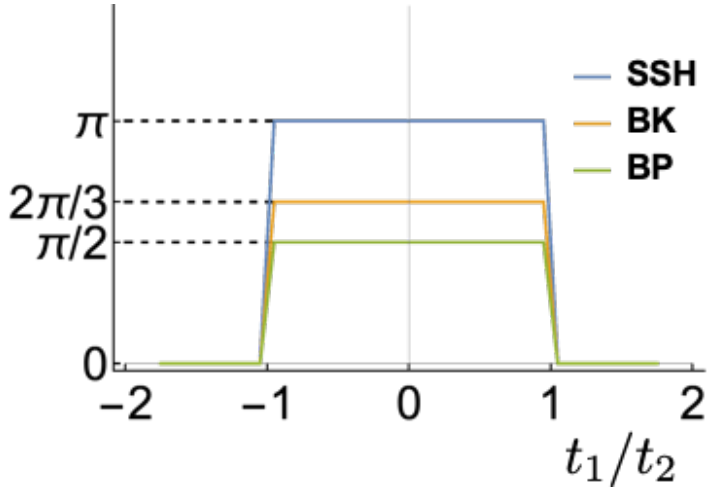

Figure 4.2: The Berry phase for the SSH model, the breathing kagome (BK) model and the breathing Pyrochlore (BP) model is shown. The Berry phases are quantized in $2\pi/2 = \pi$, $2\pi/3$ and $2\pi/4 = \pi/2$ for the SSH model, the BK model and the BP model, respectively.

Now we return to the model with the $\mathbb{Z}_N$ symmetry shown in the previous section. One of the typical models of the symmetry is the breathing hyper-tetrahedral models as $\gamma = 2\pi/(d+1)$ where d is the spacial dimension [91]. In Ref. [91], they deal with the molecular orbital models, but they are equivalent to the breathing tetrahedral models we introduced in Chapter 3 by just the energy shift. Hence, the models include the Su-Schrieffer-Heeger (SSH) model, the breathing kagome model and the breathing Pyrochlore model. They have quantized Berry phases as shown in Fig. 4.2. As seen in previous chapter, they have the corner states corresponding with the HOTI phases. For the series of the models, the $\mathbb{Z}_N$ symmetry is equivalent to the inversion symmetry, the three-fold rotational (C_3) symmetry and the mirror plus C_3 symmetry for the SSH model, the breathing kagome model and the breathing Pyrochlore model, respectively.

Further, the Berry phase is quantized in $\mathbb{Z}_4$ for the BBH model on the hyper-cubic lattices. The details for the quantization and the relation to the higher-order topology is described in the next chapter.

Chapter 5

Quantized Berry phases for higher-order topological insulators

In this chapter, the Berry phase for the Hamiltonian with the local twists is proposed to characterize the HOTI phases and the higher-order symmetry protected topological (HOSPT) phases. For the the SPT phases, the quantized Berry phase has been used to characterize them including both the many-body and the non-interacting systems [35–44]. In this study, we extend the characterization of the SPT phases to the HOSPT phases. The main observation of the study is that non-trivial Berry phases illustrate the ground state of the system is adiabatically connected with the *irreducible (decoupled) cluster state*. The irreducible cluster states are not divided in the smaller clusters or elements under the symmetries that protect the topological insulator phases. This chapter demonstrates the ground state of the HOTI/HOSPT can be adiabatically connected to the irreducible cluster states. We also demonstrate the boundary states of the HOTIs are obtained by cutting the clusters on higher-order boundaries. Similar to the first-order SPT phases, the quantized Berry phase is a topological invariant to characterize the HOSPT phases.

5.1 Quantized Berry phases

The quantized Berry phase has been defined in the previous chapter. In this section, we consider the Berry phase for the BBH model. Then, we show the bulk-corner correspondence for the HOTI phases in which the ground state is adiabatically connected to the decoupled-clusters.

5.1.1 Quantized Berry phases for the BBH model

Here we define the BBH model, which is mainly studied exampled in this chapter. The BBH model is written as

$$\mathcal{H}_{\mathrm{BBH}} = -\sum_{\langle kl \rangle} t_{kl} e^{i\alpha_{k,l}} \hat{c}_k^\dagger \hat{c}_l, \tag{5.1}$$

where $t_{kl} = t_2$ (t_1) for the nearest-neighbour hopping are alternated bonds, which is colored in blue (red) in Fig. 5.1(a). The model has the π-flux in every square plaquettes, which is implemented in the phase factor $e^{i\alpha_{k,l}}$. The π-flux is essential to open the energy gap in bulk [53,54]. For the explicit representation for the C_4 symmetry of the model, the phase $\alpha_{k,l}$ is set to be $\pi/4$ for the nearest-neighbour hoppings (see Fig. 5.1(a)). We emphasize that the model defined above is equivalent under the gauge transformation to the model introduced in Chapter 3, which is originally proposed in Ref. [48]. For the later discussions, we introduce three types of the square plaquettes: type-I where all the amplitude of the hopping belong to

the plaquette are t_1, type-II where all the amplitude of the hopping belong to the plaquette are t_2, and type-III where two of four amplitude of hoppings are t_1 and the rest two are t_2.

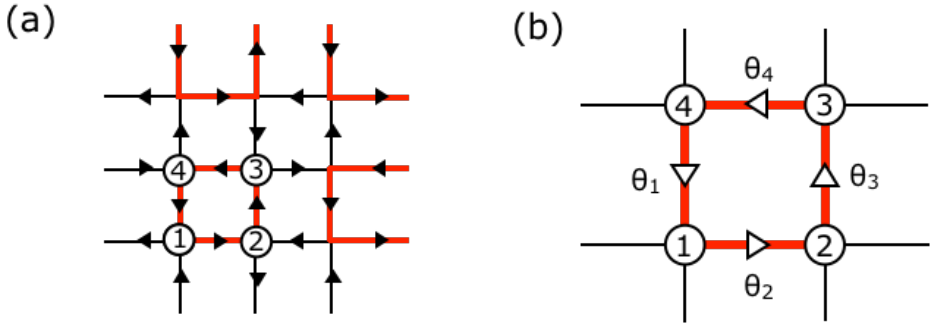

Figure 5.1: (a) This figure shows the hopping parameters in a square lattice. The red and black colors on the nearest-neighbour bonds correspond the amplitude of the hopping t_1 and t_2, respectively. Along the arrows, the phases factors of the hopping parameters on the bonds are set to $e^{-i\pi/4}$. (b) The twist parameters of the Berry phase are shown. The parameters induce the twists on the nearest-neighbour bonds along the arrows.

Now the Berry phase of the BBH model is introduced, which is quantized due to the C_4 symmetry. In the beginning, we rewrite the non-interacting Hamiltonian $\mathcal{H}_0$ as

$$\mathcal{H}_0 = \sum_{\eta=I,II} \sum_{P\in\text{type}-\eta} h_P \tag{5.2}$$

by using the Hamiltonian h_P for the plaquette P. Then, we specify a plaquette P_0, which is chosen to reside in either the type-I plaquette or the type-II plaquette. In next, we change the Hamiltonian h_{P_0} such that $\hat{c}_k \to e^{i\varphi_k}\hat{c}_k$ with $\varphi_k = \sum_{n=1}^{k}\theta_n$ for $k = 1, 2, 3, 4$ and $\varphi_4 = 0$. The fourth parameter θ_4 is fixed by the condition to be $-\sum_{n=1}^{3}\theta_n$. Hence, there are three independent parameters, θ_1, θ_2 and θ_3, which form the parameter space $\boldsymbol{\Theta} = (\theta_1, \theta_2, \theta_3)$. The total Hamiltonian modified by the twist parameters is written as

$$\mathcal{H}(\boldsymbol{\theta}) = h_{P_0}(\boldsymbol{\theta}) + \sum_{P\neq P_0} h_P, \tag{5.3}$$

where $\boldsymbol{\theta} \in \boldsymbol{\Theta}$. The paths in the parameter space L_n $(n = 1, 2, 3, 4)$ are defined as $\boldsymbol{E}_{n-1} \to \boldsymbol{G} \to \boldsymbol{E}_n$ where the points in the parameter space $\boldsymbol{E}_n$ are $\boldsymbol{E}_1 = (2\pi, 0, 0)$, $\boldsymbol{E}_2 = (0, 2\pi, 0)$, $\boldsymbol{E}_3 = (0, 0, 2\pi)$, $\boldsymbol{E}_0 = (0, 0, 0)$, $\boldsymbol{E}_4 = \boldsymbol{E}_0$ and the center of the points is $\boldsymbol{G} = 1/4\sum_{n=1}^{4}\boldsymbol{E}_n$. The Berry phase is defined in the parameter space as an integral on the closed path L_n for the Berry connection $\boldsymbol{A}(\boldsymbol{\theta}) = \langle\Psi(\boldsymbol{\theta})|\frac{\partial}{\partial\boldsymbol{\theta}}|\Psi(\boldsymbol{\theta})\rangle$,

$$\gamma_n^\eta = -i\oint_{L_n} d\boldsymbol{\theta}\cdot\boldsymbol{A}(\boldsymbol{\theta}) \tag{5.4}$$

where $\boldsymbol{\theta}$ runs on the path L_n and $|\Psi(\boldsymbol{\theta})\rangle$ is the ground state of the modified Hamiltonian $\mathcal{H}(\boldsymbol{\theta})$. In the case for the non-interacting systems, $|\Psi(\boldsymbol{\theta})\rangle$ is calculated by occupying the all of single-particle states which have the negative energy.

In the following, we consider the reason for the quantization of the Berry phase in $\mathbb{Z}_4$. In the first, as seen in Fig. 5.2 (b), we can see the Berry phases on each of paths $\{L_n\}$ are canceled. Therefore, we have the equation

$$\sum_{n=1}^{4}\gamma_n^\eta = 4\gamma = 0 \ mod\ 2\pi. \tag{5.5}$$

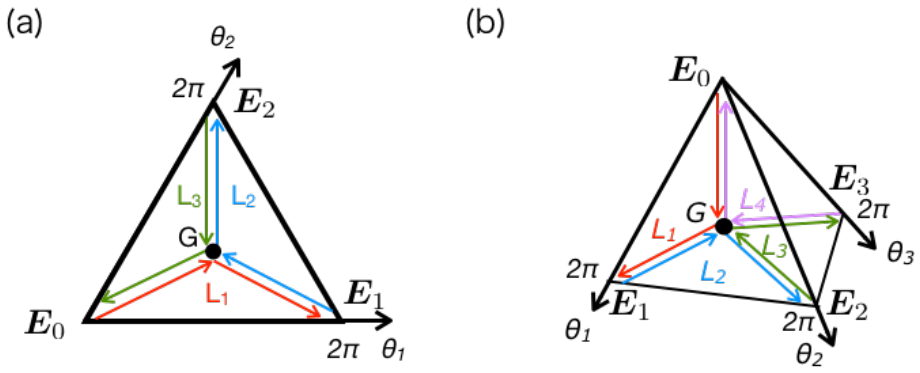

Figure 5.2: Figure (a) and (b) shows the paths of the Z_N Berry phase for the case of $N = 3$ and $N = 4$ in the parameter space, respectively.

In the second, because of the C_4 symmetry of the BBH model, we obtain

$$\gamma_1^\eta = \gamma_2^\eta = \gamma_3^\eta = \gamma_4^\eta \equiv \gamma^\eta \ mod\ 2\pi. \tag{5.6}$$

To use above two equations, we have $\gamma_n^\eta = \gamma^\eta = 2\pi\frac{m}{4}\ mod\ 2\pi$ where m is an integer. Hence we can conclude the Berry phase is quantized in $\mathbb{Z}_4$.

5.1.2 Bulk-corner correspondence

In this section, we describe the bulk-corner correspondence, which is a relation between the corner states of the HOTIs and the (bulk) Berry phase. For the sake to show the bulk-corner correspondence, we consider the $\mathbb{Z}_N$ Berry phase for the HOTIs in the decoupled cluster limit. For the BBH model, the clusters are shown in Fig. 5.3. In the decoupled limit, which means t_1 or t_2 is 0, the Berry phase for the whole system is equivalent to the Berry phase for one of the clusters. Hence, we need to deal with the Berry phase for single cluster in the limit. Hereafter, we consider that the cluster consists of N sites, *c.f.* $N = 4$ for the BBH model and $N = 3$ for the breathing kagome model. The Hamiltonian has $\mathbb{Z}_N$ symmetry that require the Hamiltonian is invariant with the cyclic operations $\hat{c}_k \to \hat{c}_{k+1}$, $\hat{c}_{N+1} = \hat{c}_1$ where $\hat{c}_k$ $(n = 1, \cdots, N)$ is the annihilation operators of the k-th electron in a unit cell. For that case, we calculate the Berry phase for the single cluster γ as

$$\gamma = 2\pi \langle n_1 \rangle = \cdots = 2\pi \langle n_N \rangle = 2\pi\nu \tag{5.7}$$

where $\langle n_k \rangle$ are occupation numbers of the electron at the k-th site and ν is the filling factor of the system. The detail of the derivation is shown in Appendix 5.4. For the BBH model with half-filling, the Berry phase for the single cluster takes $\gamma = 2\pi/2 = \pi$.

As the Berry phases of the decoupled clusters has been obtained, the boundary states for the finite system is simply inferred. Figure (5.3) is an illustration for the decoupled clusters of the BBH model with the cutting on boundaries. If one of the clusters with strong bonds is cut off at a corner, the corner state emerged from the localized state at the isolated site. In that case, under periodic boundary conditions, the Berry phase for the decouple clusters is non-trivial. In addition, as the Berry phase is the topological invariant, the Berry phase is unchanged as long as band gap remains open. In conclusion, the ground state, which is adiabatically connected to the decoupled cluster state has also non-trivial Berry phase. Following section demonstrates the bulk-corner correspondence for the several extensions of the BBH model.

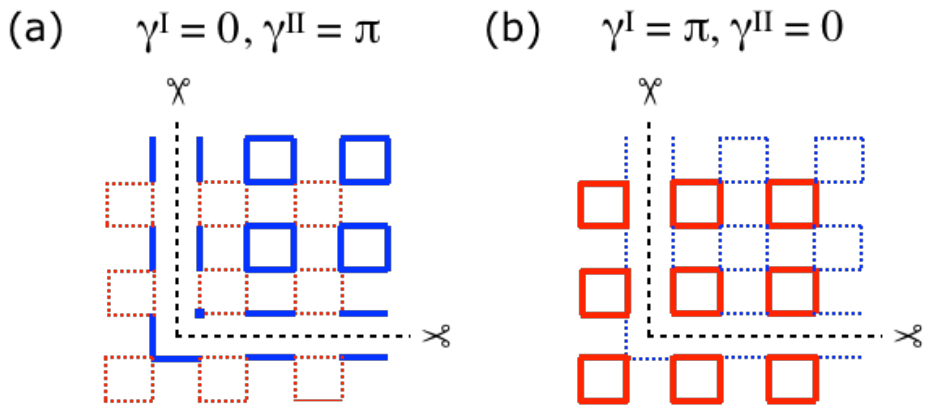

Figure 5.3: This figure shows a schematic picture about the bulk-corner correspondence, which is a relation between the corner state and the Berry phase. The type-I (type-II) plaquettes are colored in red (blue). Thick and dashed lines corresponds to the strong and weak bonds, respectively. In (a), a plaquette is cut at a corner with strong bonds. On the other hand, in (b), a plaquette is cut at a corner with weak bonds.

5.2 Quantized Berry phases for Higher-order topological insulator models

In this section, we show that the Berry phase describes the HOTI phases of the extended BBH models. Firstly, we demonstrate the Berry phase characterize the HOTI phase of the BBH model with the next-nearest-neighbor (NNN) hoppings. Then, we extend the model to the many-body analogue for the BBH model with the inter-site repulsive interactions. Further, we analyze the quantum spin analog of the model. This is the platform of the HOSPT phases. For these systems, we confirmed the correspondence of the quantized Berry phase with corner excitations in finite systems. The correspondence clearly shows the characterization of the Berry phase for the HOTI phases beyond the non-interacting fermions. Finally, we discuss the application of the characterization we proposed to the three-dimensional (3D) BBH model.

5.2.1 The BBH model with next-nearest neighbour hopping

In this section, we analyze the BBH model with next-nearest neighbour (NNN) hopping and its Berry phases. In first, we introduce the NNN hopping term to the BBH model such that the extended model still has the zero-energy corner state.

Here, we define the BBH model with the NNN hopping term as $\mathcal{H}_0 = \mathcal{H}_{\mathrm{BBH}} + \mathcal{H}_{\mathrm{NNN}}$ where

$$\mathcal{H}_{\mathrm{NNN}} = -\lambda \sum_{\langle\langle kl \rangle\rangle} u_{kl} \hat{c}_k^\dagger \hat{c}_l. \tag{5.8}$$

The u_{kl} is determined according to whether the NNN bond is belong to the type-I plaquettes, the type-II plaquettes or the type-III plaquettes as shown in Fig. 5.4 (a). Namely, $u_{kl} = t_1, t_2$, and $(t_1 + t_2)/2$ for the bonds for the type-I plaquettes, the type-II plaquettes or the type-III plaquettes, respectively. A ratio of the NNN term $\mathcal{H}_{\mathrm{NNN}}$ of the NN term $\mathcal{H}_{\mathrm{BBH}}$ is controlled by the λ. We note that the C_4 symmetry still holds but the chiral symmetry is broken with finite λ. Hereafter, we consider the system with the half-filled electrons.

As illustrated before, non-trivial Berry phase is instinctive by considering the decoupled cluster limits, namely, $t_1 = 0$, $t_2 \neq 0$ and $t_1 \neq 0$, $t_2 = 0$. For the former case, the Hamiltonian

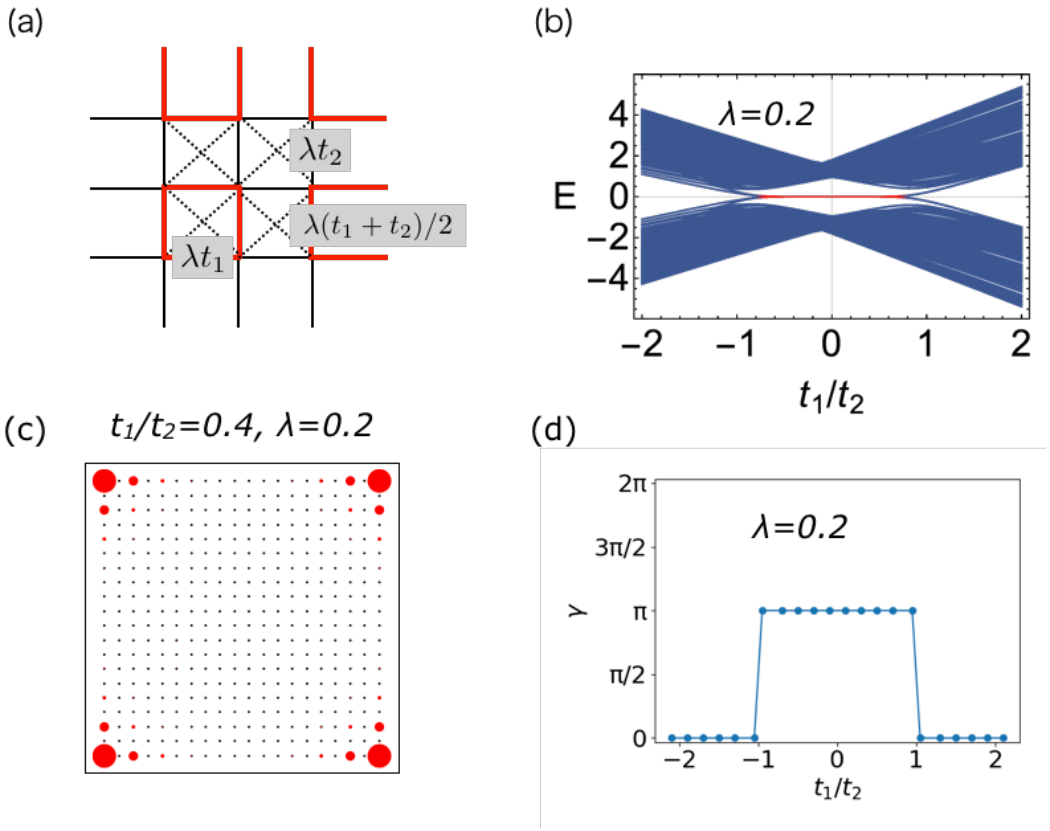

Figure 5.4: (a) The hopping parameters for next-nearest neighbour hopping is illustrated. The red and black lines are the nearest-neighbour hoppings with t_1 and t_2, respectively. (b) The one particle energies with $\lambda = 0.2$ against t_1/t_2. The system size is 20×20. On the red line, the corresponding state is the corner state. The phase transition occurs when $t_1/t_2 = \pm 1$. (c) The density plot for the four corner states of the system with $\lambda = 0.2$ and $t_1/t_2 = 0.4$. (d) The Berry phase against t_1/t_2 for the model with $\lambda = 0.2$. The non-zero Berry phases are corresponding with the HOTI phase.

can be expressed as $\mathcal{H} = \sum_{P\in\text{type-II}} h_P$. The ground state in this limit is simply the product state consisting of the plaquette state, $|\Psi_0^{\text{II}}\rangle = \prod_{P\in\text{type-II}} \left(\psi_{P,2}^\dagger \psi_{P,1}^\dagger |0\rangle_P\right)$. Here, the operators $\psi_{P,1}^\dagger$ ($\psi_{P,2}^\dagger$) are the lowest (second-lowest) energy state of the Hamiltonian for the chosen plaquette h_P. The $|0\rangle_P$ is the vacuum state of a plaquette P. Here, we define $|\Psi_0^{\text{II}}\rangle$ as the type-II plaquette state. In this limit the hopping terms on the type-I plaquettes is turned off, hence $\gamma^{\text{I}} = 0$. The Berry phase for the type-II plaquette γ^{II} is obtained to be $2\pi \times \frac{1}{2} = \pi$ (see Fig. 5.4(d)), which comes from the fact the quantized Berry phase is related to the filling factor in the decoupled cluster limit, as shown in Appendix 5.4. In next, we consider the finite t_1. In the present model, as long as $|t_1| < |t_2|$ is satisfied, the bulk band gap remains open with increasing t_1. Hence the Berry phase unchanges for finite $|t_1|$ ($< |t_2|$). The fact means the ground state of the model with the condition $|t_1| < |t_2|$ is adiabatically connected to the product state for the type-II plaquettes. Corresponding to the non-trivial Berry phase, four corner-state appears localized at the corners, which have nearly zero energies. One of the sample is shown in Fig. 5.4 (c). Differently, for the latter limit $t_1 \neq 0$, $t_2 = 0$, the ground state is adiabatically connected to the plaquette state of type-I $|\Psi_0^{\text{I}}\rangle$ as long as $|t_1| > |t_2|$ is held. For that case, the Berry phase of the ground state has the non-trivial value for the type-I plaquette $\gamma^{\text{I}} = \pi$ [see Fig. 5.4(d)]. Note that the

minimally decoupled states form the plaquette states for the ground state of $\mathcal{H}_0$. Because we cannot adiabatically deform the plaquette states to the atomic insulators, they are the "reference states" for the HOTI phases of the present model.

The model has the exact corner states for any λ and the localized corners are different between $|t_1/t_2| > 1$ and $|t_1/t_2| < 1$ as shown in Appendix 5.4. This implies that the higher-order topological phase transition occurs from the trivial phase to the HOTI phases at $t_1/t_2 = \pm 1$. Considering the model with the periodic boundary conditions, the quantized Berry phase for type-II plaquette turns into non-zero for the model with $|t_1/t_2| < 1$, This completely concurs in the HOTI phase. We note a relation between the Berry phases for the type-I and type-II plaquettes where γ^{I} with (t_1, t_2) is same to γ^{II} for (t_2, t_1). This fact express the duality for the type-I and type-II plaquettes. In conclusion, we have shown that there is the correspondence between the corner states in HOTI phases and $\mathbb{Z}_4$ Berry phases, and the quantized Berry phase characterizes the HOTI phase as a topological invariant.

5.2.2 The BBH model with intersite interactions

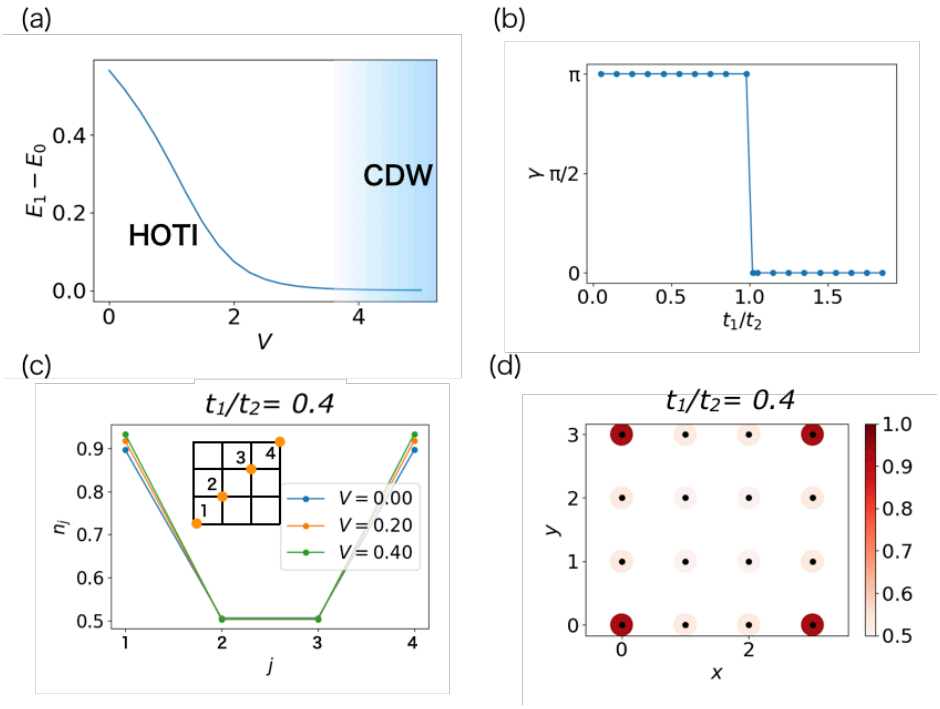

Figure 5.5: (a) The energy difference between the many-body first excited state and the many-body ground state of the model with periodic boundary conditions. The horizontal axis shows the intersite interaction V. We fixed $t_1/t_2 = 0.8$ and the lattice size is 4×4. The HOTI phase is overlapped to the CDW phase with finite V. (b) The quantized Berry phase for the BBH model with interactions. The strength of the intersite interactions is fixed to $V = 0.4$. (c)-(d) The ground state of the model with the open boundary condition is calculated, in which $(L \times L)/2 + 2$ electrons are filled. The system size is 4×4. The parameters are fixed to $V = 0.4$ and $t_1/t_2 = 0.4$. (c) The occupation number at representative sites indicated in the inset. (d) The color map of the occupation number of the electrons is shown.

In next, we investigate the HOTI/HOSPT phase with the intersite interactions. We calculate the many-body eigenstates and eigenenergies by the exact diagonalization using $\mathcal{H}\Phi$, which is the solver of the many-body lattice-model [102]. In the beginning, we consider

the BBH model with the nearest neighbour repulsive interactions, $\mathcal{H} = \mathcal{H}_0 + \mathcal{H}_{\rm int}$. Here,

$$\mathcal{H}_{\rm int} = V \sum_{\langle kl \rangle} \hat{n}_k \hat{n}_l \tag{5.9}$$

where $\hat{n}_k = \hat{c}_k^\dagger \hat{c}_k$ denotes the density operator of the electron at k-th site. We exploit the finite system that contains the $N = L \times L$ sites. We consider the half-filled systems for the bulk calculations. In the following, we take $\lambda = 0$ for simplicity.

From numerical calculations, we find that the many-body ground state under the periodic boundary condition has the gapped excitation for $V \geq 0$ [see Fig. 5.5 (a)]. For large V, present model goes to a charge density wave (CDW) phase. We note that, for the thermodynamic limit ($L \to \infty$), the quantum phase transition to the CDW phase from the HOTI phase will occur at $V = V_c$ upon increasing V. However, if V is smaller than the bulk energy gap, it is expected that the analysis in the following will be valid. Figure 5.5 (b) shows the Berry phase of the model with $V = 0.4$ against t_1/t_2. It is clearly seen that the topological phase transition occurs upon changing t_1/t_2.

Analogous to the non-interacting BBH model, the non-zero Berry phase implies the topologically non-trivial HOTI phase. For the sake to confirm it, we considered the model with open boundary condition and then calculated the spacial profile of the electron's charge distributions. In detail, we add two electrons into this system. It means the number of electrons is increased from half-filling $\frac{L\times L}{2}$ electrons to $\frac{L\times L}{2} + 2$. Then, we investigate the occupation numbers of electrons for this system. If there is a low-energy excitation that is localized at the corners, it is expected that the occupation numbers approaches to 1 at the corners. On the other hand, the occupation numbers at the rest of sites approaches to $1/2$. Hence that calculation is a hallmark for the higher-order topological phase.

Fig. 5.5 (c) shows the result. In this figure, the occupation numbers at corners are enlarged. On the other hand, the occupation numbers in the bulk sites are closed to $1/2$. This result express that the gapless excitations localized at the corners are the reminiscent of the zero-energy corner state of the non-interacting HOTI. In conclusion, we found that the higher-order topological phase with the gapless corner excitation exists in the interacting BBH model with the inter site interactions, and the quantized Berry phase characterizes the topological phase as a topological invariant, as is in the non-interacting model.

5.2.3 Spin-model-analogue of the BBH model

Secondly, we investigate the quantum spin analog of the BBH model [103] as an example for the HOSPT phase of the quantum many-body system:

$$\mathcal{H}_{\rm spin} = \sum_{\langle k,l \rangle} J_{kl} \left[\frac{1}{2} \left(S_k^+ S_l^- + S_k^- S_l^+ \right) + \Delta S_k^z S_l^z \right]. \tag{5.10}$$

Here, $\boldsymbol{S}_k$ denote the spin operator with $S = 1/2$ at the k-th site. $J_{kl} = J_1, J_2$ are the coupling constant between the NN sites. The configuration of the J_{ij} is the same as that of the hopping $t_{kl} = t_1, t_2$ of the BBH model. Δ is the Ising anisotropy – for $\Delta = 1$ ($\Delta = 0$), the spin model corresponds with the quantum Heisenberg-like model (the quantum XY-like model). By using the Jordan-Wigner transformation, the existence of the corner states of the present model has been discussed [103].

Here, we modify the Hamiltonian to define the quantized Berry phase by introducing the twisting parameters as

$$S_k^- \to e^{i\varphi_k} S_k^- \tag{5.11}$$
$$S_k^+ \to e^{-i\varphi_k} S_k^+ \tag{5.12}$$

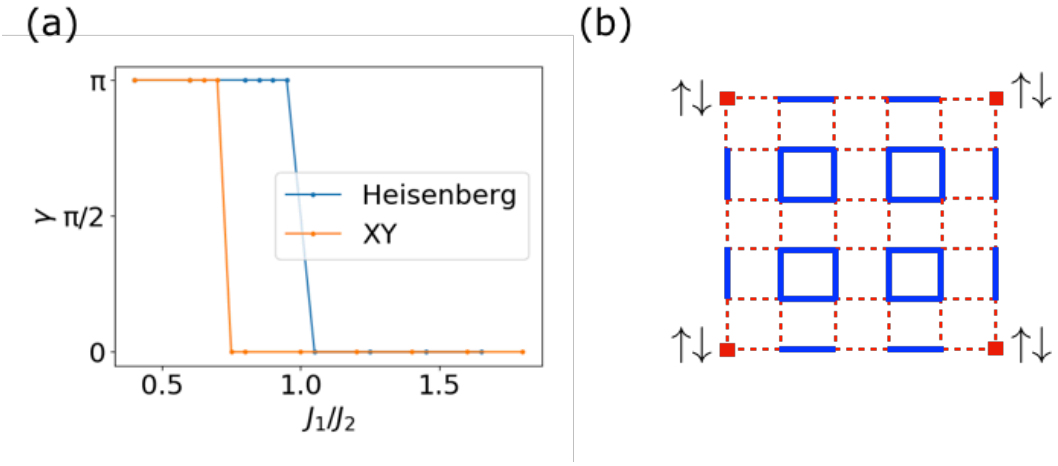

Figure 5.6: (a) The quantized Berry phases for the BBH-type spin model is shown. The blue (yellow) line denote the Berry phase for the model with $\Delta = 1$ ($\Delta = 0$) in Eq. 5.10, which corresponds the Heisenberg-like model (the XY-like model), respectively. (b) Schematic picture of the corner state for the model. The red (blue) lines denote the $J_1(J_2)$ interactions. If J_1 vanishes, the free spins emerge at corners.

on a specified plaquette belonging to either the type-I plaquettes or the type-II plaquettes. Thus, the quantized Berry phase is obtained in the same way to the Berry phase of the fermions. In Fig. 5.6 (a), the quantized Berry phase γ^{II} is shown. In the spin system, the Berry phase γ^{II} is clearly changed. In this figure, the Berry phase $\gamma^{\eta} = \pi$ implies that the decoupled cluster state of the type-η plaquettes can be obtained by adiabatic deformation from the state with non-trivial Berry phase, *i.e.*, the state belongs to the HOSPT phase. The schematic picture for the corner states is shown in Fig. 5.6 (b). In this figure, the red (blue) lines denote the $J_1(J_2)$ coupling. If J_1 vanishes, the free spins emerge at corners. This is the origin of the corner states of the model in the HOSPT phases. Fascinatingly, comparing to the BBH model of electrons, the XY model has the different phase transition point $J_1/J_2 \neq 1$. This means that there is an intermediate state where both of the quantized Berry phase of type-I and type-II plaquette equal to 0, which cannot be adiabatically connected to neither of the type-I or the type-II decoupled cluster states. It can be an artifact thing that arise from thee effect of the finite size. In the further studies, we need to identify the nature of this phase.

5.2.4 The BBH model in three-dimensions

Lastly, we analyze the 3D version of the BBH model by the quantized Berry phases. The Hamiltonian for the model is defined as [48, 49]

$$\mathcal{H}_0^{\mathrm{3D}} = -\sum_{\langle kl \rangle} e^{-i\alpha_{k,l}} t_{kl} \hat{c}_k^{\dagger} \hat{c}_l. \tag{5.13}$$

Here, $t_{kl} = t_1$ for the NN sites in the unit cells and otherwise $t_{kl} = t_2$, as the same fashion to the 2D version of the BBH model. The phase factors of the hopping parameters are set to $\alpha = \pi$ and 0 for the bonds colored in blue and black, respectively, as shown in Fig. 5.7 (a). The phases of the hopping parameters induce the π-flux in each of the surfaces of all the unit cells. The 3D BBH model has the HOTI phase for $t_1/t_2 < 1$. In Fig. 5.7 (b), the density plot for the corner states of the present model with $t_1/t_2 = 0.1$ is shown.

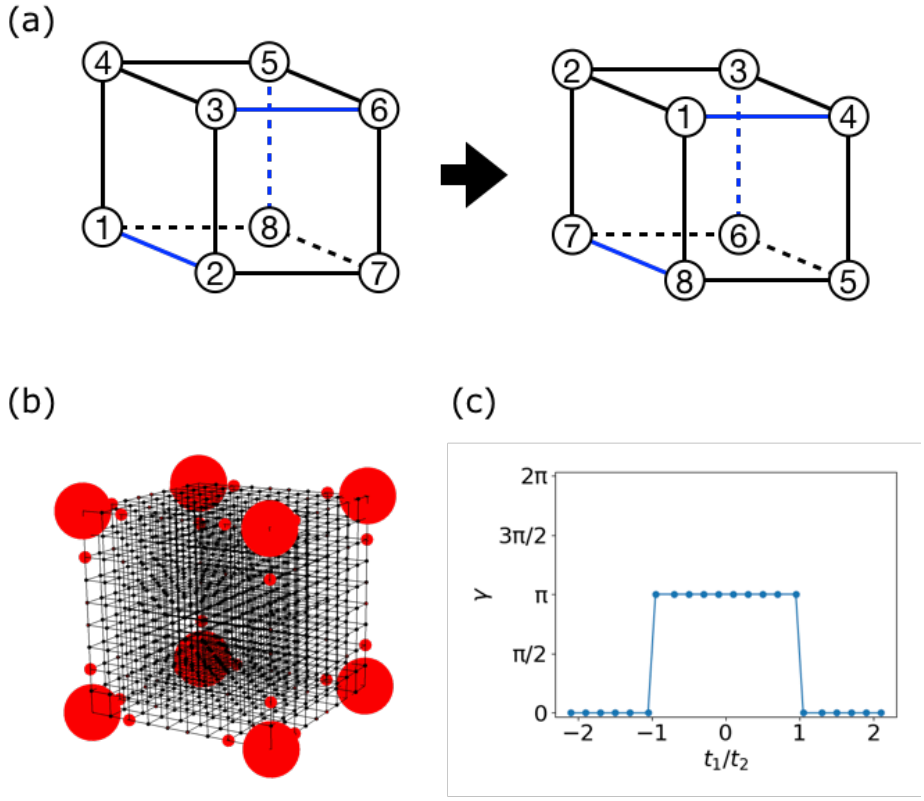

Figure 5.7: (a) This figure shows a unit cell for the 3D version of the BBH model. The model has the π-flux in each plane of the unit cell and the blue lines denotes that the hoppings between the sites having the $e^{-i\pi} = -1$ phase. The $\mathbb{Z}_4$ symmetry operates the system to change the basis in the unit cell from the left to the right figure. (b) Density plot of the corner states with $t_1/t_2 = 0.1$ is shown. The system size is 10×10. (c) The quantized Berry phase for the present model as the function of t_1/t_2.

Now we define the quantized Berry phase. We again introduce the twisting into the Hamiltonian as

$$\hat{c}_k \to e^{i\varphi_k}\hat{c}_k \tag{5.14}$$

with $\varphi_k = \sum_{m=1}^{k}\theta_m$ for $k = 1, 2, \cdots, 8$ and a condition $\varphi_8 = 0$. Thus, we have seven independent twisting parameters $\boldsymbol{\theta} = (\theta_1, \cdots, \theta_7)$. Figure 5.7 (a) shows the $\mathbb{Z}_4$ symmetry, under which the model Hamiltonian is invariant. There are $\mathbb{Z}_8$ symmetry which cycle the indices of the sites in a unit cell. The model Hamiltonian is invariant under the two operations, hence the model has the $(\mathbb{Z}_8)^2 = \mathbb{Z}_4$ symmetry. We define paths $L_j (j = 1, 2, \cdots, 8)$ in the parameter space as $\boldsymbol{E}_{k-1} \to \boldsymbol{G} \to \boldsymbol{E}_k$ where $\boldsymbol{E}_1 = (2\pi, 0, \cdots, 0)$, $\cdots$, $\boldsymbol{E}_7 = (0, 0, \cdots, 2\pi)$, $\boldsymbol{E}_8 = \boldsymbol{E}_0 = (0, 0, \cdots, 0)$, and $\boldsymbol{G} = 1/8\sum_{k=1}^{8}\boldsymbol{E}_k$. Because of the $\mathbb{Z}_4$ symmetry, an equation of the Berry phase $\gamma_j = -i\oint_{L_j} d\boldsymbol{\theta}\cdot\boldsymbol{A}(\boldsymbol{\theta})$ holds:

$$\gamma_1 + \gamma_2 = \gamma_3 + \gamma_4 = \gamma_5 + \gamma_6 = \gamma_7 + \gamma_8 \equiv \gamma \mod 2\pi. \tag{5.15}$$

Combining to the equation $\sum_k \gamma_k = 0$, the Berry phase γ is quantized in $\mathbb{Z}_4$.

In Fig. 5.7 (c), the Berry phase γ is shown as a function of t_1/t_2. The figure clearly shows the non-trivial Berry phases characterize the HOTI phase in $t_1/t_2 < 1$.

5.3 Conclusion

The $\mathbb{Z}_4$ Berry phase has been demonstrated to characterize the HOTI/HOSPT phases of the square lattice models under the C_4 symmetry. The main idea is based on the fact that the ground states are adiabatically connected to the product states of the irreducible decoupled clusters. In these systems, the bulk-corner correspondence between the bulk Berry phase and the corner state of the HOTI phases is naturally explained as a consequence that the isolated site(s) appears if the cluster with non-trivial Berry phase is cut at the corner. Numerical evidences of the above statement are presented for the BBH model with NNN hopping term, the BBH model in the presence of NN intersite interactions, and the spin model that is analogous to the BBH model. Furthermore, we have found that the $\mathbb{Z}_4$ Berry phases correspond the HOTI phases of the 3D BBH model as well.

In this chapter, we have investigated the BBH type models with the C_4 symmetry. Here, we should note the symmetries which protect the BBH model. Previous study in Ref. [49,104] argues that it is enough to protect the HOTI phases by two mirror symmetries, instead of the C_4 symmetry. If two mirror symmetries are preserved while the C_4 symmetry is broken, the ground state can be adiabatically connected to the valence-bond-solid (VBS) state for the strong bonds, where the conventional $\mathbb{Z}_2$ Berry phase capture the VBS states [35,38,105]. However, the VBS states are not the irreducible-cluster state at the C_4-symmetric point since it does not preserve the C_4 symmetry. As a consequence, the $\mathbb{Z}_2$ Berry phase is ill-defined at the point. Thus it is necessarily to use the $\mathbb{Z}_4$ Berry phase for these systems.

We note that the models with the C_N symmetry or the $\mathbb{Z}_N$ symmetry are good examples to straightforwardly apply the quantized Berry phase. The examples include the $\mathbb{Z}_6$ Berry phase for C_6 symmetric honeycomb lattice model [106] and the $\mathbb{Z}_3$ Berry phase for C_3 symmetric breathing kagome model [91, 107]. Because various models for the HOTI/HOSPT phases with the C_N or the $\mathbb{Z}_N$ symmetries have been proposed [108], we believe the $\mathbb{Z}_N$ Berry phases serve as a useful tool for studying such phases.

5.4 Appendix

Berry phase for decoupled clusters

Before we show the bulk-corner correspondence, we calculate the quantized Berry phase for a decoupled cluster of the HOTIs. We contemplate the single cluster, which consists of N sites and also the Hamiltonian of the single cluster is under $\mathbb{Z}_N$ symmetry, *i.e.*, the Hamiltonian is invariant with the cyclic operation $c_j \to c_{j+1},\ c_{N+1} = c_1$. Here, $c_j (j = 1, \cdots, N)$ denote an annihilation operator for i-th electron.

Then, we consider the many-body ground state $|\Psi\rangle$. The unitary operator for the bond-twisting is defined as

$$U = e^{-i\varphi_1 n_1} e^{-i\varphi_2 n_2} \cdots e^{-i\varphi_{N-1} n_{N-1}}, \tag{5.16}$$

where $\varphi_j = \sum_{i=1}^{j} \theta_i,\ \varphi_N = 0$. By the unitary operator U, the annihilation operators of electrons are connected

$$U c_j U^{-1} = e^{i\varphi_j} c_j. \tag{5.17}$$

Hence, the ground state of the modified Hamiltonian $\mathcal{H}(\boldsymbol{\theta})$ is given as

$$|\Psi(\boldsymbol{\theta})\rangle = U\,|\Psi\rangle\,. \tag{5.18}$$

Here, we can show that the expectation of the number of electron is not changed by $\boldsymbol{\theta}$ as

$$\begin{aligned} \langle n_j \rangle_{\boldsymbol{\theta}} &= \langle \Psi(\boldsymbol{\theta}) | n_j | \Psi(\boldsymbol{\theta}) \rangle & (5.19)\\ &= \langle \Psi | U^\dagger n_j U | \Psi \rangle & (5.20)\\ &= \langle \Psi | n_j | \Psi \rangle = \langle n_j \rangle\,. & (5.21) \end{aligned}$$

In next, let us introduce paths $L_j, (j = 1, \cdots, N)$ (see Fig. 5.2) to define the Berry phase,

$$\begin{aligned} L_1 &: \boldsymbol{O} \to \boldsymbol{G} \to \boldsymbol{E}_1 \\ L_2 &: \boldsymbol{E}_1 \to \boldsymbol{G} \to \boldsymbol{E}_2 \\ &\cdots \\ L_N &: \boldsymbol{E}_{N-1} \to \boldsymbol{G} \to \boldsymbol{O} \end{aligned} \tag{5.22}$$

where $\boldsymbol{E}_j = 2\pi \boldsymbol{e}_j$ and $\boldsymbol{G} = 1/N \sum_{j=1}^{N-1} \boldsymbol{V}_j$. The $\{\boldsymbol{e}_j\}$ is the unit vectors in the parameter space. We then have

$$\sum_{j=1}^{N} \gamma_j = 0 \ (\mathrm{mod}\ 2\pi). \tag{5.23}$$

because the Berry phases on each paths are canceled each other.

By explicitly parameterize the path, the Berry phase can be calculated. By using Eq. (5.18), we obtain

$$\begin{aligned} d\boldsymbol{\theta} \cdot \langle \Psi(\boldsymbol{\theta}) | \frac{\partial}{\partial \boldsymbol{\theta}} | \Psi(\boldsymbol{\theta}) \rangle &= dt\, \langle \Psi(\boldsymbol{\theta}) |\, \partial_t\, | \Psi(\boldsymbol{\theta}) \rangle \\ &= -idt \frac{\partial \theta_1}{\partial t} (\langle n_1 \rangle + \langle n_2 \rangle + \cdots + \langle n_{N-1} \rangle) \\ &\quad -idt \frac{\partial \theta_2}{\partial t} (\langle n_2 \rangle + \cdots + \langle n_{N-1} \rangle) \\ &\quad - \cdots - idt \frac{\partial \theta_{N-1}}{\partial t} \langle n_{N-1} \rangle\,. \end{aligned} \tag{5.24}$$

Here, the real number t parameterizes the path. In the path L_j $(j = 1, \cdots, N)$, only the $\frac{\partial \theta_j}{\partial t}$ is 2π and the others $\frac{\partial \theta_{k\neq j}}{\partial t}$ are zero. Hence, the Berry phase expressed as

$$\gamma_j = -i \int_{L_j} \langle \Psi(\boldsymbol{\theta}) | \, \partial_t \, | \Psi(\boldsymbol{\theta}) \rangle \, dt, \tag{5.25}$$

are calculated as

$$\begin{aligned} \gamma_1 &= 2\pi(\langle n_N \rangle - N) \\ \gamma_2 &= 2\pi \langle n_1 \rangle \\ &\cdots \\ \gamma_N &= 2\pi \langle n_{N-1} \rangle . \end{aligned} \tag{5.26}$$

Here, the integer $N = \sum_{j=1}^{N} \langle n_j \rangle$ is the total number of electrons in the cluster, Hence, $\gamma_1 = 2\pi \langle n_N \rangle \pmod{2\pi}$.

Due to the C_N symmetry, we can conclude the density of the electrons are

$$\langle n_1 \rangle = \cdots = \langle n_N \rangle \equiv \nu \tag{5.27}$$

where ν is the filling factor of the electrons in a unit cell. Finally, to combine Es. (5.23) and (5.27), we find the Berry phase for the decoupled clusters is $\gamma_1 = \cdots = \gamma_N \equiv \gamma = 2\pi\nu \bmod 2\pi$, $n \in \mathbb{Z}$.

The exact corner states of the BBH model with the NNN hopping

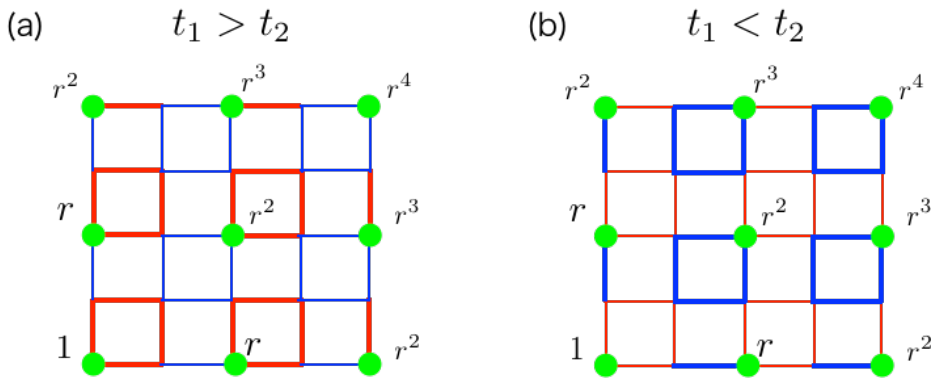

Figure 5.8: The exact corner state for the model with the NNN hoppings is illustrated for (a) $t_1 > t_2$ and (b) $t_1 < t_2$. The corner state has finite amplitude only at the sites colored in green. (a) The corner state is localized at the right-top corner. (b) The corner state is localized at the left-bottom corner.

Now we consider the BBH model with NNN hopping with the lattice sites of $L_x \times L_y$ and the lattice size is $L_x = 2N_x + 1$ and $L_y = 2N_y + 1$. In this case, the model has the exact zero-energy corner state, which is expressed as

$$|\psi_0\rangle = \frac{1}{\mathcal{N}} \sum_{k,l=0}^{N_x,N_y} r^{k+l} \, |2k+1, 2l+1\rangle \, , \tag{5.28}$$

where $\mathcal{N}$ is the normalization constant. The amplitude of the electrons are finite for only $(N_x + 1) \times (N_y + 1)$ sites but zero for other sites (see Fig. 5.8). The proportion $r = -t_1/t_2$

determines the localization length of the corner state. $|i,j\rangle$ is the basis of the eigen space at the site (i,j). It is confirmed that the state satisfies $\mathcal{H}\,|\psi_0\rangle = 0$, by the straightforward calculation. This means the corner state is the zero-energy eigenstate of the present model. When $|t_1| < |t_2|$, the corner state is localized at the position $(1,1)$ and the localization length is $-1/\log|\mathrm{r}|$. On the other hand, when $|t_1| > |t_2|$, the corner state is localized at the positions (L_x, L_y).

The zero-energy state in Eq. (5.28) is valid for the lattice size of odd L_x and L_y. For the even lattice size, four corner states emerge. The energies of the corner states are not exactly zero due to the finite size effect, which are seen in Fig. 5.4 (b). However, the exactly zero energy state in Eq. (5.28) is a nicely approximate the corner states for sufficiently large systems. As the exactly zero energy state has the exponential localization, the corner states are orthogonal for the sufficiently large systems.

Chapter 6

Machine learning study for the disordered higher-order topological insulators

This chapter investigate tight-binding model of a breathing kagome lattice [50–52, 91]. As explained before, the tight-binding model exhibits the higher-order topological insulator phase having zero-dimensional corner mode protected by mirror and three-fold rotational symmetries [50–52]. Firstly, we apply the supervised learning for this model in the clean limit, in which the topological phase diagram has been already known [50–52]. Then, we introduce the disorders as on-site potentials and determine the phases by using the supervised neural-network for classification. We can get the phase diagram for the disordered kagome higher-order topological insulator model of both triangle and rhombus geometries. We have found that as long as the energy gap does not collapse,the HOTI phase survives because of the robustness of the topological corner states versus disorders.

We organize this chapter as following. Section 6.1 shows the model we study in the chapter and reviews a phase diagram of the model in a clean limit. We also summarized the topological invariant that is proposed in the previous works and the symmetries of the model. Section 6.2 explains the machine learning method we use in this chapter, It is the supervised learning and identifies the phases of the model with disorders. Section 6.3 presents the main results of the study. We applied the machine learning method to the disordered HOTI model and the method successfully generated a phase diagram of the model, which is compared to the analytical method, the inverse participation ratio. In Sec. 6.4, we summarize the study and present discussions.

6.1 Disordered kagome higher-order topological insulators

In the beginning of this section, we introduce a tight-binding Hamiltonian on a breathing kagome lattice for spinless fermions, as shown in Chapter 3

$$\mathcal{H}_0 = -\sum_{k,l} t_{kl} c_k^\dagger c_l, \tag{6.1}$$

Here, c_k and $c_k^\dagger$ are the annihilation and the creation operators of an electron on a k-th site, respectively The $t_{kl} = t_2(t_1)$ are the hopping parameters between k and l, which belong to the NN bonds living on the downward (upward) triangles [Fig. 6.1(a) and 6.1(d)]. We set $t_2 = 1$ in the following.

To diagonalize the Hamiltonian $\mathcal{H}_0$ in a Fourier space, the bulk spectrum is obtained. In this model, a flat band appears in the energy of $t_1 + t_2$. There are a band gap between the rest two bands if $|t_1| \neq |t_2|$. If $t_1 = t_2$, there appears the gapless linear dispersions at K and K' point. If $t_1 = -t_2$, the gapless linear dispersion appear at Γ point.

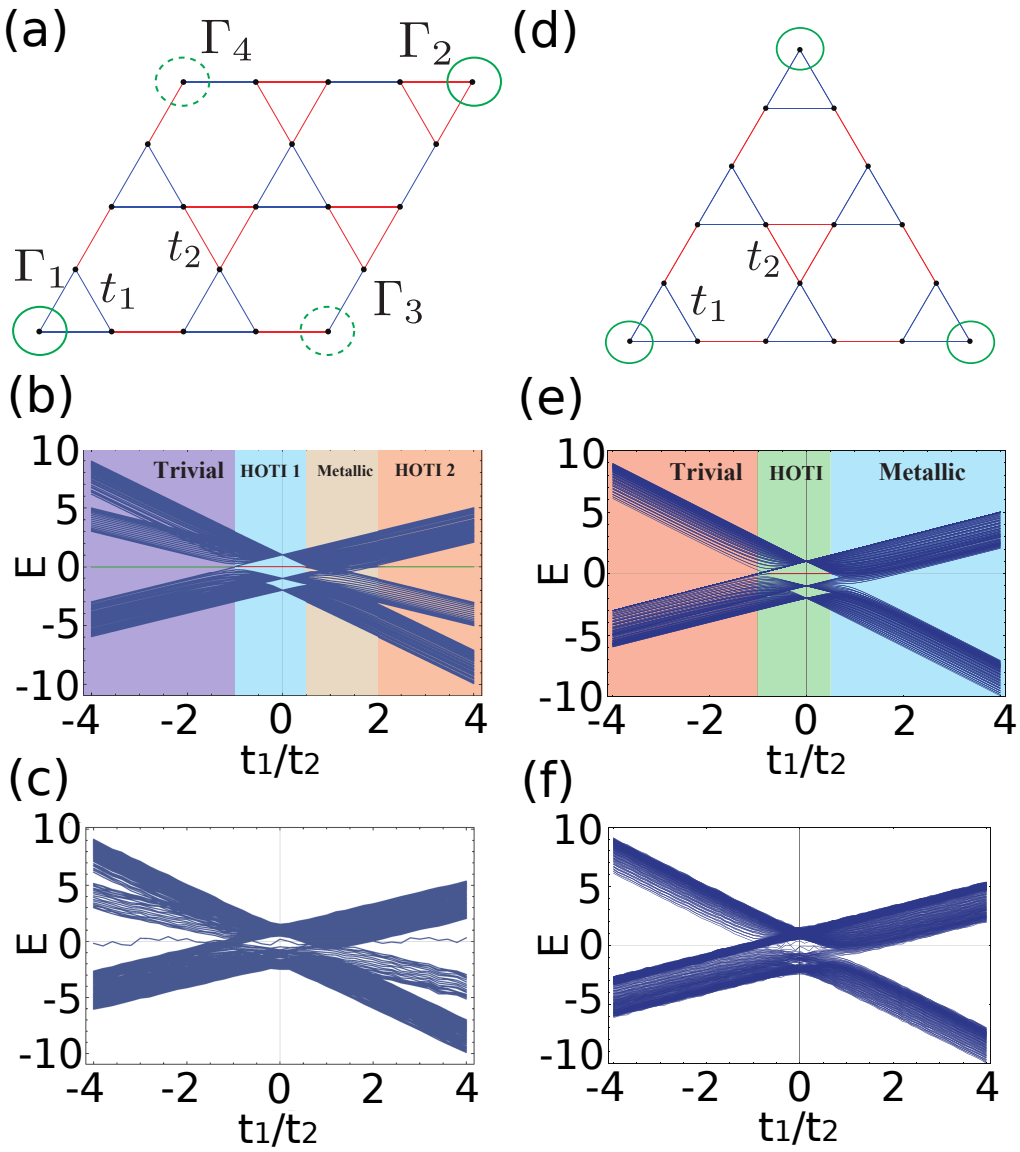

Figure 6.1: In (a)/(d), a flake of the kagome lattice with a rhombus/triangle geometry is shown. In each geometry, the green circles denotes the corners. In (b) and (e), the energy spectrum as a function of t_1/t_2 for a rhombus and triangle geometry are shown, respectively. In (c)/(f), the energy spectrum for the present model in a rhombus/triangle geometry with the disorder strength $W = 1.1$ are shown.

6.1.1 Phase diagrams for rhombus and triangular geometries in the clean limit

Let us consider the finite system with an open boundary condition to study HOTI phases of the present model. As yet, rhombus and triangular geometries are chosen to generate the

finite system [see Fig. 6.1(a) and 6.1(d)]. In the model of these geometries has HOTI phases with the corner states, which is the zero-dimensional localized states at corners [50–52]. To consider the limit for $|t_1| = 0$ or $|t_2| = 0$, the existence of the corner states can be understood. For example, if we consider the $|t_1| = 0$ limit, there are "dimers" aligning on the edges of the triangular or rhombus geometry, which do not reside in the downward triangles, and there are the "trimers" in the bulk, which forms all downward triangles. In the rhombus geometry, only the site at Γ_1 corner is isolated, which generates a zero-energy corner state, The corner states survive even with $t_1 \neq 0$ as far as $|t_1| < |t_2|$ is satisfied, Likewise, there the corner state localized at the Γ_2 corner for $|t_1| > |t_2|$. Actually, as shown in Ref. [51], the exact zero-energy corner states for the system with $|t_1| \neq |t_2|$ are explicitly constructed. We note that there are no corner states which is localized at Γ_3 and Γ_4 for any t_1 and t_2. On the other hand, in a triangular geometry, because there are three corners that belong to the upward triangles, the corner modes appear at three corners if $-1 \leq t_1/t_2 \leq 1/2$ and the corner modes have three-fold degeneracy [50].

To define the phases, the difference between the corner states of the system with different geometry is crucial. The corner state appears for every parameter in a rhombus geometry, however it is matter whether the corner state is the in-gap state or not. Therefore, for the classification of the phases, we fix the number of electrons such that $N = M^2 = \nu_{\mathrm{R}}$. Here, we contemplate the system consists of $M \times M$ rhombuses or $3M^2 - 2M$ sites and consider the highest occupied (single-particle) state. Figure 6.1(b) shows four phases of the model as a function of t_1/t_2. The system is in the HOTI phase for $t_1/t_2 > 2$, in which there are zero-energy state in a band gap localized at the Γ_2 corner. We refer to the phase as "HOTI 2", which is named after the position of the corner state. The system is in the metallic phase for $1/2 < t_1/t_2 < 2$, in which the zero-energy corner state is buried in the bulk and edge states. There is another HOTI phase in $-1 < t_1/t_2 < 1/2$, where a zero-energy state appear and the state is localized at the Γ_1 corner. We refer to this phase as "HOTI 1". There is a "trivial" phase for $t_1/t_2 < -1$, where there is a zero-energy state which is localized at the Γ_2 corner, but it is not the highest occupied state for fixed ν_R. In this phase, the highest occupied state is one of the degenerated flat band states.

In contrast to the rhombus geometry, three phases exist for the system in a triangle geometry. In this geometry, there is only a HOTI phase in $-1 \leq t_1/t_2 \leq \frac{1}{2}$ [50]. There are three corner states at $(\nu_{\mathrm{T}} - 1)$-th, ν_{T}-th, and $(\nu_{\mathrm{T}} + 1)$-th states in the phase. Here, $\nu_{\mathrm{T}} = \frac{M(M+3)}{2}$ and the system has $\frac{M(M-1)}{2}$ number of upward triangles pr $\frac{3M(M-1)}{2}$ sites. So that the highest occupied state in this region becomes one of the corner states, we fix the number of electrons as $N = \nu_{\mathrm{T}}$. There are two other phases, the trivial phase for $t_1/t_2 \leq -1$ and the metallic phase for $t_1/t_2 \geq 1/2$. Essentially, they are same as the phases in the rhombus geometry.

6.1.2 Symmetries and topological invariants

As yet, previous studies revealed that the symmetries of the Hamiltonian protects the zero-energy corner state in the HOTI phase. However, according to the geometry of the system, the protecting symmetries and corresponding topological invariants are different. Firstly, we consider the triangle geometry. In this case, the distance of the "Wannier center" from the origin, P_3, is quantized as 0 for the trivial phases and 1/2 for the HOTI phase [50]. The quantization of P_3 originates from the three mirror symmetries. Next we consider the rhombus geometry. In this case, the topological invariant can be obtained from the trajectory of the eigenvalues of the "Wannier Hamiltonian" during the adiabatic deformation of the Hamiltonian [52]. Then, the composite operation of symmetry for complex conjugation and the three-fold rotation protects the corner state in the HOTI phase.

One important thing is that the spacial symmetries are crucial for both of these geometries for the Hamiltonian, while these symmetries are broken by random impurity potentials. Therefore, the quantization of the above topological invariants are also broken in the disordered systems. In addition, as seen in Figs. 6.1(c) and 6.1(f), the corner state in the HOTI phase has non-zero energy any further. Hence for the system with disorders, the definition of the HOTI phases is more or less subtle, but it may be reasonable to adopt whether the corner states exist or not as a working definition of the HOTI phase with disorders. For the sake of detecting the (disordered) HOTI phases in the definition, it is suitable to apply the machine learning method. This method can detect the corner states existing in the gap, systematically.

6.1.3 Effect of disorders

As an effect of disorders, the on-site random potentials are introduced as

$$\mathcal{H}_R = \sum_j w_j \hat{c}_j^\dagger \hat{c}_j \tag{6.2}$$

where w_j is a randomness in the uniform distribution of $[-W/2, W/2)$. The W denotes the strength of the random potentials. Here after, we consider the total Hamiltonian as $\mathcal{H} = \mathcal{H}_0 + \mathcal{H}_R$.

6.2 Identification of the topological phase by machine learning

In this section, we introduce a detection method for the disordered phases of HOTIs by the state-of-the-art machine learning technique. In this study, we use an algorithm based on a neural network, which is implemented by PyTorch [109] that is the open-source library for Python.

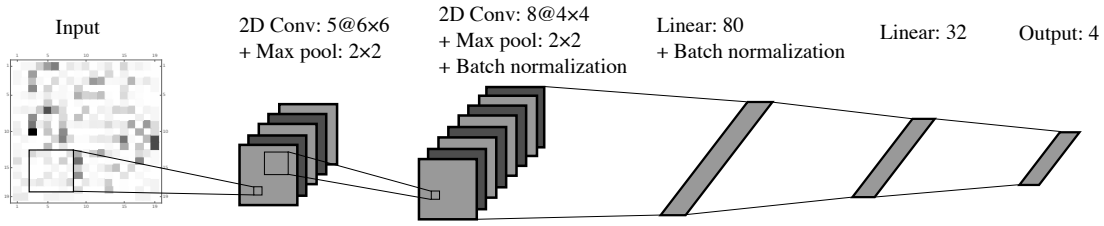

Figure 6.2: An configuration of the artificial neural network is shown. The first and the second layers are the convolutional neural-network layers for two-dimensions. The rests of the layers are the ordinal linear layers. The batch normalization and the max pooling layers are used. The figure also shows the size of the layers.

6.2.1 Configuration of the neural network

Figure 6.2 shows a schematic picture of the configuration of the multi-layer neural network used in the chapter. The configuration contains five artificial neural network, in which first two layers are the convolutional neural network. The rests of them are the linear layers. We take the activation functions as the ReLU functions $f(x) = \max(0, x)$. The max pooling layers are inserted after the convolutional neural networks. We insert the batch normalization

layer after the second convolutional neural network and the first linear layer. The max pooling layer takes the max value in 2×2 sectors. The outputs of the neural networks are the probabilities of phases. Corresponding the number of phases for clean systems, the number of output is three for triangle geometry and four for rhombus geometry.

6.2.2 Input and output data

Our input data is the electron densities of the single-particle highest occupied state. The machine learning method that we show in the following is similar to the method for the first order TI developed in Ref. [73, 75]. First we consider the rhombus geometry. With $c_{\nu_\mathrm{R}} = \sum_i \phi_i^{\nu_\mathrm{R}} c_i$, as the annihilation operator of the state ν_R, the input data for this case is $|\phi_i^{\nu_\mathrm{R}}|^2$. Next we consider the triangle geometry. In this case, we use the average density of electrons among three corner states, $(|\phi_i^{\nu_\mathrm{T}-1}|^2 + |\phi_i^{\nu_\mathrm{T}}|^2 + |\phi_i^{\nu_\mathrm{T}+1}|^2)/3$, as the input data. In this geometry, the specific choice is reasonable because the C_3 symmetry is preserved. We note that since it is useful to detect corner states of the HOTIs, we adopt the choices of the input data. Other possible choices of the input data can be considered, such as the topological numbers [110] and the all of the occupied states [71].

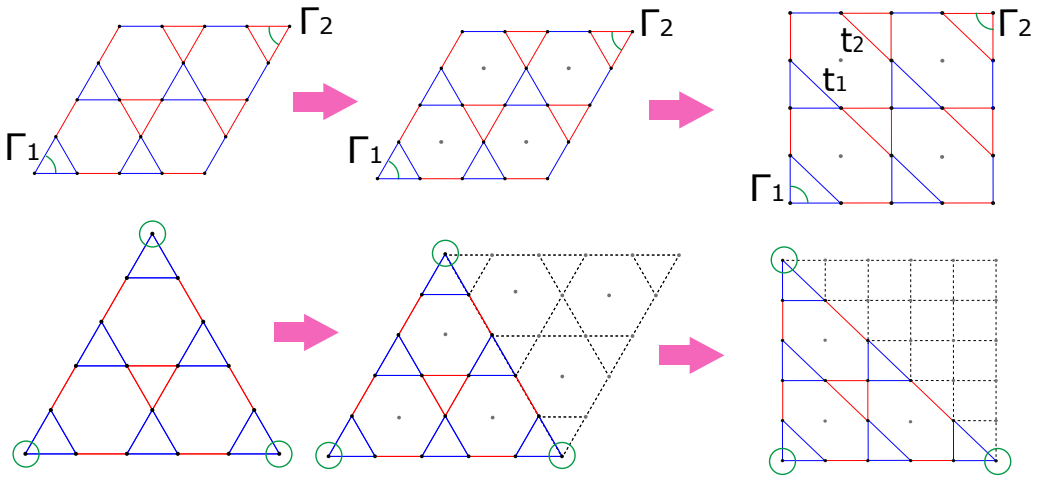

Figure 6.3: A schematic picture for the modification is shown. The kagome lattice is modified to the square lattice. The upper (lower) figures show the modification for the rhombus (triangular) geometry. The gray circles are the artificial sites we added.

We transform the geometry from a kagome lattice to a square lattice in order to make the input data as two-dimensional square-shaped images, [Fig. 6.3]. The vacancy sites are inserted for the input data. Firstly let us consider the rhombus geometry. This deformation from the equilateral triangles to the right triangles is accomplished by appending redundant sites at the centre of the hexagonal plaquettes. We take the zero probability at the additional sites for the single-particle wavefunctions of the input data. This proceeding increases the size of image data from $3N$ to $4N$. Here N denotes a number of unit cells. We note that the deformation do not lose any information, although the computational cost is increased. Next, let us consider the triangle geometry. Similar to the rhombus geometry, the redundant sites at the center of the plaquettes are inserted. Furthermore, it is necessarily to append a large downward triangle, which consists of the redundant sites. Then, the probabilities of more than half of the sites are zero in the deformed image. Finally we consider the output data. For rhombus (triangular) geometry, the output data are four- (three-) dimensional vectors. The components of the vectors correspond the probabilities for the phase that the

neural network estimates.

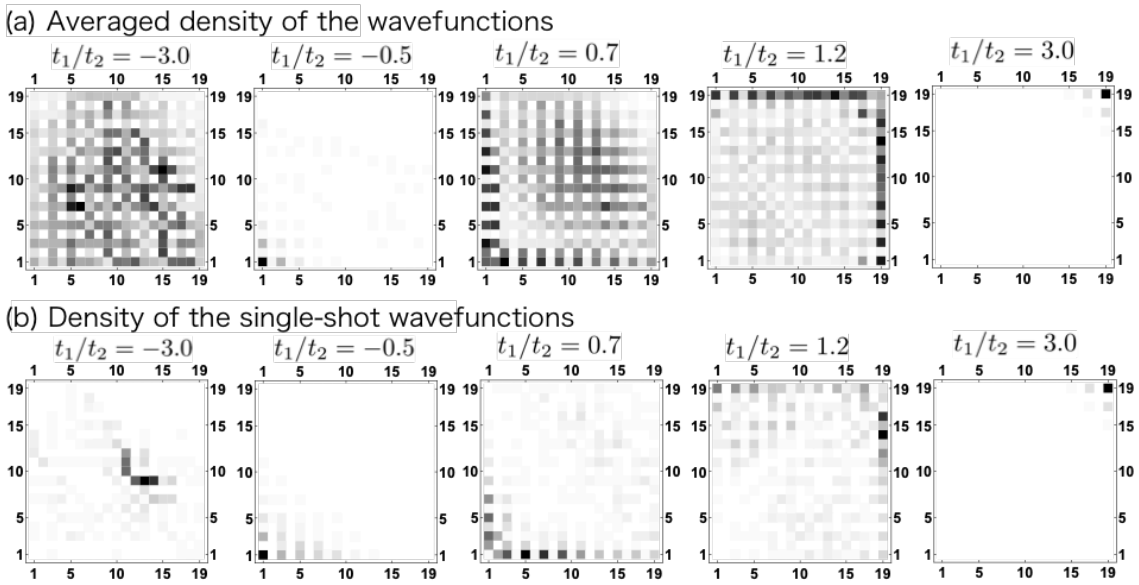

Figure 6.4: The probability density of the wavefunctions is shown for a rhombus geometry. (a) The averaged densities of the wavefunctions of the highest occupied state are shown. We used 30 samples to calculate the averaged density of the wavefunctions. (b) The densities of single-shot wavefunctions of the highest occupied state are shown. Both of them, the disorder strength is set to $W = 1$.

6.2.3 Supervised learning

Firstly, we do a supervised learning to optimize the parameters of the model to classify the phases. To achieve that, we randomly choose the t_1/t_2 and then obtain the highest occupied state of the Hamiltonian in the clean limit. Then, the 5000 images, *i.e.* the probability density of the state, are prepared. The label of each image is the phase corresponding with the randomly-chosen parameter and the label is represented as a three- (four-) dimensional vector for a triangular (rhombus) geometry. We use the one-hot representation, in which only n-th component is 1 and all the other components are 0 for the label of the n-th phase. We employ the cross entropy as the loss function. Then, we train the model such that the loss function is minimized. To achieve that, a kind of the gradient method is used to update the parameters of the model. Here we note that the trained model can reproduce the label of the test data over 99% of accuracy.

In next, we use the trained model to identify the phases of the systems with disorders. To accomplish that, we take the probability density of the state of the system with disorders as the input data for the trained model. Then, we adopt the output vectors as the probabilities for the phases of the input data. To averaging the state, 30 samples are prepared for chosen parameters of W and t_1/t_2. Then, we take two distinct methods to average the densities of these states to investigate the phase diagram as follows. Firstly, we take an average for the input data, *i.e.*, the probability densities are averaged over the samples. The disorders break the translational symmetry but the averaging process is needed to restore the symmetry, as mentioned in Ref. [75]. The second way of averaging is taking the average of output data. In this way, we take an average over the obtained output vectors for 30 samples of the single-shot wavefunctions. The two ways of averaging complement each other. Because the randomly-localized states are uniformly distributed, the former way of averaging is expedient

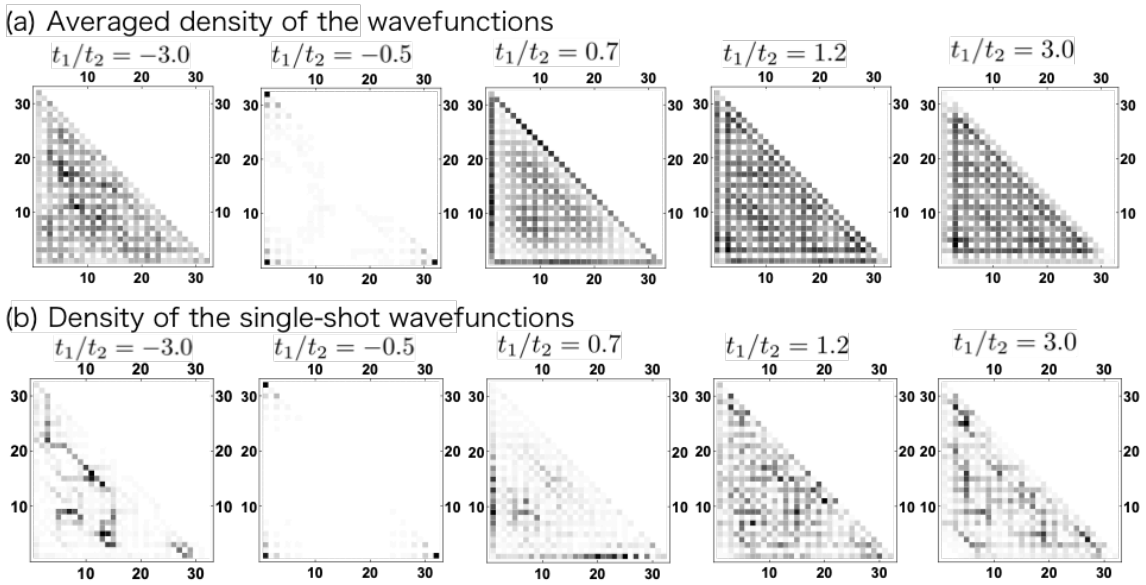

Figure 6.5: The probability density of the wavefunctions is shown for a rhombus geometry. (a) The averaged densities of the wavefunctions of the highest occupied state are shown. We used 30 samples to calculate the averaged densities of the wavefunctions. (b) The densities of the single-shot wavefunctions of the highest occupied state are shown. Both of them, the disorder strength is set to $W = 1$.

for large W to distinguish the corner states from the randomly-localized states. Although, because the probability density of all of these states is uniform, this way of averaging has no capacity of distinguishing the randomly-localized states, the trivial states and the metallic states. On the other hand, because the single-shot wavefunctions has clear difference of them, the latter way of averaging can distinguish them.

In next, we see the averaged probability density of the wavefunctions and the single-shot wavefunctions. Figure 6.4 (a) and Fig. 6.5 shows the averaged densities of the wavefunctions for a rhombus geometry and a triangular geometry, respectively. The disorder strength is fixed to $W = 1$. In Fig. 6.4 (b) and Fig. 6.5 (b), the single-shot wavefunctions for a rhombus geometry and a triangle geometry, respectively. The parameters of the model Hamiltonian are same to the averaged densities of the wavefunctions. For the wavefunction at $t_1/t_2 = -3.0$, the flat-band states are dominant in the single-shot wavefunctions. and we can clearly see that the averaging restores the translational symmetry. Let us see the other phases. As we will see later, the corner states can be seen in both the single-shot and averaged wavefunctions. Hence, they can serve as a fingerprint of the HOTI phases for the neural network.

6.3 Disordered higher-order topological insulator phases

6.3.1 Result for the rhombus geometry

Firstly, let us contemplate the rhombus geometry. We take the system size of $M = 10$. Here we generate phase diagrams in two ways. Figure 6.6 (a) shows the phase diagram generated by averaged densities of the wavefunctions. On the other hand, Fig. 6.6 (b) shows the phase diagram generated by the single-shot wavefunctions. In the figures, the right-blue, orange, yellow and blue colors represent the HOTI 1, HOTI 2, metallic and trivial phase, respectively.

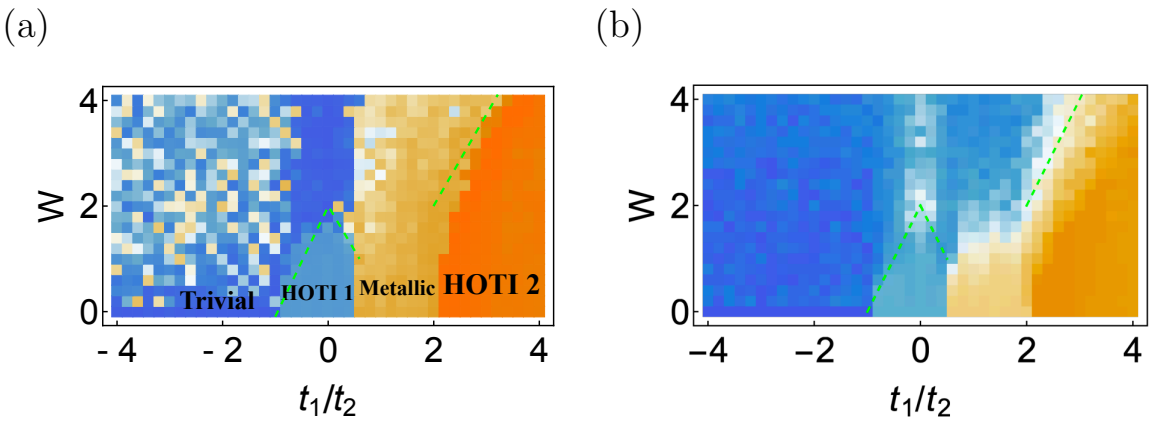

Figure 6.6: The phase diagram for the kagome HOTI model for the rhombus geometry, which contains the terms for disorders. (a) The phase diagram is plotted for the averaged densities of the wavefunctions. Here, orange, yellow, right-blue and blue regions denote the HOTI 2 phase, the metallic phase, the HOTI 1 phase and the trivial phase, respectively. The energy gap between the corner states and the bulk *or* edge states are shown as green dashed line. (b) plots the phase diagram by the calculation of the averaged probabilities, which is averaged over 30 densities of the single-shot wavefunctions.

Firstly, we contemplate the HOTI phases. The HOTI phases remain to the critical disorder strength as seen in both of two phase diagrams. For $W > W_c^{(1)}$, the HOTI 1 phase take transition to the trivial phase. On the other hand, the HOTI 2 phase turns into the gapless phase for $W > W_c^{(2)}$. These phase transitions indicate that the level cross between the states nearby zero-energy and the corner states occurs in these regimes. For these cases, $W_c^{(1,2)}$ can be estimated by the energy gap between the nearby bulk/edge states and the corner states. To specify it, the formulae for $W_c^{(1)}$ are $-2t_1/t_2 + 2$ for $0 \leq t_1/t_2 \leq 1/2$ and $2t_1/t_2 + 2$ for $-1 \leq t_1/t_2 \leq 0$. Similar to that, those for $W_c^{(2)}$ are $2t_1/t_2 - 2$ for $t_1/t_2 > 2$. The green dashed lines in the figures are these estimated values and turn out to be good approximations. We note that the behavior is a reminiscent of the on-site disorder-induced SSH model. In this model, there are the zero-dimensional edge states and when the strength of disorders is comparable to the band gap, they become unstable [111, 112].

Next, we see the other phases. In all the phases, the most fragile phase is the trivial phase against disorders. Actually, the mosaic-like area exists in Fig. 6.6 (a). In this area, the trained neural network predicts the phase "unknown". Specifically, the confidence of the four phases in the area is less than 98%. This phase is expected to be an Anderson-localized (AL) phase. The reason is described as follows. In the trivial phase, the highest occupied state is one of the massively degenerated states in a flat band. Then, the degeneracy is lifted by the disorders and one of the localized states become the highest occupied state. Later, we use the inverse participation ratio (IPR) to analyze the qualitative argument for the transition of the localization. We note that the existence of the critical phase between the AL phase and the trivial phase, which is predicted by the previous study [113]. However, the phase transition point appears at very small disorders ($W < 10^{-2}$). The strength of the disorder is much smaller than our minimum disorder strength ($W = 0.2$). We also note that Refs. [114, 115] predict the reentrance to the metallic phase, which appears at much larger disorder strength than the maximum value we study.

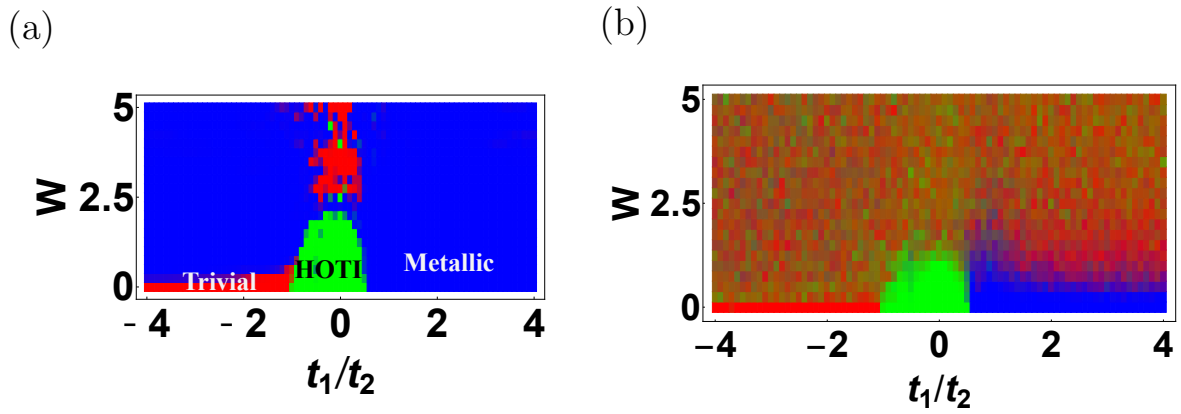

Figure 6.7: The phase diagram for the kagome HOTI model for the triangle geometry in the presence of disorders. (a) The phase diagram is plotted for the averaged densities of the wavefunctions. The green, blue and red areas denote the HOTI phase, the metallic phase and the trivial phase, respectively. (b) plots the phase diagram by the averaged probabilities for 30 single-shot wavefunctions.

6.3.2 Result for the triangular geometry

Then, let us show the results for the triangular geometry. Figure 6.7 shows the phase diagrams for $M = 16$. In this case, the three-dimensional vectors of the output is mapped to the color map of the RGB component; the trivial, HOTI and metallic phases respectively, correspond with red, blue, and green areas.

Above a critical line of the disorder strength, the HOTI phase vanishes. Similar to the rhombus geometry, we can calculate the rough estimation of the critical strengths by the energy gap. One can assume the HOTI phase is robust for disorders as long as the corner states are alive, as same as the rhombus geometry.

Next, we see the phase diagram generated by the averaged densities of the wavefunction. Above the trivial phase, there is a metallic phase as shown in Fig. 6.7 (a). As described in the previous section, it is an artifact of the averaging of the densities of the wavefunctions. Indeed, as seen in the phase diagram generated by the single-shot wavefunction [Fig. 6.7 (b)], we clearly see the mosaic-like pattern. It clearly indicates the AL phase and it is consistent with the wavefunction [Fig. 6.5]. Furthermore, one can observe that the Anderson localization occurs above the metallic phase. We also see that its critical value is smaller compared with the case of the rhombus geometry.

6.3.3 Inverse participation ratio

The localized states are distinguished from the extended state by the IPR [115–118]. The definition of the IPR is

$$p = \sum_i |\phi(r_i)|^4. \tag{6.3}$$

We assume the normalized eigenstates ($\sum_i |\phi(r_i)|^2 = 1$). For N-site system, the fully extended states are $\phi(r_i) = 1/\sqrt{N}$, hence $p \simeq 1/N$. Hence, in the thermodynamic limit, the IPR for the extended states vanishes. For the AL states, the IPR gets larger value. Hence it do not vanished in the thermodynamic limit.

For the breathing kagome model, metallic states and trivial states are the extended states, and the AL and corner states are the localized ones, so these two classes of phases

are distinguished by the IPR with the single-shot wavefunctions. For distinguishing the AL and corner states, it is needed to compare the IPR for the single-shot wavefunctions with the IPR for the averaged densities of the wavefunctions. Namely, there are uniform distribution of the averaged densities of the wavefunctions for the AL states. Hence, as same to the case of extended states, the obtained IPR is vanishing. On the other hand, as seen in Figs. 6.4 and 6.5, the distribution is still weighted at the corners for the corner states even for the wavefunction that is averaged over a number of samples, thus the IPR is not vanishing. Table 6.1 summarizes the expected behaviors for each phase.

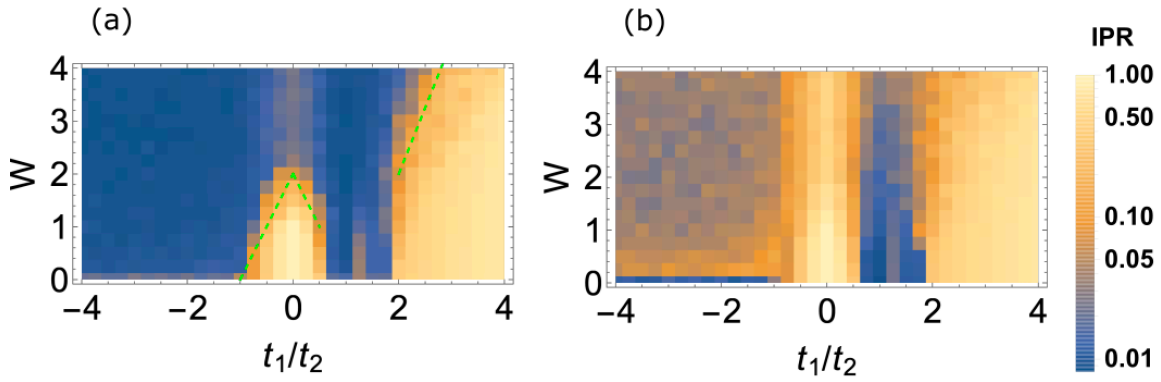

Figure 6.8: (a) The IPR calculated by the averaged densities of the wavefunctions is shown. (b) The IPR that is averaged for the densities of the single-shot wavefunctions is shown. For each parameters, 30 samples are taken. The system size is 10. As same to lines in Fig. 6.6, the green dashed lines denote the energy gap between the corner states and the bulk / edge states. We note the scale of the plots is logarithmic.

Figure 6.8 (a) shows the result of the IPR for the averaged densities of the wavefunctions for a rhombus geometry. Whereas Fig. 6.8 (b) shows that for the densities of the single-shot wavefunction. For the averaging, 30 samples are used. Indeed, we see that the IPR shows the behaviors expected in Table 6.1, comparing the phase diagram generated by the machine learning (Fig. 6.6). It indicates that the machine learning method is reliable.

Besides the correspondence between the phase diagram generated by the machine learning and the IPR, it is also found that we obtain large IPR at $t_1/t_2 = 1$ for weak W. These points originate from the appearance of the Dirac point at the Fermi level in the clean limit. The strongly-localized zero-energy modes, which are inherent in the disordered Dirac fermion systems may attribute this [119].

Table 6.1: The expected behaviors of the IPR for HOTI, AL, and trivial/metallic phases.

	HOTI	AL	Trivial/metallic
Single-shot	~ 1	~ 1	~ 0
averaged	~ 1	~ 0	~ 0

6.4 Conclusion

In this chapter, the phase diagram of the disordered breathing kagome model is investigated by the machine learning method. To achieve this, the wavefunction of the highest occupied

state is used as input data. In this study, the HOTI phase in which the corner states exists can be distinguished by the artificial neural network from other phases. The results reveal the robustness of the HOTI phase is remaining against disorders as far as the energy gap in the clean limit is not be exceeded by the disorder strength. To combine the results of the single-shot wavefunctions and the averaged densities of the wavefunctions, trivial/metallic states and the AL states can be successfully distinguished.

To use the conventional approaches to study the disordered models is important to justify the results about the study of the machine learning method. One of the conventional approaches is the IPR method. The IPR for our model is investigated for the rhombus geometry. The result is consistent with the phase diagram by the machine learning. Testing various other approaches, such as the transfer matrix method [73–75, 120, 121], will be an interesting future problem.

Finally, we emphasize the remark of the related works. In the electric circuit, Refs. [59,60] investigate the robustness of the corner states against disorders. In the platform, it was discovered the resonance peak of the impedance that the corner mode induces survives even though the inductances and capacitances are slightly disordered. Both bond disorders and on-site disorders in the language of the tight-binding model are induced by disorders of this kind in the electric circuits [122]. Our results are consistent with these results for the robustness about the corner states.

Chapter 7

Conclusions and perspectives

This thesis was dedicated to the theoretical study for the higher-order topological insulators. We have studied the higher-order topological insulators in several situations by using the Berry phase characterizations and the machine learning technique. Firstly, the Benalcazar-Bernevig-Hughes model with and without interactions are investigated by the Berry phase. In next, the kagome higher-order topological insulator model with disorders is investigated by the machine learning technique.

The thesis proposed the Berry phase as a topological invariant for the higher-order topological insulators. The Berry phase is quantized by symmetries, which is associated with the crystalline symmetries. We have found the bulk-corner correspondence between the Berry phase and the corner states of the higher-order topological insulators. The correspondence states the nontrivial Berry phase characterizes the higher-order topological insulators, which is adiabatically connected to the decoupled clusters. In Chapter 5, we demonstrate it for the Benalcazar-Bernevig-Hughes models in two- and three-dimensions. The bulk-corner correspondence still alive even with the electron-electron interactions. We also investigate the Berry phase for the spin-model-analogue of the Benalcazar-Bernevig-Hughes model.

The disorder effect for the higher-order topological insulators is studied in Chapter 6. We investigated the phase diagram of the disordered kagome higher-order topological insulator model. We generated a phase diagram of the model by machine learning. We also confirmed the phase diagram is consistent with the other analytical method. The study reveals that the HOTI phases of the kagome higher-order topological insulator model are robust against the disorders as far as the disorder strength does not exceed the energy gap.

In conclusion, we have obtained the numerical results about the higher-order topological insulator phases by two methods. In the first part, we proposed the quantized Berry phases characterize the higher-order topological insulators even with electron-electron interactions. In this study, we numerically found the phase transition point of the spin-model-analogue of the Benalcazar-Bernevig-Hughes model differs from that of the original Benalcazar-Bernevig-Hughes model. For the sake to find whether the difference comes from the finite size effect or not, we need to cautiously investigate the ground-state and the Berry phase in the larger systems. To obtain the explicit relation between the Berry phase and the other topological invariants is another perspective. However, we hope the Berry phase we proposed in the thesis may open a new way to search the higher-order topological insulators in correlated systems. In the second part, we have generated a phase diagram of the kagome higher-order topological insulator model and confirmed that the result is consistent with the other analytical method. We expect that the method can be applied to detect disordered phases for the higher-order topological materials in experiments.

Chapter 8

Acknowledgment

First of all, I would like to express my gratitude to Prof. Y. Hatsugai for helpful suggestions and sincere encouragements throughout my doctoral program. I would like to thank the examiners of the thesis, Prof. Y. Tokura, Prof. X. Hu and Prof. S. Iwamoto for valuable advice and comments. Special thanks also go to all the collaborators, Prof. T. Fukui, Dr. T. Kariyado, Dr. T. Yoshida, Dr. T. Mizoguchi and H. Wakao for useful comments and fruitful discussions. I also express my gratitude to all my colleagues, S. Fubasami, K. Hoda, T. Isobe, S. Ito, R. Kamoda, K. Kohda, K. Kudo, H. Kurihara, G. Najima, S. Nishizawa, S. Oka, Dr. S. Oono, D. Seki, T. Sekizawa, S. Suzuki, Y. Takahashi and T. Yamazaki for the stimulating discussions and the warm atmosphere. I would like to thank University of Tsukuba, JSPS and JASSO for financial supports. I owe my deep gratitude to my parents and my family for all kind of supports which made it possible to complete the study.

Publications

Journal publications

1. Hiromu Araki, Tomonari Mizoguchi, and Yasuhiro Hatsugai, "Phase diagram of disordered higher-order topological insulator: A machine learning study", Physical Review B, **99**, 085406 (2019)

2. Hiromu Araki, Tomonari Mizoguchi, and Yasuhiro Hatsugai, "Z_Q Berry Phase for Higher-Order Symmetry-Protected Topological Phases", Physical Review Research Rapid Communications, **2**, 012009 (2020)

3. Tomonari Mizoguchi, Hiromu Araki, and Yasuhiro Hatsugai, "Higher-Order Topological Phase in a Honeycomb-Lattice Model with Anti-Kekulé Distortion", Journal of Physical Society of Japan, **88**, 104703 (2019)

4. Hiromasa Wakao, Tsuneya Yoshida, Hiromu Araki, Tomonari Mizoguchi, and Yasuhiro Hatsugai, "Higher-order topological phases in a spring-mass model on a breathing kagome lattice", arXiv:1909.02828

International conference contributions

1. Hiromu Araki, Takahiro Fukui, and Yasuhiro Hatsugai, "Characterization of topological phases by the Weyl points of the entanglement Hamiltonian", The 28th International Conference on Low Temperature Physics, P.532, Gothenburg, Sweden, Aug., 2017

2. Hiromu Araki, Takahiro Fukui, and Yasuhiro Hatsugai, "Section entanglement Chern number for the Fu-Kane-Mele model and the Wilson-Dirac model", Trends in Theory of Correlated Materials (TTCM2017), P6, Tsukuba, Japan, Sep., 2017

3. Hiromu Araki, Takahiro Fukui, and Yasuhiro Hatsugai, "Section entanglement Chern number for strong and weak topological insulators", Novel Quantum States in Condensed Matter 2017 (NQS2017), Poster No. 3, Kyoto, Japan, Nov., 2017

4. Hiromu Araki, Takahiro Fukui, and Yasuhiro Hatsugai, "Section entanglement Chern number for Bi and Sb based on first principles calculations", Variety and universality of bulk-edge correspondence in topological phases: From solid state physics to transdisciplinary concepts, P8, Tsukuba, Japan, Feb., 2018

5. Hiromu Araki, Takahiro Fukui, and Yasuhiro Hatsugai, "Weyl Points of the Entanglement Spectrum for Topological Insulators from First Principles" American Physical Society March Meeting 2018, B08.00007, Los Angeles, U.S., Mar., 2018

6. Hiromu Araki, Takahiro Fukui, and Yasuhiro Hatsugai, "Topological phase of the strained HgTe from the entanglement Hamiltonians", Third informal workshop: Variety and universality of bulk-edge correspondence in topological phases: From solid state physics to transdisciplinary concepts, P4, Tsukuba, Japan, May, 2018

7. Hiromu Araki, Takahiro Fukui, and Yasuhiro Hatsugai, "Entanglement Chern Number for Topological Insulators without Inversion Symmetry from First Principles Calculation", 34th International Conference on the Physics of Semiconductors (ICPS2018), P3_131, Montpellier, France, Jul., 2018

8. Hiromu Araki, Takahiro Fukui, and Yasuhiro Hatsugai, "Topological phase of the strained HgTe from the entanglement Hamiltonians and the first-principles calculations", 23rd International Conference on High Magnetic Fields in Semiconductor Physics (HMF23), Poster-Mo09, Toulouse, France, Jul., 2018

9. Hiromu Araki, Tomonari Mizoguchi, and Yasuhiro Hatsugai, "Z_3 Berry phases for the Kagome higher order topological insulator model", Trends in Theory of Correlated Materials 2018 (TTCM2018), Poster No. 7, Geneve, Switzerland, Oct., 2018

10. Hiromu Araki, Tomonari Mizoguchi, and Yasuhiro Hatsugai, "Detection of higher order topological phase in a disordered breathing Kagome model by using machine learning" American Physical Society March Meeting 2019, K03.00009, Boston, U.S., Mar., 2019

11. Hiromu Araki, Tomonari Mizoguchi, and Yasuhiro Hatsugai, "Higher order topological phases of a disordered breathing Kagome model: A machine learning study" International Conference on Frontiers of Correlated Electron Sciences (FCES19), P02, Tokyo, Japan, Mar., 2019

12. Hiromu Araki, Tomonari Mizoguchi, and Yasuhiro Hatsugai, "Higher-order topological phases of a breathing kagome model with disorders: A machine learning study", Topological and Correlated Matter Gordon Research Conference, Hong Kong, China, Jun., 2019

13. Hiromu Araki, Tomonari Mizoguchi, and Yasuhiro Hatsugai, "Z_N Berry phases for several models of higher-order topological insulators", Les Houches Program on New Developments in Topological Condensed Matter Physics, Les Houches, France, Sep., 2019

Bibliography

[1] K. v. Klitzing, G. Dorda, and M. Pepper. New method for high-accuracy determination of the fine-structure constant based on quantized hall resistance. *Phys. Rev. Lett.*, 45:494–497, Aug 1980.

[2] D. J. Thouless, M. Kohmoto, M. P. Nightingale, and M. den Nijs. Quantized hall conductance in a two-dimensional periodic potential. *Phys. Rev. Lett.*, 49:405–408, Aug 1982.

[3] R. B. Laughlin. Quantized hall conductivity in two dimensions. *Phys. Rev. B*, 23:5632–5633, May 1981.

[4] B. I. Halperin. Quantized hall conductance, current-carrying edge states, and the existence of extended states in a two-dimensional disordered potential. *Phys. Rev. B*, 25:2185–2190, Feb 1982.

[5] Yasuhiro Hatsugai. Chern number and edge states in the integer quantum hall effect. *Phys. Rev. Lett.*, 71:3697–3700, Nov 1993.

[6] Yasuhiro Hatsugai. Edge states in the integer quantum hall effect and the riemann surface of the bloch function. *Phys. Rev. B*, 48:11851–11862, Oct 1993.

[7] C. L. Kane and E. J. Mele. Z_2 topological order and the quantum spin hall effect. *Phys. Rev. Lett.*, 95:146802, Sep 2005.

[8] C. L. Kane and E. J. Mele. Quantum spin hall effect in graphene. *Phys. Rev. Lett.*, 95:226801, Nov 2005.

[9] Liang Fu, C. L. Kane, and E. J. Mele. Topological insulators in three dimensions. *Phys. Rev. Lett.*, 98:106803, Mar 2007.

[10] Alexei Kitaev. Periodic table for topological insulators and superconductors. *AIP Conf. Proc.*, 1134:22, Jun 2009.

[11] Andreas P. Schnyder, Shinsei Ryu, Akira Furusaki, and Andreas W. W. Ludwig. Classification of topological insulators and superconductors in three spatial dimensions. *Phys. Rev. B*, 78:195125, Nov 2008.

[12] Shinsei Ryu, Andreas P Schnyder, Akira Furusaki, and Andreas W W Ludwig. Topological insulators and superconductors: tenfold way and dimensional hierarchy. *New J. Phys.*, 12(6):065010, 2010.

[13] Alexander Altland and Martin R. Zirnbauer. Nonstandard symmetry classes in mesoscopic normal-superconducting hybrid structures. *Phys. Rev. B*, 55:1142–1161, Jan 1997.

[14] Liang Fu and C. L. Kane. Topological insulators with inversion symmetry. *Phys. Rev. B*, 76:045302, Jul 2007.

[15] Liang Fu. Topological crystalline insulators. *Phys. Rev. Lett.*, 106:106802, Mar 2011.

[16] Takahiro Morimoto and Akira Furusaki. Topological classification with additional symmetries from clifford algebras. *Phys. Rev. B*, 88:125129, Sep 2013.

[17] Ken Shiozaki and Masatoshi Sato. Topology of crystalline insulators and superconductors. *Phys. Rev. B*, 90:165114, Oct 2014.

[18] Youichi Yanase and Ken Shiozaki. Möbius topological superconductivity in upt_3. *Phys. Rev. B*, 95:224514, Jun 2017.

[19] Jorrit Kruthoff, Jan de Boer, Jasper van Wezel, Charles L. Kane, and Robert-Jan Slager. Topological classification of crystalline insulators through band structure combinatorics. *Phys. Rev. X*, 7:041069, Dec 2017.

[20] Lukasz Fidkowski and Alexei Kitaev. Topological phases of fermions in one dimension. *Phys. Rev. B*, 83:075103, Feb 2011.

[21] Ari M. Turner, Frank Pollmann, and Erez Berg. Topological phases of one-dimensional fermions: An entanglement point of view. *Phys. Rev. B*, 83:075102, Feb 2011.

[22] Tsuneya Yoshida, Akito Daido, Youichi Yanase, and Norio Kawakami. Fate of majorana modes in $cecoin_5$/$ybcoin_5$ superlattices: A test bed for the reduction of topological classification. *Phys. Rev. Lett.*, 118:147001, Apr 2017.

[23] Tsuneya Yoshida, Ippei Danshita, Robert Peters, and Norio Kawakami. Reduction of topological $\mathbb{Z}$ classification in cold-atom systems. *Phys. Rev. Lett.*, 121:025301, Jul 2018.

[24] Dmytro Pesin and Leon Balents. Mott physics and band topology in materials with strong spin–orbit interaction. *Nature Physics*, 6(5):376–381, 2010.

[25] Chong Wang and T. Senthil. Time-reversal symmetric $u(1)$ quantum spin liquids. *Phys. Rev. X*, 6:011034, Mar 2016.

[26] Michael Levin and Ady Stern. Fractional topological insulators. *Phys. Rev. Lett.*, 103:196803, Nov 2009.

[27] Titus Neupert, Luiz Santos, Shinsei Ryu, Claudio Chamon, and Christopher Mudry. Fractional topological liquids with time-reversal symmetry and their lattice realization. *Phys. Rev. B*, 84:165107, Oct 2011.

[28] Yang-Le Wu, N. Regnault, and B. Andrei Bernevig. Gauge-fixed wannier wave functions for fractional topological insulators. *Phys. Rev. B*, 86:085129, Aug 2012.

[29] C. Repellin, B. Andrei Bernevig, and N. Regnault. F_2 fractional topological insulators in two dimensions. *Phys. Rev. B*, 90:245401, Dec 2014.

[30] Frank Pollmann, Ari M. Turner, Erez Berg, and Masaki Oshikawa. Entanglement spectrum of a topological phase in one dimension. *Phys. Rev. B*, 81:064439, Feb 2010.

[31] Frank Pollmann, Erez Berg, Ari M. Turner, and Masaki Oshikawa. Symmetry protection of topological phases in one-dimensional quantum spin systems. *Phys. Rev. B*, 85:075125, Feb 2012.

[32] Xiao-Gang Wen. Symmetry-protected topological phases in noninteracting fermion systems. *Phys. Rev. B*, 85:085103, Feb 2012.

[33] Xiao-Gang Wen. Symmetry-protected topological invariants of symmetry-protected topological phases of interacting bosons and fermions. *Phys. Rev. B*, 89:035147, Jan 2014.

[34] Juven C. Wang, Zheng-Cheng Gu, and Xiao-Gang Wen. Field-theory representation of gauge-gravity symmetry-protected topological invariants, group cohomology, and beyond. *Phys. Rev. Lett.*, 114:031601, Jan 2015.

[35] Yasuhiro Hatsugai. Quantized berry phases as a local order parameter of a quantum liquid. *Journal of the Physical Society of Japan*, 75(12):123601, 2006.

[36] Yasuhiro Hatsugai. Symmetry-protected $\mathbb{Z}_2$-quantization and quaternionic berry connection with kramers degeneracy. *New Journal of Physics*, 12(6):065004, 2010.

[37] T. Hirano, H. Katsura, and Y. Hatsugai. Topological classification of gapped spin chains: Quantized berry phase as a local order parameter. *Phys. Rev. B*, 77:094431, Mar 2008.

[38] Y Hatsugai. Quantized berry phases for a local characterization of spin liquids in frustrated spin systems. *Journal of Physics: Condensed Matter*, 19(14):145209, mar 2007.

[39] Yuichi Motoyama and Synge Todo. Path-integral monte carlo method for the local Z_2 berry phase. *Phys. Rev. E*, 87:021301, Feb 2013.

[40] Natalia Chepiga, Ian Affleck, and Frédéric Mila. Spontaneous dimerization, critical lines, and short-range correlations in a frustrated spin-1 chain. *Phys. Rev. B*, 94:205112, Nov 2016.

[41] Toshikaze Kariyado, Takahiro Morimoto, and Yasuhiro Hatsugai. Z_N berry phases in symmetry protected topological phases. *Phys. Rev. Lett.*, 120:247202, Jun 2018.

[42] Yuichi Motoyama and Synge Todo. Z_N berry phase and symmetry-protected topological phases of the su(n) antiferromagnetic heisenberg chain. *Phys. Rev. B*, 98:195127, Nov 2018.

[43] Tohru Kawarabayashi, Kota Ishii, and Yasuhiro Hatsugai. Fractionally quantized berry' s phase in an anisotropic magnet on the kagome lattice. *Journal of the Physical Society of Japan*, 88(4):045001, 2019.

[44] Shota Fubasami, Tomonari Mizoguchi, and Yasuhiro Hatsugai. Sequential quantum phase transitions in J_1-J_2 heisenberg chains with integer spins $s > 1$: Quantized berry phase and valence-bond solids. *Phys. Rev. B*, 100:014438, Jul 2019.

[45] Robert-Jan Slager, Andrej Mesaros, Vladimir Juričić, and Jan Zaanen. The space group classification of topological band-insulators. *Nature Physics*, 9:98 EP –, 12 2012.

[46] Koji Hashimoto, Xi Wu, and Taro Kimura. Edge states at an intersection of edges of a topological material. *Phys. Rev. B*, 95:165443, Apr 2017.

[47] Frank Schindler, Ashley M. Cook, Maia G. Vergniory, Zhijun Wang, Stuart S. P. Parkin, B. Andrei Bernevig, and Titus Neupert. Higher-order topological insulators. *Science Advances*, 4(6), 2018.

[48] Wladimir A. Benalcazar, B. Andrei Bernevig, and Taylor L. Hughes. Electric multipole moments, topological multipole moment pumping, and chiral hinge states in crystalline insulators. *Phys. Rev. B*, 96:245115, Dec 2017.

[49] Wladimir A. Benalcazar, B. Andrei Bernevig, and Taylor L. Hughes. Quantized electric multipole insulators. *Science*, 357(6346):61–66, 2017.

[50] Motohiko Ezawa. Higher-order topological insulators and semimetals on the breathing kagome and pyrochlore lattices. *Phys. Rev. Lett.*, 120:026801, Jan 2018.

[51] Flore K. Kunst, Guido van Miert, and Emil J. Bergholtz. Lattice models with exactly solvable topological hinge and corner states. *Phys. Rev. B*, 97:241405, Jun 2018.

[52] Yichen Xu, Ruolan Xue, and Shaolong Wan. Topological corner states on kagome lattice based chiral higher-order topological insulator. *arXiv:1711.09202*.

[53] Shin Hayashi. Topological invariants and corner states for hamiltonians on a three-dimensional lattice. *Communications in Mathematical Physics*, 364(1):343–356, 2018.

[54] Shin Hayashi. Toeplitz operators on concave corners and topologically protected corner states. *Letters in Mathematical Physics*, 109(10):2223–2254, Oct 2019.

[55] Ryo Okugawa, Shin Hayashi, and Takeshi Nakanishi. Second-order topological phases protected by chiral symmetry. *Phys. Rev. B*, 100:235302, Dec 2019.

[56] Flore K. Kunst, Guido van Miert, and Emil J. Bergholtz. Boundaries of boundaries: A systematic approach to lattice models with solvable boundary states of arbitrary codimension. *Phys. Rev. B*, 99:085426, Feb 2019.

[57] Frank Schindler, Zhijun Wang, Maia G. Vergniory, Ashley M. Cook, Anil Murani, Shamashis Sengupta, Alik Yu. Kasumov, Richard Deblock, Sangjun Jeon, Ilya Drozdov, Hélène Bouchiat, Sophie Guéron, Ali Yazdani, B. Andrei Bernevig, and Titus Neupert. Higher-order topology in bismuth. *Nature Physics*, 14(9):918–924, 2018.

[58] Marc Serra-Garcia, Valerio Peri, Roman Süsstrunk, Osama R. Bilal, Tom Larsen, Luis Guillermo Villanueva, and Sebastian D. Huber. Observation of a phononic quadrupole topological insulator. *Nature*, 555:342 EP –, 01 2018.

[59] Stefan Imhof, Christian Berger, Florian Bayer, Johannes Brehm, Laurens W. Molenkamp, Tobias Kiessling, Frank Schindler, Ching Hua Lee, Martin Greiter, Titus Neupert, and Ronny Thomale. Topolectrical-circuit realization of topological corner modes. *Nature Physics*, 14(9):925–929, 2018.

[60] Motohiko Ezawa. Higher-order topological electric circuits and topological corner resonance on the breathing kagome and pyrochlore lattices. *Phys. Rev. B*, 98:201402, Nov 2018.

[61] Bi-Ye Xie, Hong-Fei Wang, Hai-Xiao Wang, Xue-Yi Zhu, Jian-Hua Jiang, Ming-Hui Lu, and Yan-Feng Chen. Second-order photonic topological insulator with corner states. *Phys. Rev. B*, 98:205147, Nov 2018.

[62] Xiao-Dong Chen, Wei-Min Deng, Fu-Long Shi, Fu-Li Zhao, Min Chen, and Jian-Wen Dong. Direct observation of corner states in second-order topological photonic crystal slabs. *Phys. Rev. Lett.*, 122:233902, Jun 2019.

[63] Haoran Xue, Yahui Yang, Fei Gao, Yidong Chong, and Baile Zhang. Acoustic higher-order topological insulator on a kagome lattice. *Nature Materials*, 18(2):108–112, 2019.

[64] Mikio Morii, Shiro Ikeda, Nozomu Tominaga, Masaomi Tanaka, Tomoki Morokuma, Katsuhiko Ishiguro, Junji Yamato, Naonori Ueda, Naotaka Suzuki, Naoki Yasuda, and Naoki Yoshida. Machine-learning selection of optical transients in the subaru/hyper suprime-cam survey. *Publications of the Astronomical Society of Japan*, 68(6):104, 2016.

[65] Shimon Whiteson and Daniel Whiteson. Machine learning for event selection in high energy physics. *Engineering Applications of Artificial Intelligence*, 22(8):1203 – 1217, 2009.

[66] P. Baldi, P. Sadowski, and D. Whiteson. Searching for exotic particles in high-energy physics with deep learning. *Nature Communications*, 5:430, Jul 2014.

[67] Huitao Shen, Junwei Liu, and Liang Fu. Self-learning monte carlo with deep neural networks. *Phys. Rev. B*, 97:205140, May 2018.

[68] Giuseppe Carleo and Matthias Troyer. Solving the quantum many-body problem with artificial neural networks. *Science*, 355(6325):602–606, 2017.

[69] Yusuke Nomura, Andrew S. Darmawan, Youhei Yamaji, and Masatoshi Imada. Restricted boltzmann machine learning for solving strongly correlated quantum systems. *Phys. Rev. B*, 96:205152, Nov 2017.

[70] Hiroyuki Fujita, Yuya O. Nakagawa, Sho Sugiura, and Masaki Oshikawa. Construction of hamiltonians by supervised learning of energy and entanglement spectra. *Phys. Rev. B*, 97:075114, Feb 2018.

[71] Patrick Huembeli, Alexandre Dauphin, and Peter Wittek. Identifying quantum phase transitions with adversarial neural networks. *Phys. Rev. B*, 97:134109, Apr 2018.

[72] Patrick Huembeli, Alexandre Dauphin, Peter Wittek, and Christian Gogolin. Automated discovery of characteristic features of phase transitions in many-body localization. *Phys. Rev. B*, 99:104106, Mar 2019.

[73] Tomoki Ohtsuki and Tomi Ohtsuki. Deep learning the quantum phase transitions in random two-dimensional electron systems. *J. Phys. Soc. Jpn.*, 85(12):123706, 2016.

[74] Tomi Ohtsuki and Tomoki Ohtsuki. Deep learning the quantum phase transitions in random electron systems: Applications to three dimensions. *J. Phys. Soc. Jpn.*, 86(4):044708, 2017.

[75] Nobuyuki Yoshioka, Yutaka Akagi, and Hosho Katsura. Learning disordered topological phases by statistical recovery of symmetry. *Phys. Rev. B*, 97:205110, May 2018.

[76] Ming-Chiang Chung and Ingo Peschel. Density-matrix spectra of solvable fermionic systems. *Phys. Rev. B*, 64:064412, Jul 2001.

[77] A. Osterloh, Luigi Amico, G. Falci, and Rosario Fazio. Scaling of entanglement close to a quantum phase transition. *Nature*, 416(6881):608–610, 04 2002.

[78] Tobias J. Osborne and Michael A. Nielsen. Entanglement in a simple quantum phase transition. *Phys. Rev. A*, 66:032110, Sep 2002.

[79] G. Vidal, J. I. Latorre, E. Rico, and A. Kitaev. Entanglement in quantum critical phenomena. *Phys. Rev. Lett.*, 90:227902, Jun 2003.

[80] Siew-Ann Cheong and Christopher L. Henley. Many-body density matrices for free fermions. *Phys. Rev. B*, 69:075111, Feb 2004.

[81] S. Ryu and Y. Hatsugai. Entanglement entropy and the berry phase in the solid state. *Phys. Rev. B*, 73:245115, Jun 2006.

[82] Hui Li and F. D. M. Haldane. Entanglement spectrum as a generalization of entanglement entropy: Identification of topological order in non-abelian fractional quantum hall effect states. *Phys. Rev. Lett.*, 101:010504, Jul 2008.

[83] A. Alexandradinata, Taylor L. Hughes, and B. Andrei Bernevig. Trace index and spectral flow in the entanglement spectrum of topological insulators. *Phys. Rev. B*, 84:195103, Nov 2011.

[84] Timothy H. Hsieh and Liang Fu. Bulk entanglement spectrum reveals quantum criticality within a topological state. *Phys. Rev. Lett.*, 113:106801, Sep 2014.

[85] Takahiro Fukui and Yasuhiro Hatsugai. Entanglement chern number for an extensive partition of a topological ground state. *J. Phys. Soc. Jpn.*, 83(11):113705, 2014.

[86] Takahiro Fukui and Yasuhiro Hatsugai. Disentangled topological numbers by a purification of entangled mixed states for non-interacting fermion systems. *J. Phys. Soc. Jpn.*, 84(4):043703, 2015.

[87] Hiromu Araki, Toshikaze Kariyado, Takahiro Fukui, and Yasuhiro Hatsugai. Entanglement chern number of the kane - mele model with ferromagnetism. *Journal of the Physical Society of Japan*, 85(4):043706, 2016.

[88] Takahiro Fukui and Yasuhiro Hatsugai. A spin pump characterized by entanglement chern numbers. *Journal of the Physical Society of Japan*, 85(8):083703, 2016.

[89] Hiromu Araki, Takahiro Fukui, and Yasuhiro Hatsugai. Entanglement chern number for three-dimensional topological insulators: Characterization by weyl points of entanglement hamiltonians. *Phys. Rev. B*, 96:165139, Oct 2017.

[90] Ingo Peschel. Calculation of reduced density matrices from correlation functions. *J. Phys. A: Math. Gen.*, 36(14):L205, 2003.

[91] Y. Hatsugai and I. Maruyama. $\mathbb{Z}_{\mathrm{Q}}$ topological invariants for polyacetylene, kagome and pyrochlore lattices. *Europhys. Lett.*, 95(2):20003, 2011.

[92] Lukasz Fidkowski, T. S. Jackson, and Israel Klich. Model characterization of gapless edge modes of topological insulators using intermediate brillouin-zone functions. *Phys. Rev. Lett.*, 107:036601, Jul 2011.

[93] R. D. King-Smith and David Vanderbilt. Theory of polarization of crystalline solids. *Phys. Rev. B*, 47:1651–1654, Jan 1993.

[94] David Vanderbilt and R. D. King-Smith. Electric polarization as a bulk quantity and its relation to surface charge. *Phys. Rev. B*, 48:4442–4455, Aug 1993.

[95] S. Kivelson. Wannier functions in one-dimensional disordered systems: Application to fractionally charged solitons. *Phys. Rev. B*, 26:4269–4277, Oct 1982.

[96] Nicola Marzari and David Vanderbilt. Maximally localized generalized wannier functions for composite energy bands. *Phys. Rev. B*, 56:12847–12865, Nov 1997.

[97] Sinisa Coh and David Vanderbilt. Electric polarization in a chern insulator. *Phys. Rev. Lett.*, 102:107603, Mar 2009.

[98] Rui Yu, Xiao Liang Qi, Andrei Bernevig, Zhong Fang, and Xi Dai. Equivalent expression of F_2 topological invariant for band insulators using the non-abelian berry connection. *Phys. Rev. B*, 84:075119, Aug 2011.

[99] Xiao-Liang Qi. Generic wave-function description of fractional quantum anomalous hall states and fractional topological insulators. *Phys. Rev. Lett.*, 107:126803, Sep 2011.

[100] Ingi Kim, Satoshi Iwamoto, and Yasuhiko Arakawa. Topologically protected elastic waves in one-dimensional phononic crystals of continuous media. *Applied Physics Express*, 11(1):017201, dec 2017.

[101] Yasutomo Ota, Ryota Katsumi, Katsuyuki Watanabe, Satoshi Iwamoto, and Yasuhiko Arakawa. Topological photonic crystal nanocavity laser. *Communications Physics*, 1(1):86, 2018.

[102] Mitsuaki Kawamura, Kazuyoshi Yoshimi, Takahiro Misawa, Youhei Yamaji, Synge Todo, and Naoki Kawashima. Quantum lattice model solver h Φ. *Computer Physics Communications*, 217:180 – 192, 2017.

[103] Oleg Dubinkin and Taylor L. Hughes. Higher-order bosonic topological phases in spin models. *Phys. Rev. B*, 99:235132, Jun 2019.

[104] Byungmin Kang, Ken Shiozaki, and Gil Young Cho. Many-body order parameters for multipoles in solids. *Phys. Rev. B*, 100:245134, Dec 2019.

[105] Jan Attig, Krishanu Roychowdhury, Michael J. Lawler, and Simon Trebst. Topological mechanics from supersymmetry. *Phys. Rev. Research*, 1:032047, Dec 2019.

[106] Tomonari Mizoguchi, Hiromu Araki, and Yasuhiro Hatsugai. Higher-order topological phase in a honeycomb-lattice model with anti-kekulé distortion. *Journal of the Physical Society of Japan*, 88(10):104703, 2019.

[107] Koji Kudo, Tsuneya Yoshida, and Yasuhiro Hatsugai. Higher-order topological mott insulators. *Phys. Rev. Lett.*, 123:196402, Nov 2019.

[108] Wladimir A. Benalcazar, Tianhe Li, and Taylor L. Hughes. Quantization of fractional corner charge in C_n-symmetric higher-order topological crystalline insulators. *Phys. Rev. B*, 99:245151, Jun 2019.

[109] https://pytorch.org.

[110] Ning Sun, Jinmin Yi, Pengfei Zhang, Huitao Shen, and Hui Zhai. Deep learning topological invariants of band insulators. *Phys. Rev. B*, 98:085402, Aug 2018.

[111] Beatriz Pérez-González, Miguel Bello, Álvaro Gómez-León, and Gloria Platero. Ssh model with long-range hoppings: topology, driving and disorder. *arXiv:1802.03973*.

[112] F. Munoz, Fernanda Pinilla, J. Mella, and Mario I. Molina. Topological properties of a bipartite lattice of domain wall states. *Scientific Reports*, 8(1):17330, 2018.

[113] J. T. Chalker, T. S. Pickles, and Pragya Shukla. Anderson localization in tight-binding models with flat bands. *Phys. Rev. B*, 82:104209, Sep 2010.

[114] Masaki Goda, Shinya Nishino, and Hiroki Matsuda. Inverse anderson transition caused by flatbands. *Phys. Rev. Lett.*, 96:126401, Mar 2006.

[115] Shinya Nishino, Hiroki Matsuda, and Masaki Goda. Flat-band localization in weakly disordered system. *Journal of the Physical Society of Japan*, 76(2):024709, 2007.

[116] M. Schreiber. Fractal character of eigenstates in weakly disordered three-dimensional systems. *Phys. Rev. B*, 31:6146–6149, May 1985.

[117] Thomas C. Halsey, Mogens H. Jensen, Leo P. Kadanoff, Itamar Procaccia, and Boris I. Shraiman. Fractal measures and their singularities: The characterization of strange sets. *Phys. Rev. A*, 33:1141–1151, Feb 1986.

[118] Sayaka Yoshino and Makoto Okazaki. Numerical study of electron localization in anderson model for disordered systems: Spatial extension of wavefunction. *Journal of the Physical Society of Japan*, 43(2):415–423, 1977.

[119] Y. Hatsugai and P. A. Lee. Numerical study of localization of dirac fermions on a lattice in two dimensions. *Phys. Rev. B*, 48:4204–4207, Aug 1993.

[120] Koji Kobayashi, Tomi Ohtsuki, and Ken-Ichiro Imura. Disordered weak and strong topological insulators. *Phys. Rev. Lett.*, 110:236803, Jun 2013.

[121] A. MacKinnon and B. Kramer. The scaling theory of electrons in disordered solids: Additional numerical results. *Zeitschrift für Physik B Condensed Matter*, 53(1):1–13, Mar 1983.

[122] Ching Hua Lee, Stefan Imhof, Christian Berger, Florian Bayer, Johannes Brehm, Laurens W. Molenkamp, Tobias Kiessling, and Ronny Thomale. Topolectrical circuits. *Communications Physics*, 1(1):39, 2018.